

DTIC FILE COPY.

①

AD-A218 478

FROM: AFIT/CI

7 July 1989

SUBJECT: Review of Thesis/Dissertation for Public Release

TO: PA

1. Request you review the attached for public release prior to being sent to DTIC.

2. Reply by indorsement to CI NLT \_\_\_\_\_.

*Ernest A. Haygood*  
ERNEST A. HAYGOOD, 1st Lt, USAF  
Executive Officer  
Civilian Institution Programs

1 Atch.  
THESIS 89-047  
MCNAMEE

1st Ind, AFIT/PA

TO: CI

8 FEB 1990

Approved/~~Disapproved~~ for public release.

Log Number: 89-10-91

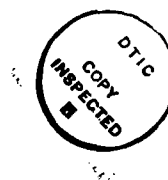
*Harriet D. Moultrie*  
HARRIET D. MOULTRIE, Capt, USAF  
Director, Office of Public Affairs

DTIC  
ELECTE  
FEB 22 1990  
S E D  
CO

REPORT DOCUMENTATION PAGE				Form Approved OMB No. 0704-0188	
1a. REPORT SECURITY CLASSIFICATION UNCLASSIFIED			1b. RESTRICTIVE MARKINGS NONE		
2a. SECURITY CLASSIFICATION AUTHORITY			3. DISTRIBUTION/AVAILABILITY OF REPORT APPROVED FOR PUBLIC RELEASE; DISTRIBUTION UNLIMITED.		
2b. DECLASSIFICATION/DOWNGRADING SCHEDULE					
4. PERFORMING ORGANIZATION REPORT NUMBER(S)			5. MONITORING ORGANIZATION REPORT NUMBER(S) AFIT/CI/CIA-89-047		
6a. NAME OF PERFORMING ORGANIZATION AFIT STUDENT AT SAINT LOUIS UNIVERSITY		6b. OFFICE SYMBOL (if applicable)	7a. NAME OF MONITORING ORGANIZATION AFIT/CIA		
6c. ADDRESS (City, State, and ZIP Code)			7b. ADDRESS (City, State, and ZIP Code) Wright-Patterson AFB OH 45433-6583		
8a. NAME OF FUNDING/SPONSORING ORGANIZATION		8b. OFFICE SYMBOL (if applicable)	9. PROCUREMENT INSTRUMENT IDENTIFICATION NUMBER		
8c. ADDRESS (City, State, and ZIP Code)			10. SOURCE OF FUNDING NUMBERS		
			PROGRAM ELEMENT NO.	PROJECT NO.	TASK NO.
11. TITLE (Include Security Classification) (UNCLASSIFIED) Examination of Microburst Development in a Colorado Thunderstorm for the 5 August 1982 case.					
12. PERSONAL AUTHOR(S) William Edward McNamee					
13a. TYPE OF REPORT THESIS/DISSERTATION		13b. TIME COVERED FROM _____ TO _____	14. DATE OF REPORT (Year, Month, Day) 1989		15. PAGE COUNT 151
16. SUPPLEMENTARY NOTATION APPROVED FOR PUBLIC RELEASE IAW AFR 190-1 ERNEST A. HAYGOOD, 1st Lt, USAF Executive Officer, Civilian Institution Programs					
17. COSATI CODES			18. SUBJECT TERMS (Continue on reverse if necessary and identify by block number)		
FIELD	GROUP	SUB-GROUP			
19. ABSTRACT (Continue on reverse if necessary and identify by block number)					
20. DISTRIBUTION/AVAILABILITY OF ABSTRACT <input checked="" type="checkbox"/> UNCLASSIFIED/UNLIMITED <input type="checkbox"/> SAME AS RPT. <input type="checkbox"/> DTIC USERS					
22a. NAME OF RESPONSIBLE INDIVIDUAL ERNEST A. HAYGOOD, 1st Lt, USAF			21. ABSTRACT SECURITY CLASSIFICATION UNCLASSIFIED		22c. OFFICE SYMBOL AFIT/CI
			22b. TELEPHONE (Include Area Code) (513) 255-2259		

EXAMINATION OF MICROBURST DEVELOPMENT IN A  
 COLORADO THUNDERSTORM FOR THE  
 5 AUGUST 1982 CASE.

William Edward McNamee, B.S.



Accession For	
NTIS GRA&I	<input checked="" type="checkbox"/>
DTIC TAB	<input type="checkbox"/>
Unannounced	<input type="checkbox"/>
Justification	
By	
Distribution/	
Availability Codes	
Dist	Avail and/or Special
A-1	

A Digest Presented to the Faculty of the Graduate School  
 of Saint Louis University in Partial Fulfillment of  
 the Requirements for the Degree of  
 Master of Science (Research)

1989

90 02 20 152

## DIGEST

Dual-doppler radar data were collected near Denver, CO during the summer of 1982 to study the phenomenon of microbursts within the boundary layer. Horizontal and vertical fields of reflectivity, vertical velocity, perturbation temperature and pressure are obtained from the radar data to assist in this microburst study. Three time periods on 5 August are used to detail the chronological development of microbursts: 1845, 1847 and 1850 MDT.

The fields of perturbation pressure and temperature are derived from the 3-dimensional wind field using a thermodynamic retrieval method based on the momentum equations. Inclusions of local time tendency terms in the momentum equations will increase resolution of these fields.

During the 1845-1850 window, there are two microbursts, and one downdraft whose outflow does not extend to the surface. The two microbursts are in close proximity to each other, so the outflow from one results in upward vertical motion that helps lift surface moisture to condense at upper levels and help sustain the downdraft intensity *via* precipitation loading. At the gust front, the vertical shear of the horizontal winds creates a rotary-type circulation that is lifted at the gust front

boundary. This rotation helps to maintain the microburst by steering dry upper-level winds into the column to cool the downdraft. The upper-level flow maintains its momentum during the entrainment into the downdraft to eventually diverge at the surface.

Microburst development is a result of many factors, including interaction with its environment. The rate of development is directly related to ample supplies of warm, moist low-level air, and upper-level high velocity dry air.

EXAMINATION OF MICROBURST DEVELOPMENT IN A  
COLORADO THUNDERSTORM FOR THE  
5 AUGUST 1982 CASE.

William Edward McNamee, B.S.

A Thesis Presented to the Faculty of the Graduate School  
of Saint Louis University in Partial Fulfillment of  
the Requirements for the Degree of  
Master of Science (Research)

1989

*COMMITTEE IN CHARGE OF CANDIDACY:*

Professor Yeong-je Lin,  
*Chairperson and Advisor*

Assistant Professor Lawrence Coy

Associate Professor James T. Moore

## ACKNOWLEDGEMENTS

The author would like to thank Dr. Yeong-Jer Lin for his guidance and assistance in completing this project. I would like to also extend my thanks to Drs. James T. Moore and Lawrence Coy for their comments and suggestions on project improvement. Special thanks go to Captain John Coover for his expert help in the many computational problems that arose during the study, and for his work that laid the foundation that made this thesis possible. Thanks also go to Sonia Lasher for her helpful inputs and plotting. My appreciation goes to my wife, Sharon and to my daughters Dawn and Kelly for their understanding and patience during this project.



## TABLE OF CONTENTS

Chapter	Page
1. Introduction.....	1
2. Statement of the Problem.....	4
3. Methodology.....	7
3.1 Data Analysis Techniques.....	8
3.2 Momentum Checks to Indicate Data Accuracy.....	12
4. Results.....	19
4.1 Plan View Plots (tendency not considered).....	19
4.1.1 1845 Plan View Plots.....	20
4.1.2 1847 Plan View Plots.....	37
4.1.3 1850 Plan View Plots.....	52
4.2 Cross-Section Plots (tendency not considered).....	66
4.2.1 (NW-SE) Cross-Section Plots.....	68
4.2.1.a (NW-SE) Cross-Section at 1845.....	68
4.2.1.b (NW-SE) Cross-Section at 1847.....	74
4.2.1.c (NW-SE) Cross-Section at 1850.....	77
4.2.2 (E-W) Cross-Section Plots.....	83
4.2.2.a (E-W) Cross-Section at 1845.....	83
4.2.2.b (E-W) Cross-Section at 1847.....	88
4.2.2.c (E-W) Cross-Section at 1850.....	91
4.3 Plan View Plots (tendency included).....	97
4.3.1 1845 Plan View Plots.....	98
4.3.2 1847 Plan View Plots.....	109
4.3.3 1850 Plan View Plots.....	118
4.4 Cross-Section Plots (tendency included).....	126

4.4.1	(NW-SE) Cross-Section at 1845.....	126
4.4.2	(NW-SE) Cross-Section at 1847.....	130
4.4.3	(NW-SE) Cross-Section at 1850.....	133
4.4.4	(E-W) Cross-Section at 1845.....	136
4.4.5	(E-W) Cross-Section at 1847.....	139
4.4.6	(E-W) Cross-Section at 1850.....	142
5.	Summary and Conclusions.....	145
	REFERENCES.....	149
	BIOGRAPHY OF AUTHOR.....	151

## LIST OF TABLES

Table 1: Momentum Check Values using a 31 x 31 matrix (tendency not included).....	13
Table 2: Momentum Check Values using a 31 x 31 matrix (tendency included).....	16
Table 3: Momentum Check Values using a 27 x 27 matrix (tendency included).....	17

# LIST OF FIGURES

Figure	Page
4.1 Plan view of the horizontal wind field and reflectivity field for 1845 MDT at 0.25 km.....	21
4.2 Same as Fig 4.1, except for vertical velocity.....	22
4.3 Same as Fig 4.1, except for pressure $P'_d$ .....	24
4.4 Same as Fig 4.1, except for temperature $T'_{vd}$ .....	25
4.5 Plan view of the horizontal wind field and reflectivity field for 1845 MDT at 0.5 km.....	27
4.6 Same as Fig 4.5, except for vertical velocity.....	28
4.7 Plan view of the horizontal wind field and reflectivity field for 1845 MDT at 0.75 km.....	30
4.8 Plan view of the horizontal wind field and reflectivity field for 1845 MDT at 1 km.....	31
4.9 Same as Fig 4.8, except for vertical velocity.....	33
4.10 Plan view of the horizontal wind field and reflectivity field for 1845 MDT at 1.25 km.....	34
4.11 Same as Fig 4.10, except for vertical velocity.....	35
4.12 Plan view of the horizontal wind field and reflectivity field for 1847 MDT at 0.25 km.....	38
4.13 Same as Fig 4.12, except for vertical velocity.....	40
4.14 Same as Fig 4.13, except for pressure $P'_{vd}$ .....	41
4.15 Same as Fig 4.12, except for temperature $T'_{vd}$ .....	43
4.16 Plan view of the horizontal wind field and reflectivity field for 1847 MDT at 0.5 km.....	45
4.17 Same as Fig 4.16, except for vertical velocity.....	46
4.18 Plan view of the horizontal wind field and reflectivity field for 1847 MDT at 0.75 km.....	47
4.19 Same as Fig 4.18 except, for vertical velocity.....	49

4.20	Plan view of the horizontal wind field and reflectivity field for 1847 MDT at 1 km.....	50
4.21	Plan view of the horizontal wind field and reflectivity field for 1850 MDT at 0.25 km.....	53
4.22	Same as Fig 4.21, except for pressure $P'_d$ .....	55
4.23	Plan view of the vertical velocity field for 1850 MDT at 0.5 km.....	57
4.24	Same as Fig 4.23, except for pressure $P'_d$ .....	58
4.25	Same as Fig 4.23, except for temperature $T'_{vd}$ .....	59
4.26	Plan view of the horizontal wind field and reflectivity field for 1850 MDT at 0.75 km.....	61
4.27	Plan view of the horizontal wind field and reflectivity field for 1850 MDT at 1 km.....	62
4.28	Plan view of the horizontal wind field and reflectivity field for 1850 MDT at 1.25 km.....	64
4.29	Same as Fig 4.28, except for pressure $P'_d$ .....	65
4.30	Plan view of the horizontal wind field and reflectivity field for 1845 MDT at 0.25 km The axes of the NW-SE and E-W cross-sections are shown by lines A-B and C-D.....	67
4.31	NW-SE cross-section of the reflectivity field for 1845 MDT.....	69
4.32	NW-SE cross-section of the vertical velocity field for 1845 MDT.....	70
4.33	Same as Fig 4.32, except for pressure $P'_d$ .....	72
4.34	Same as Fig 4.32, except for temperature $T'_{vd}$ .....	73
4.35	NW-SE cross-section of the reflectivity field for 1847 MDT.....	75
4.36	Same as Fig 4.35, except for vertical velocity.....	76
4.37	NW-SE cross-section of the reflectivity field for 1850 MDT.....	78
4.38	Same as Fig 4.37, except for vertical velocity.....	79
4.39	Same as Fig 4.37, except for pressure $P'_d$ .....	80

4.40	Same as Fig 4.37, except for temperature $T'_{vd}$ .....	82
4.41	E-W cross-section of the reflectivity field for 1845 MDT.....	84
4.42	Same as Fig 4.41, except for vertical velocity.....	86
4.43	Same as Fig 4.41, except for pressure $P'_{vd}$ .....	87
4.44	E-W cross-section of the reflectivity field for 1847 MDT.....	89
4.45	Same as Fig 4.44, except for vertical velocity.....	90
4.46	E-W cross-section of the reflectivity field for 1850 MDT.....	92
4.47	Same as Fig 4.46, except for vertical velocity.....	93
4.48	Same as Fig 4.46, except for pressure $P'_d$ .....	95
4.49	Same as Fig 4.46, except for temperature $T_{vd}$ .....	96
4.50	Plan view of the horizontal wind field and pressure field (tendency included) for 1845 MDT at 0.25 km.....	99
4.51	Same as Fig 4.50, except for temperature $T_{vd}$ .....	100
4.52	Same as Fig 4.50 except for 0.5 km.....	102
4.53	Same as Fig 4.51 except for 0.5 km.....	103
4.54	Same as Fig 4.50 except for 0.75 km.....	104
4.55	Same as Figure 4.50 except for 1 km.....	106
4.56	Same as Figure 4.51 except for 1 km.....	107
4.57	Same as Figure 4.51 except for 1.25 km.....	108
4.58	Plan view of the horizontal wind field and pressure field (tendency included) for 1847 MDT at 0.25 km.....	110
4.59	Plan view of the temperature field (tendency included) for 1847 MDT at 0.25 km.....	111
4.60	Same as Fig 4.58, except for 0.5 km.....	113
4.61	Same as Fig 4.59, except for 0.5 km.....	114
4.62	Same as Fig 4.60, except for 0.75 km.....	115

4.63	Same as Fig 4.62, except for 1 km.....	117
4.64	Plan view of the horizontal wind field and pressure field (tendency included) for 1850 MDT at 0.25 km.....	119
4.65	Plan view of the temperature field (tendency included) for 1850 MDT at 0.25 km.....	120
4.66	Same as Fig 4.64, except for 0.5 km.....	121
4.67	Same as Fig 4.64, except for 0.75 km.....	123
4.68	Same as Fig 4.64, except for 1.25 km.....	124
4.69	NW-SE cross-section of the pressure field (tendency included) for 1845 MDT.....	127
4.70	NW-SE cross-section of the temperature field (tendency included) for 1845 MDT.....	129
4.71	NW-SE cross-section of the pressure field (tendency included) for 1847 MDT.....	131
4.72	NW-SE cross-section of the temperature field (tendency included) for 1847 MDT.....	132
4.73	NW-SE cross-section of the pressure-field (tendency included) for 1850 MDT.....	134
4.74	NW-SE cross-section of the temperature field (tendency included) for 1850 MDT.....	135
4.75	E-W cross-section of the pressure field (tendency included) for 1845 MDT.....	137
4.76	E-W Cross-section of the temperature field (tendency included) at 1845 MDT.....	138
4.77	E-W cross-section of the pressure field (tendency included) for 1847 MDT.....	140
4.78	E-W cross-section of the temperature field (tendency included) for 1847 MDT.....	141
4.79	E-W cross-section of the pressure field (tendency included) at 1850 MDT.....	143
4.80	E-W cross-section of the temperature field (tendency included) at 1850 MDT.....	144

## 1. Introduction

The microburst, a divergent horizontal wind flow near the surface, was identified by Fujita (1976) and further studied by many authors including Wilson et al. (1984). Fujita coined the name "microburst" to identify a distinctive downdraft that produces an outflow of damaging horizontal winds at the surface extending up to 4 km in diameter. This basic definition was refined by Wilson et al. (1984) to include a differential wind velocity of the divergent outflow at the surface greater than 10 m/s within the 4 km diameter.

A microburst is thus an enhanced downdraft of air within a 4 km diameter capable of producing intense, damaging low-level winds. Across the microburst center, the differential outflow velocity at the surface is more than 10 m/s, and the maximum distance between outburst flows and approaching/receding centers is less than 4 km (Wilson et al. 1984). This criterion distinguishes a microburst from a downdraft that does not reach the surface to spread its outflow horizontally.

The microburst is capable of causing aircraft crashes due to the strong diverging horizontal winds and shear that results when the downdraft reaches the surface. This low-altitude wind shear hazard was tragically highlighted



with the crash of Eastern Airlines Flight 66 on approach to JFK Airport in New York on 24 June 1975. The crash was caused by an intense small-scale downdraft descending to the surface and spreading out horizontally: a microburst (Fujita, 1977). The sharp changes in both horizontal and vertical wind speed and direction as a result of a microburst and its associated turbulence at the gust front can be hazardous to aircraft, especially during takeoffs and landings.

Microbursts were studied extensively in the Northern Illinois Meteorological Research on Downbursts (NIMROD) Program (1978) and also during the Joint Airport Weather Studies (JAWS) Project (1982). In these studies, microbursts were studied using Doppler radar observations of the diverging outflow near the surface. Many authors have studied the effects of convective storms and the organizing systems that can produce microbursts and the damaging winds they can produce in such short time over a small scale. The kinematic structure of JAWS microbursts were studied by Wilson et al. (1984), Hjelmfelt (1987,88), and many others.

The JAWS Program was undertaken in the summer of 1982 in the vicinity of Denver's Stapleton International Airport to study the development of convective storms and the microbursts they produced. The site was chosen because of

the almost daily convective thunderstorms that occur as a result of Stapleton's proximity to the front-range of the Rockies and the orographics that enhance the effects of thermal lifting of air parcels. The late afternoon thunderstorms that are so common during the summer in Denver provide an ideal location for the study of microbursts occurring in convective storms.

The JAWS project was held during the summer of 1982 to focus specifically on the microburst phenomenon. Wilson et al. (1984) identified more than 70 microbursts in the Denver area from 15 May through 9 August 1982. They found that a typical JAWS microburst has the horizontal dimension of 1 to 3 km, a lifetime of 5 to 14 minutes and a period of severe shear from 2 to 4 minutes. It produces an average wind differential of approximately 25 m/sec. The primary instruments used for the JAWS project were three pulsed Doppler radars: CP-2 (10cm), CP-3 and CP-4 (both 5 cm). Analysis of the 5 August case microbursts was done using a dual-Doppler analysis. The scanning strategy for the two radars consisted of coordinated constant elevation sector scans that began and ended at nearly identical times. This study will use three August 5 time periods: 1845, 1847 and 1850 MDT. Two microbursts and one enhanced downdraft that does not reach the surface will be examined to study the microburst phenomenon that is so common during convective storms.

## 2. Statement of the Problem

The objective of this paper is to increase understanding of microburst structure, evolution and development using a summertime storm that occurred on 5 August 1982.

The microburst-producing storm was measured by dual-Doppler radar operating as a part of the JAWS project. Data for three time periods of 5 August are studied: 1845, 1847, and 1850 (MDT). Within the time window, there is one main microburst, M1, and a rapidly developing second microburst, M3. There is also an enhanced downdraft, D2, present throughout the period. Recall that a downdraft is a rapid flow of cool downwardly-moving air that does not extend to the surface.

Many have investigated microburst producing convective storms using dual-Doppler JAWS data. Elmore *et al.* (1986) studied the storm on 5 August 1982, with emphasis on M1 and its associated wind shear effects. Coover's Ph.D. dissertation (1988) studied the microburst-producing convective storm on 5 August. His study detailed microburst structure within the 1845-1850 time period. His research included computing perturbation temperature and pressure fields, budgets of momentum flux and eddy kinetic energy. Coover studied the 1845 to 1850 period exten-

sively, but he was unable to analyze the storm at the 1847 time period; thus, there is a five minute period between complete radar scans. This report will study microburst structure during the 1845-1850 time frame, with emphasis on the intermediate time period of 1847.

Data for one of the Doppler radars at 1847 is unusable. To allow analysis of the 1847 time period, a data set for both radars is necessary. To compensate for the missing radar's data at 1847, a composite, linearly interpolated data set using the results at 1845 and 1850 to represent the missing 1847 data is computed.

The addition of the 1847 time period allows use of the local time tendency term in the momentum equations, thereby producing greater detail in the recovered perturbation pressure and temperature fields. Use of three time periods allows small enough time intervals to make the inclusion of local tendencies desirable. Forward tendencies from 1845 to 1847 (2 minutes) and backward tendencies from 1850 to 1847 (3 minutes) are included in the momentum equations for the 1845 and 1850 time periods (respectively). The 1847 time period uses a forward difference from 1847 to 1850 (3 minutes). Using local time tendencies will allow a more thorough study of the microbursts because of enhanced perturbation pressure and temperature fields.

The goal of this report is to investigate microburst development and structure with:

1). Use of the intermediate time period 1847 to more thoroughly study microburst development within the 1845-1850 time period.

2). Use of thermodynamic fields enhanced by the inclusion of local time tendencies in the momentum equations for all three periods to obtain detailed perturbation temperature and pressure fields.

### 3. Methodology

Dual-Doppler radar was used to collect raw data from two sites near Denver's Stapleton Airport on the afternoon of 5 August 1982. Shallow volume scans (5 levels) were centered on times 1845, 1847 and 1850 MDT. Due to an equipment problem, the CP-3 radar was unable to properly obtain data for the 1847 period, although there were no problems encountered with either radar at 1845 or 1850. To compensate for the missing 1847 data, the linearly averaged composite of the CP-3 data at 1845-1850 was used to represent the CP-3 radar at 1847.

There were 5 analysis levels ranging from 0.25 to 1.25 km, with 0.25 km of spacing between scans vertically. The horizontal spacing was 0.5 km, while the vertical spacing was 0.25 km. Shallow volume scans with five layer, 0.25 km vertical resolution is well suited for the study of the microburst phenomenon. The data from the radar scan is collected in radial form.

### 3.1 Data Analysis Techniques

The raw data from the Doppler return signal is processed according to the procedure outlined by Lin and Pasken (1982) as follows:

- 1). Conversion of radar data from spherical to Cartesian coordinates.
- 2). Values exceeding pre-set tolerances are eliminated and "folded" velocities are corrected.
- 3). Interpolation to a two-dimensional array.
- 4). Three-dimensional wind field is computed from the gridded fields.
- 5). Thermodynamic retrieval is performed.
- 6). Evaluation of displayed results.

Dual-Doppler data were analyzed to produce a detailed wind field. Processed radar data is composed of radial velocities from the two radars and reflectivity, which will be used to compute vertical velocity. Synthesis of the wind field from the dual-Doppler data was formulated by Armijo (1969). He is able to accurately determine the three components of wind velocity using the equation of continuity that identifies a point in the three-dimensional  $(U,V,W)$  wind field. The Armijo method derives the horizontal wind components  $(U,V)$  from radial velocities produced by the received radar signal. Vertical velo-

cities ( $W$ ) are computed from the anelastic continuity equation.

Once the detailed wind field is derived, fields of deviation pressure and virtual temperature were retrieved. The fields of deviation perturbation pressure and virtual temperature were recovered via the thermodynamic retrieval method of Gal-Chen (1978). He used the momentum equations and the detailed wind field to compute the perturbation pressure and temperature at each horizontal level. He also suggests a verification method based on momentum checks to estimate relative errors in the recovered pressure field at each level.

Gal-Chen's method of thermodynamic retrieval uses the momentum equations and the observed 3-D wind field to determine pressure and temperature fluctuations. His technique recovers the perturbations of pressure and temperature using the momentum equations, which can be written for a moving coordinate system as follows:

$$\partial p' / \partial x = -\bar{\rho}(DU/DT) + f_x = F \quad (1)$$

$$\partial p' / \partial y = -\bar{\rho}(DV/DT) + f_y = G \quad (2)$$

$$\partial p' / \partial z = -\bar{\rho}(DW/DT) - \rho g + f_z = H \quad (3)$$

where the primed quantities represent perturbation quantities.  $DU/DT$ ,  $DV/DT$  and  $DW/DT$  are accelerations in the  $X$ ,



Y, and Z axes, respectively.

These momentum equations can be broken down as follows into their local quantities. The momentum equations in a Cartesian coordinate system are written as:

$$\partial u / \partial t = -u(\partial u / \partial x) - v(\partial u / \partial y) - w(\partial u / \partial z) - 1/\bar{\rho}(\partial p' / \partial x) + f_x \quad (4)$$

$$\partial v / \partial t = -u(\partial v / \partial x) - v(\partial v / \partial y) - w(\partial v / \partial z) - 1/\bar{\rho}(\partial p' / \partial y) + f_y \quad (5)$$

$$\partial w / \partial t = -u(\partial w / \partial x) - v(\partial w / \partial y) - w(\partial w / \partial z) - 1/\bar{\rho}(\partial p' / \partial z) + f_z \quad (6)$$

where  $f_i$  represents forces other than the pressure gradient force per unit mass, primarily friction.

From (4) and (5), the horizontal pressure perturbations can be written as follows:

$$\partial p' / \partial x = -\bar{\rho}\{u(\partial u / \partial x) + v(\partial u / \partial y) + w(\partial u / \partial z) + (\partial u / \partial t) + f_x\} = F \quad (7)$$

$$\partial p' / \partial y = -\bar{\rho}\{u(\partial v / \partial x) + v(\partial v / \partial y) + w(\partial v / \partial z) + (\partial v / \partial t) + f_y\} = G \quad (8)$$

It is seen from (7) and (8), that the local time tendency terms  $(\partial u / \partial t)$  and  $(\partial v / \partial t)$  are factors in the momentum equations. In general, the local acceleration terms are comparable in magnitude to the advective acceleration terms.

In the horizontal perturbation pressure equation,  $P'$  is obtained by use of successive over-relaxation (SOR) with the Newmann boundary condition. This involves solving the following partial differential equation as (7) is differentiated with respect to  $x$ , and (8) is differentiated with respect to  $y$ :

$$(\partial^2 P' / \partial x^2) + (\partial^2 P' / \partial y^2) = (\partial F / \partial x) + (\partial G / \partial y) \quad (9)$$

Gal-Chen (1978) noted that a unique solution to (9) exists only if the average perturbation pressure for that horizontal level, denoted by  $\langle P' \rangle$ , is removed from  $P'$  of (9). The deviation perturbation pressure exists as a pressure perturbation difference from the horizontal average perturbation pressure, and is thus defined as:

$$P'_d = P' - \langle P' \rangle$$

Once the detailed field of deviation perturbation pressure ( $P'_d$ ) is obtained, the deviation virtual temperature field ( $T'_{vd}$ ) is calculated from the buoyancy equation.

### 3.2 Momentum Checks to Indicate Data Accuracy

$P'_d$  is exact only under error-free conditions. Gal-Chen and Hane (1981) proposed a measure of relative error,  $E_r$ . This relative error is considered an indicator of the data retrieval accuracy, and is a measure of the "goodness of fit" of the perturbation pressure gradients and the known functions  $F$  and  $G$ . The retrieved fields are subjected to momentum checks to determine a level of confidence of the data's accuracy before interpretation.  $E_r$  is thus a coefficient of error in pressure retrieval. Such values are used to indicate how well the derived pressure perturbations balance the dynamic equations.  $E_r$  is an indicator of the accuracy of the retrieved perturbation pressure field. Values of  $E_r$  less than 0.5 are desirable; however, it is also important to examine the physical consistency of the pressure field perturbations with respect to the storm's kinematic structure to see if the fields are in general agreement with the fields of vertical velocity and reflectivity.

The momentum check values for the 1845, 1847 and 1850 time periods using the entire 31 x 31 matrix are shown in Table 1. Local time tendency was not included in these calculations. Note that the smaller (most desirable) values of momentum checks are in the lower levels of the radar scan. Values less than 0.5 are desirable for a good

TABLE 1

Momentum Check Values (without tendency) (31 x 31 matrix )				
Ht(km)	1845 MDT	1847 MDT	1850 MDT	1850 MDT
0.250	0.3368	0.3467	0.2520	
0.500	0.3959	0.3746	0.3650	
0.750	0.3897	0.3568	0.3661	
1.000	0.3780	0.3571	0.3417	
1.250	0.4417	0.3892	0.3689	

Table 1: Momentum Check Values using a  
31 x 31 matrix (tendency not included)

momentum check, and as a general rule, the smaller the momentum check, the better the accuracy of the retrieved perturbation pressure field.

Since the 1847 time period used composited data to represent the CP-3 at 1847, there was concern of poor momentum checks indicating it is not permissible to use the composited data as a substitute for actual raw Doppler data from the field. An examination of Table 1 reveals the momentum checks for the 1847 time period are of the same general value as those from the 1845 and 1850 time periods. The averaged data at 1847 for the CP-3 radar seem to be an accurate representation of what the radar would have seen at 1847 if the CP-3 had functioned normally.

As seen in (7) and (8), inclusion of the local tendency terms,  $(\partial u / \partial t)$  and  $(\partial v / \partial t)$ , in the momentum equations should improve momentum checks and thus enrich the retrieved pressure perturbation field. To avoid the inadvertent use of unreasonable values of local time tendencies, an upper and lower limit of  $(\pm 4 \times 10^{-2} \text{ m/s}^2)$  was used to eliminate values of  $(\partial u / \partial t)$  and  $(\partial v / \partial t)$  that are not physically reasonable. This number was based on a 5 m/s change in the horizontal wind over a two minute period. Also, a five-point smoothing technique was used to eliminate spurious data spikes that can occasionally

occur in the retrieved velocity fields used to calculate local time tendencies.

The values of momentum checks obtained after including the local time tendency terms are shown in Table 2. Note that at some levels, the values of momentum check actually worsened with the addition of the local tendency terms. This is probably due to data of poor quality near the outer limits of the matrix at a particular level. Reducing the matrix by two rows and columns from 31 x 31 to 27 x 27 should eliminate most spurious noise and data of questionable quality near the edges of each matrix.

Table 3 also shows the result of eliminating two rows and columns from each matrix and how the accuracy of momentum check at virtually every level improved. Of course, not all of the data eliminated in such a matrix reduction is of poor quality, and there is always the possibility of rejecting valuable data. Eliminating authentic data would cause momentum checks to deteriorate. Fortunately, the momentum checks listed in Table 3 indicate most of the data eliminated in the matrix reduction was of questionable quality and purging it improved momentum checks, especially in the lower levels.

TABLE 2

Momentum Check Values (with tendency) (31 x 31 matrix )				
Ht(km)	1845 MDT	1847 MDT	1850 MDT	
0.250	0.3287	0.2981	0.2273	
0.500	0.3920	0.4226	0.3789	
0.750	0.4061	0.4440	0.4226	
1.000	0.4125	0.4035	0.3702	
1.250	0.4147	0.4547	0.3692	

Table 2: Momentum Check Values using a  
31 x 31 matrix (tendency included)

TABLE 3

Momentum Check Values (with tendency) (27 x 27 matrix )				
Ht(km)	1845 MDT	1847 MDT	1850 MDT	
0.250	0.2904	0.2071	0.2813	
0.500	0.3879	0.3400	0.3813	
0.750	0.4061	0.3873	0.3913	
1.000	0.3851	0.3396	0.3412	
1.250	0.4015	0.3279	0.3915	

Table 3: Momentum Check Values using a  
27 x 27 matrix (tendency included)



The addition of the local time tendency terms ( $\partial u/\partial t$ ) and ( $\partial v/\partial t$ ) in the momentum equations yielded improved momentum checks at virtually all levels. These improved momentum values indicate the retrieved perturbation pressure field obtained with the momentum equations that included local time tendency terms will be a more accurate representation of the physical variables present in the microburst, and a more complete representation of the storm's structure. The improved thermodynamic fields will demonstrate desirability of including local time tendency terms in the momentum equations used to derive perturbation pressure.

#### 4. RESULTS

Horizontal plots of the wind flow field, reflectivity, vertical velocity, deviation perturbation pressure and temperature are used to analyze the storm. The first vertical level plotted is 0.25 km, with subsequent plots at 0.25 km intervals, up to an upper-most level of 1.25 km. In addition to the horizontal plan view plots, two vertical slices were taken of the domain of interest to obtain cross-section plots.

##### 4.1 Plan View Plots (tendency not considered)

This series of horizontal plots will be done omitting the local time tendency terms in the momentum equations used to derive the pressure and temperature fields. These horizontal plots are centered on the scan times of 1845, 1847 and 1850 MDT, and take incremental horizontal slices of 0.25 km up to the top layer of 1.25 km. With a 0.5 km grid spacing for each horizontal slice, enough detail is obtained to allow study of the sub-cloud layer and adequately detail the microburst.

#### 4.1.1 1845 Plan View Plots

The plan view for the 0.25 km horizontal wind and reflectivity fields are shown in Figure 4.1. Distances are in kilometers from the CP-2 radar. The figure shows that the microburst, M1, and the downdraft, D2, occur in the reflectivity areas greater than 50 dBz. M1 is located at ( $x = -2$ ,  $y = -23.5$ ). D2 is located to the northwest of M1 at ( $-6$ ,  $-19.5$ ). The environmental mean flow is from  $220^\circ$  at 3 m/s. The gust front resulting from M1's outflow is shown with a dashed line. Note that a cyclonic circulation (C) is present at the southern end of the gust front ( $0$ ,  $-25.5$ ). At the 0.25 km level, there is no manifestation of outflow from D2 as there is from the microburst. The diverging outflow of M1 is clearly shown, and the absence of a divergent outflow at the surface associated with the downdraft is apparent. Microbursts are usually found at the highest values of reflectivity. The microburst and the downdraft are both identified as areas with high reflectivity. This high reflectivity is due to hydrometeors such as rain and/or hail in the downwardly-moving rain shaft.

The vertical velocity for this level at 1845 is shown in Figure 4.2. Note the downward vertical motion ( $-0.6$  m/s) associated with M1, as well as upward vertical motion as a result of convergence along the gust front. The negative vertical motion associated with the downdraft is

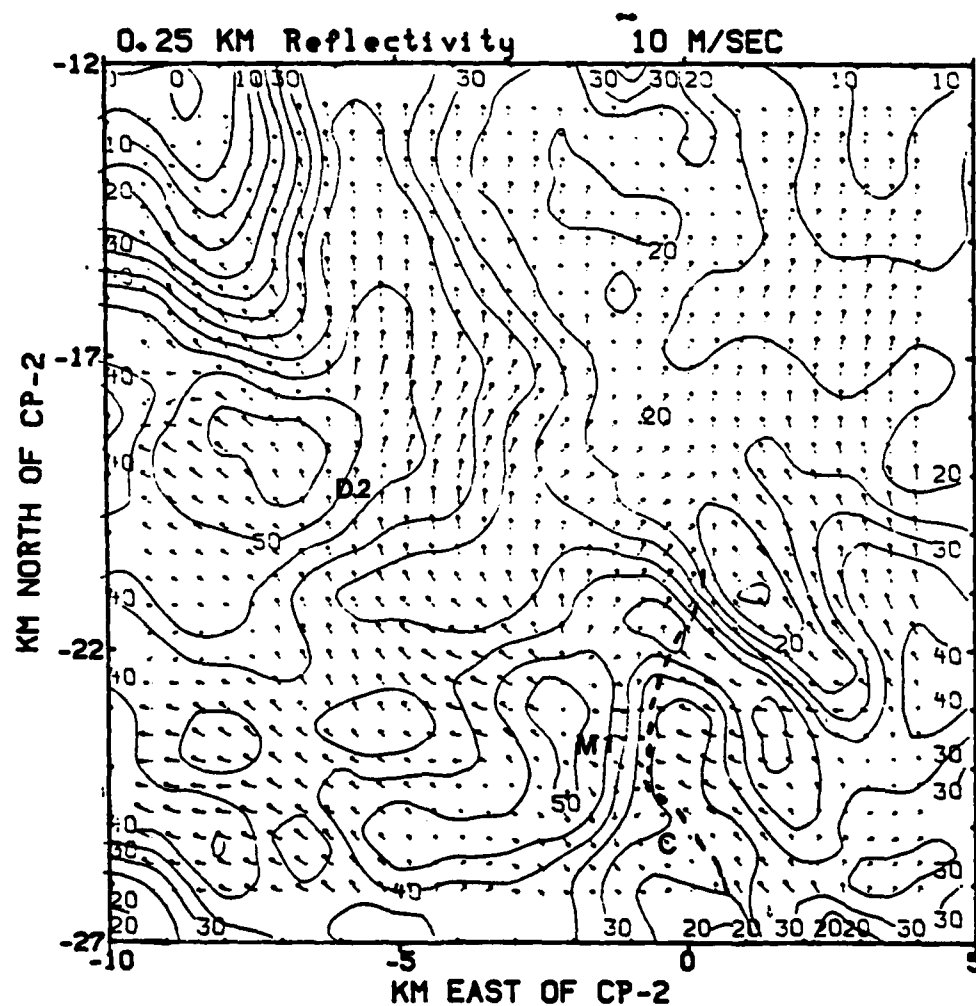


Fig 4.1 Plan view of the horizontal wind field and reflectivity field for 1845 MDT at 0.25 km.

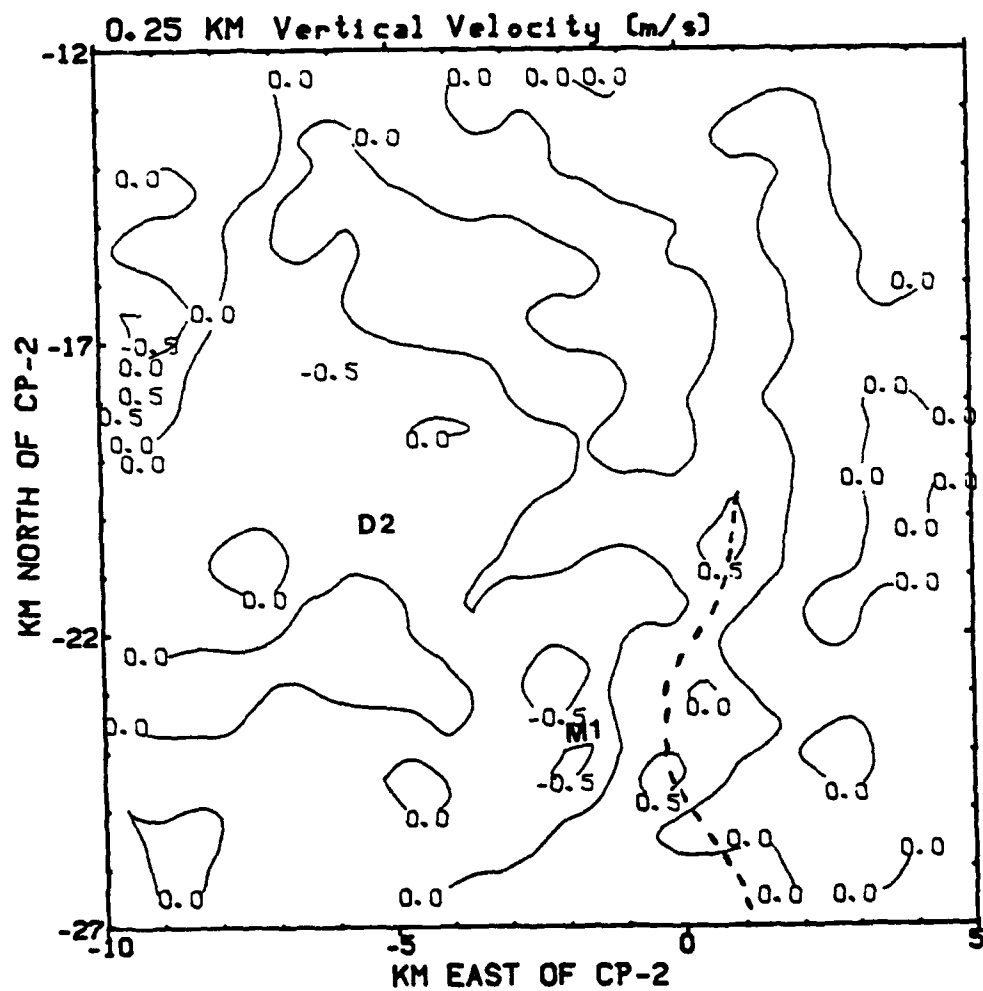


Fig 4.2 Same as Fig 4.1, except for vertical velocity.

not being felt at this level, and downward motion associated with D2 is absent at the lowest level.

The perturbation pressure field for the 0.25 km layer at 1845 is shown in Figure 4.3. The microburst has a well-defined surface meso-high where the downflow converges near the surface (-2, -24). Just to the east, outflow from M1 converges with the environmental flow to form the gust front, as designated by the dashed line. Although the wind flow pattern shows D2's downwardly-moving flow has not yet reached the surface, as evidenced by the non-disrupted environmental flow near D2, the downdraft does cause positive pressure perturbations at the 0.25 km level. This indicates downward vertical motion must be taking place in the layer(s) above.

The temperature of the 1845 time period for 0.25 km is shown in Figure 4.4. The microburst has a well-defined cold core at 0.25 km as the downwardly-moving cooler air converges toward the surface. The air is cooled because its velocity is slow enough that it can ventilate the downdraft and cool via evaporative cooling. The cool downdraft of D2 is not clearly shown based on this temperature plot, since the downdraft does not extend to the 0.25 km level.

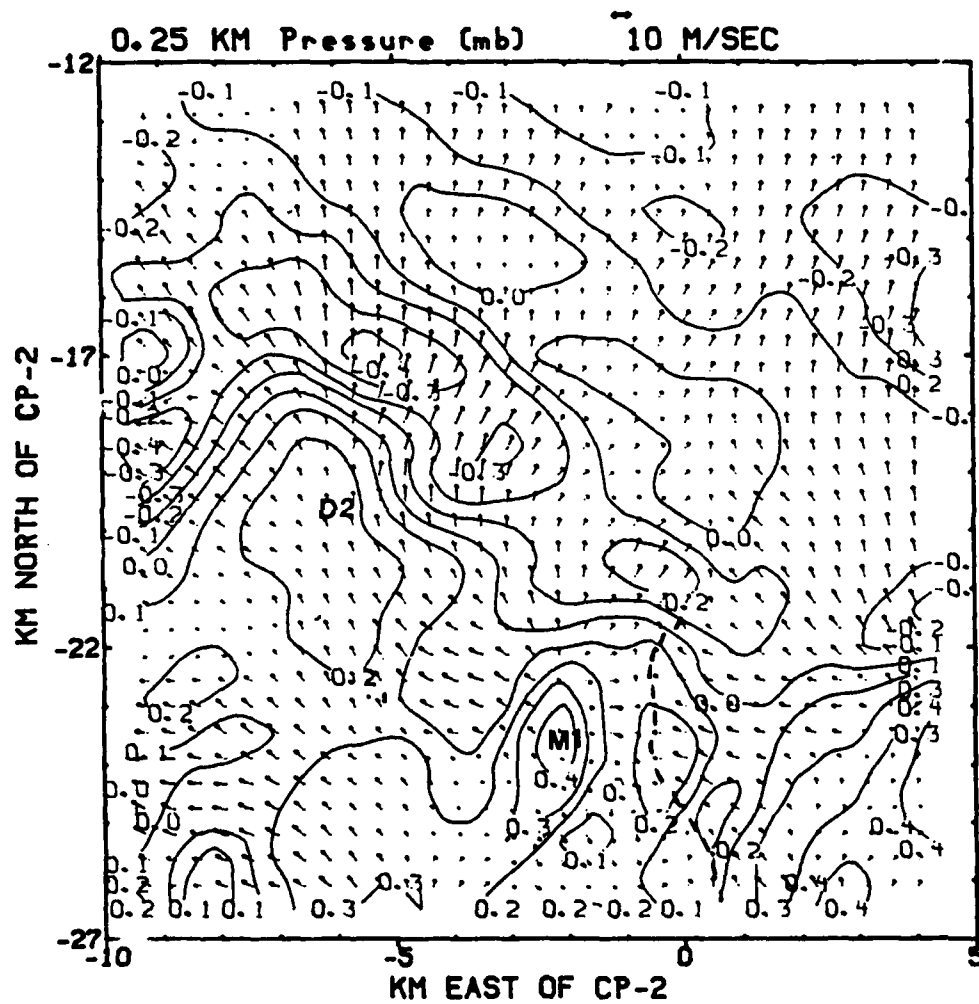


Fig 4.3 Same as Fig 4.1, except for pressure  $P'_d$ .

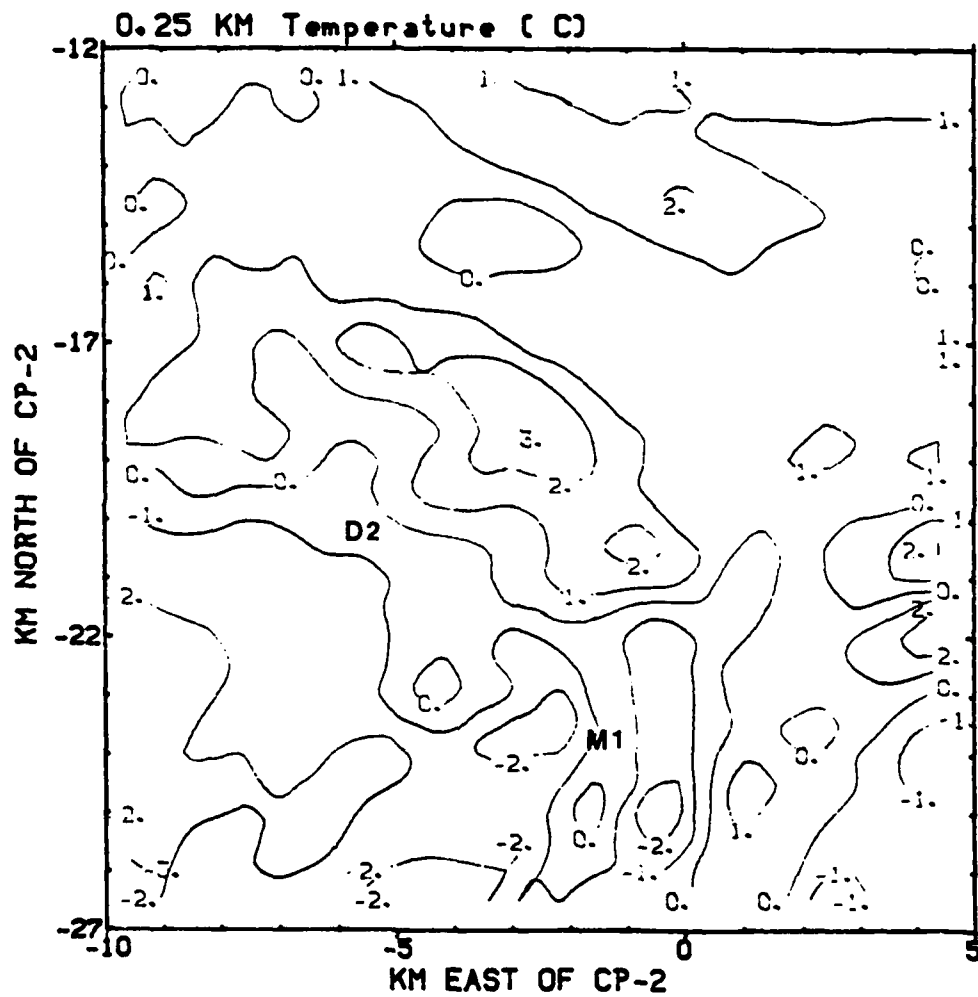


Fig 4.4 Same as Fig 4.1, except for temperature  $T'_{vd}$ .



Because the temperature plot did not consider tendency in the thermodynamic retrieval calculations, the temperature and pressure fields will not be as concise and accurate as they will with the tendency included cases, which will be discussed in Section 4.3 of the thesis.

The second level to be considered for the 1845 period is 0.5 km. The reflectivity field, shown in Figure 4.5, reveals that both D2 and M1 are shown to be areas of high reflectivity. At (1.5, -23), a second microburst, to be labelled M3, will rapidly develop in the coming minutes in the high reflectivity area of 50 dBz, which indicates the presence of a precipitation-laden downdraft. Based on high reflectivities at 0.25 and 0.5 km, it is apparent that this area could be a developing downdraft or microburst. There is no divergent outflow from this new high reflectivity area, so it is not obvious that a microburst may be forming. A closer examination of this area during the next five minutes will allow the study of the rapidly developing microburst.

The vertical velocity field for 0.5 km is displayed in Figure 4.6. The sinking area in the vicinity of M1 shows it to be an area of negative vertical velocity. D2 is not yet apparent at this level, so the downdraft has not extended itself to this level at 1845. Note that a relatively weak value of -1 m/s vertical motion associated

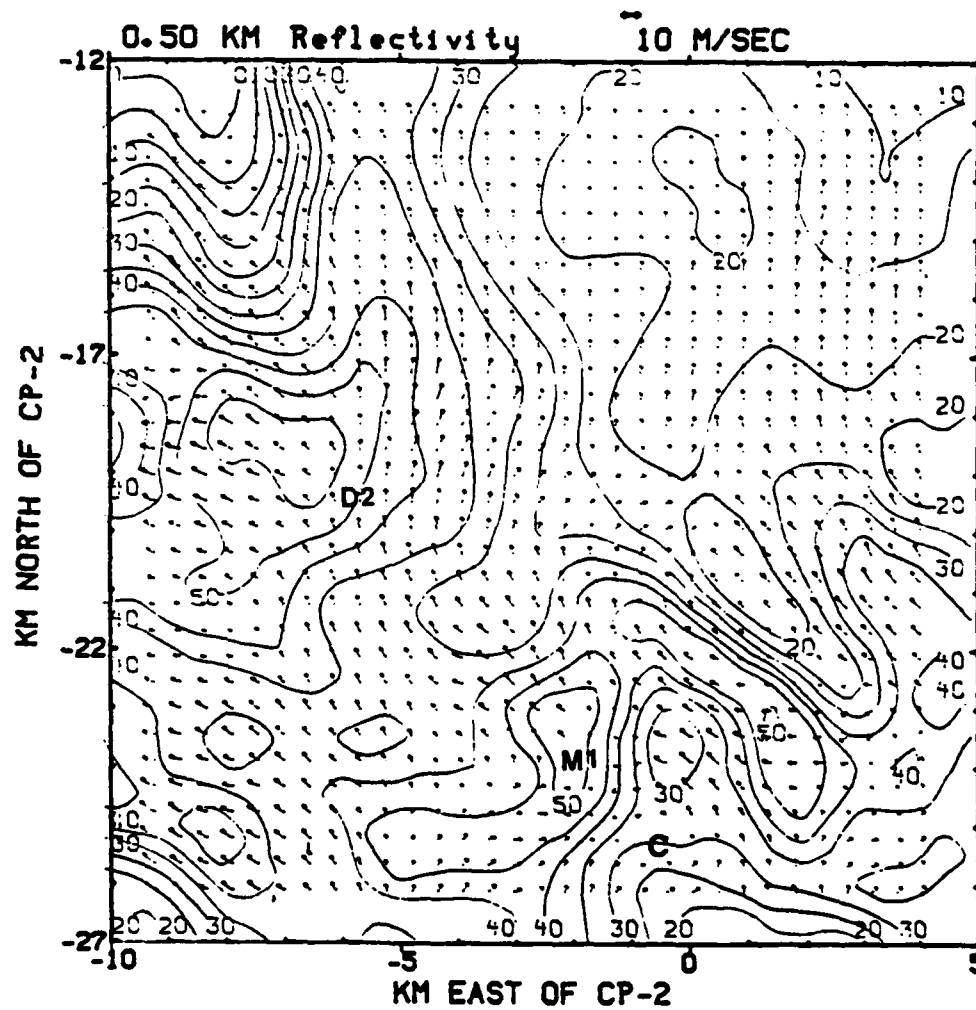


Fig 4.5 Plan view of the horizontal wind field and reflectivity field for 1845 MDT at 0.5 km.

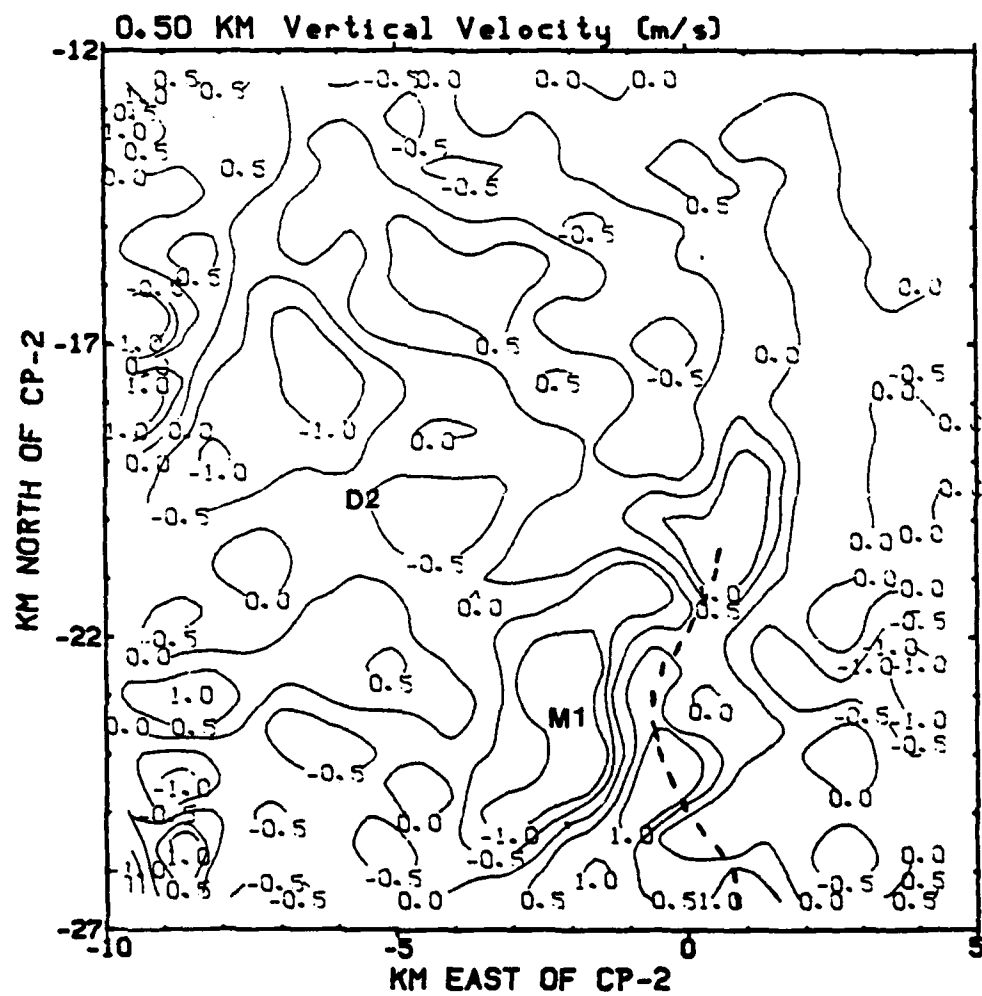


Fig 4.6 Same as Fig 4.5, except for vertical velocity.

with D2 is near the area of highest reflectivity. Both M1 and D2 are located in areas of sinking motion, although M1 is stronger at this level.

The next level for the 1845 case is 0.75 km. The horizontal wind field is shown in Figure 4.7. Unlike the two levels below, the mean flow is almost exclusively environmental wind from the southeast. This level does not seem to support entrainment into the downdraft, as evidenced by the non-attraction of the environmental wind to the downdraft. At this level, the downdraft and the environmental flow seem to act independently of each other and have little interaction. The cyclonic circulation at (-1.5, -25) is still apparent and its radius of circulation has increased.

The 1 km wind flow is shown on Figure 4.8. The wind field is beginning to show a pattern of flow from areas of low to high reflectivity. Entrainment of dry air is beginning to occur at the 1 km level, as the flow is turning toward the descending precipitation shaft. The cyclonic circulation that was apparent in the first three levels in the vicinity of (-1.5, -25) is not obvious at this level. The area of strong reflectivity associated with the developing microburst/downdraft to the east of M1 continues to show strong values of reflectivity.

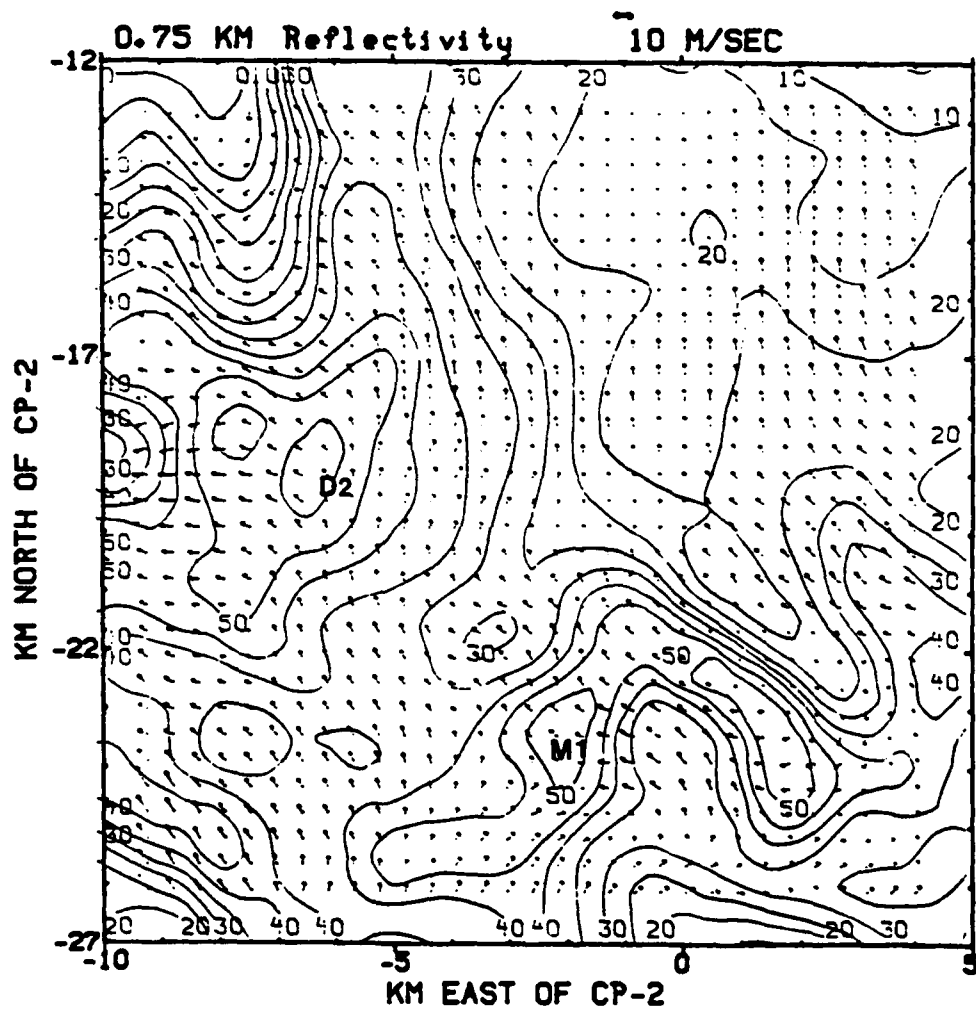


Fig 4.7 Plan view of the horizontal wind field and reflectivity field for 1845 MDT at 0.75 km.

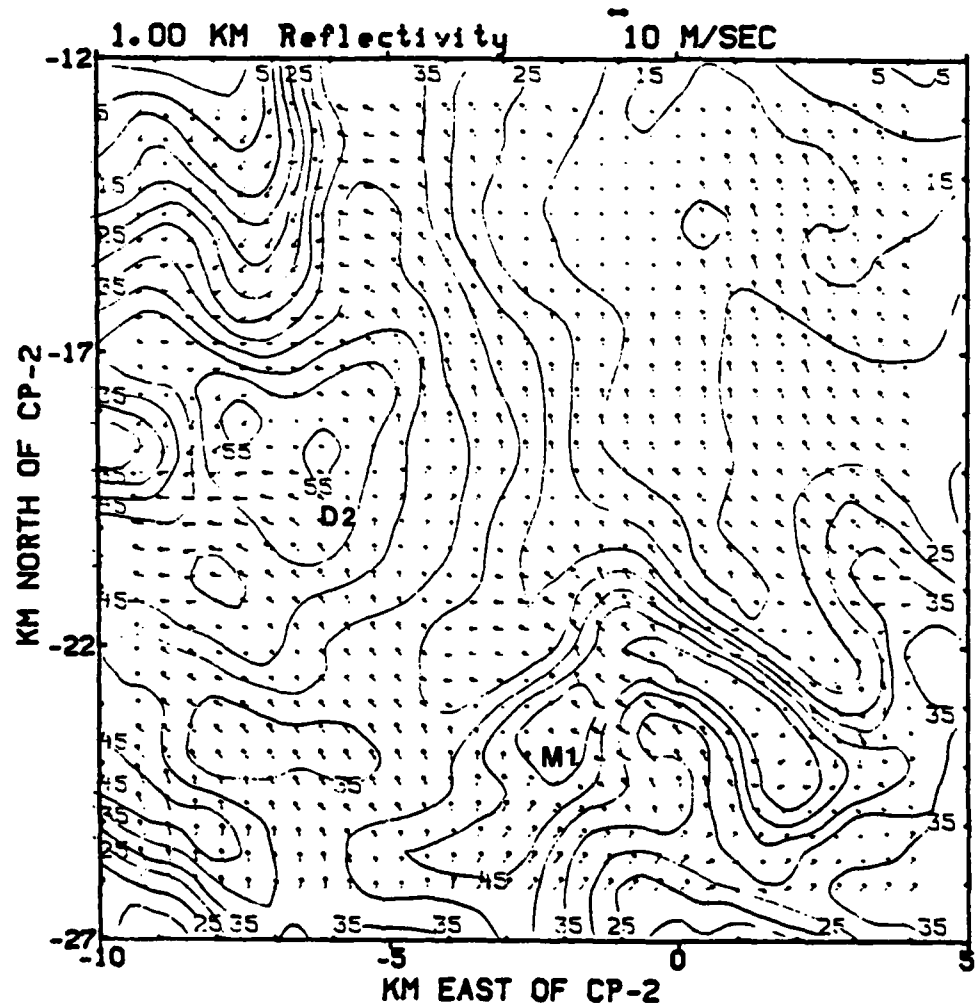


Fig 4.8 Plan view of the horizontal wind field and reflectivity field for 1845 MDT at 1 km.

The vertical velocity field for 1 km is shown in Figure 4.9. M1 and D2 show vigorous downward vertical motion. The high reflectivity region to the east of M1 shows no obvious vertical velocity, and shows no signs yet of developing into a larger downdraft, or into extending to the surface to form a microburst. There is no obvious flow of environmental flow toward this region, so it has not yet begun to entrain dry air into the rain-shaft. For this time period, this region is nothing more than an area of high reflectivity that should continue to develop throughout the period.

The wind field for 1.25 km is shown in Figure 4.10. Note the general cyclonic turning of the winds around both M1 and D2. Both are collecting and funneling dry environmental air into the downward-moving shaft each possesses. Such dry air will enhance evaporative cooling, especially near the outside edges of the downdrafts. As the cooling process increases, the strength of the downflow should increase. This environmental air being entrained into the downdraft will bring its upper level momentum to the surface and thus strengthen the outflow velocity.

The vertical motion field for the 1.25 km level is shown in Figure 4.11. Note the area of downward vertical motion near both M1 and D2. In the area to the east of M1 (0, 25.5), the high reflectivity area is beginning to show

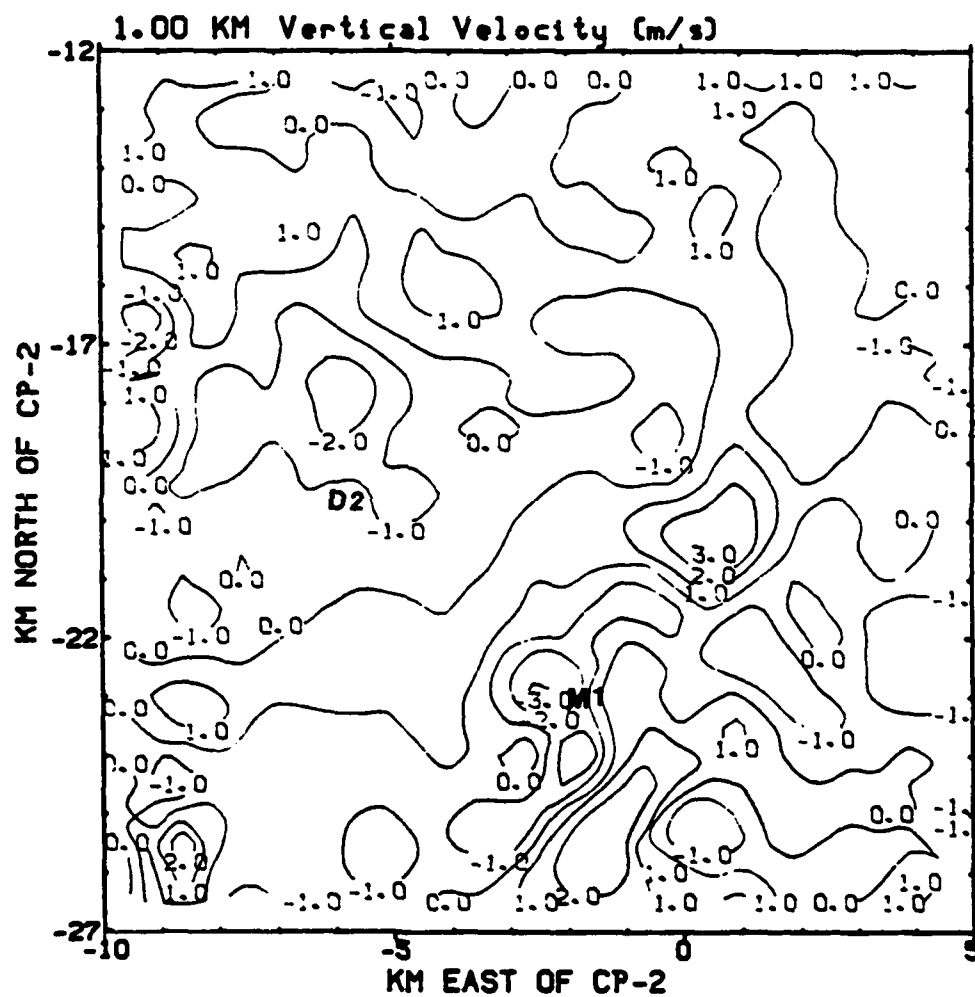


Fig 4.9 Same as Fig 4.8 except for vertical velocity.



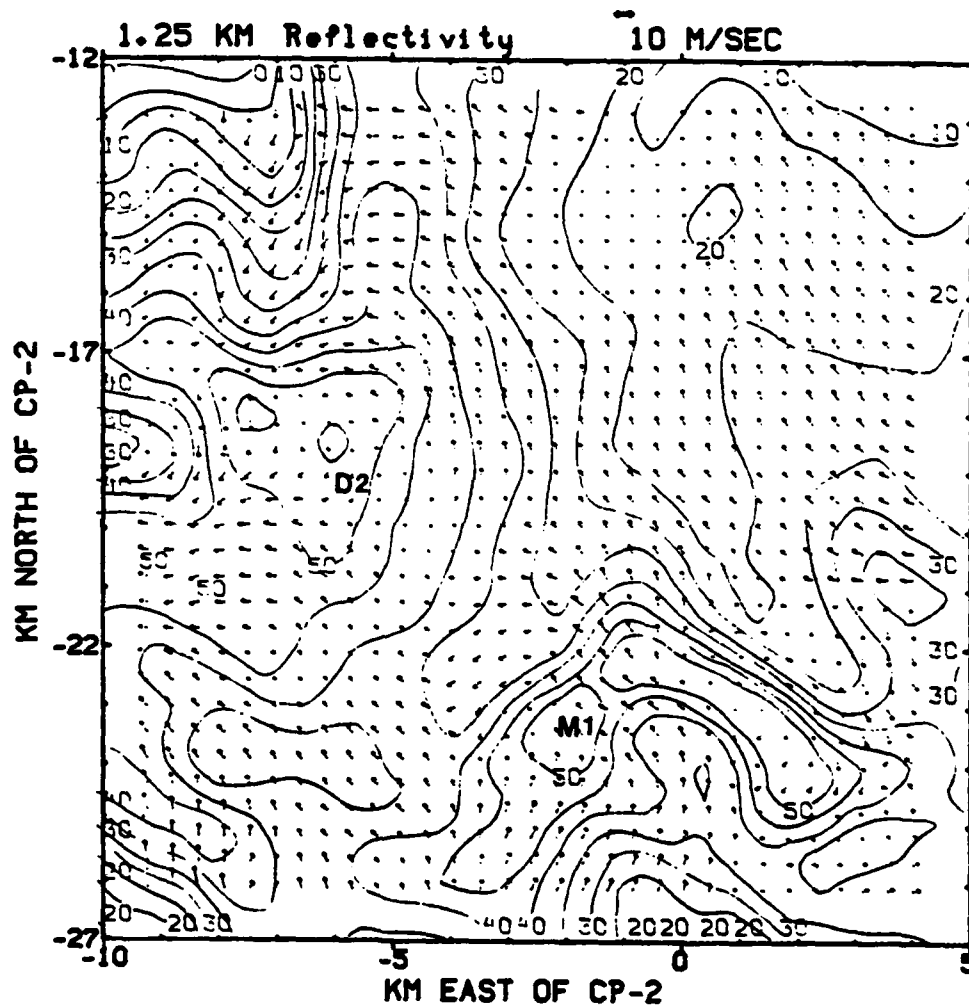


Fig 4.10 Plan view of the horizontal wind field and reflectivity field for 1845 MDT at 1.25 km.

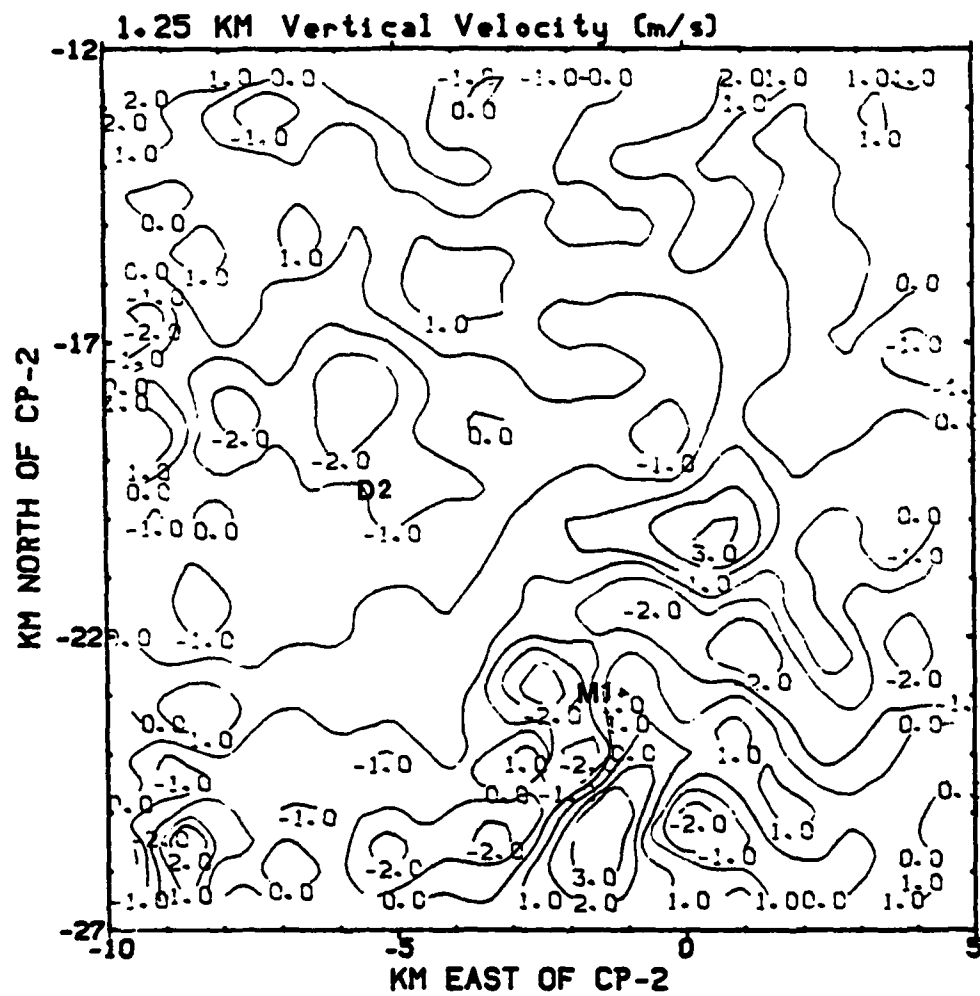


Fig 4.11 Same as Fig 4.10, except for vertical velocity.

development as the negative vertical motion becomes apparent ( $-2.0$  m/s). The outflow from M1 should help to feed the inflow of positive vertical velocity in the area of  $(-1.5, -26)$ .

#### 4.1.2 1847 Plan View Plots

Plan views of the 1847 time period will now be studied, which is two minutes later than the previously discussed time period. Data collection for 1847 was incomplete because the CP-3 radar was unable to receive data due to equipment malfunctions. To obtain usable data for the 1847 time period, a linearly-averaged composite data set was computed using results from 1845 and 1850. Momentum checks of the 1847 perturbation pressure indicate the CP-3 composite arrangement for the 1847 radar scan is a valid representation of the time period. The CP-4 radar set functioned normally throughout the entire time period under study, and data was retrieved in the normal fashion with no difficulties.

The reflectivity and wind flow plot for the 1847 time period (tendency not considered) is shown in Figure 4.12. The 50 dBz contours identify the three areas of interest: M1, M3 and D2. Just as at 1845, the development of M1 is vigorous, and the pronounced divergent outflow continues from M1. There is no indication of such an outflow from M3, but the flow has become slightly divergent at 0.25 km, nonetheless. The high reflectivity area associated with M3 has also grown. The reflectivity in this area has increased from 40 to 50 dBz since the 1845 scan, representing a 10 dBz increase in only two minutes. The

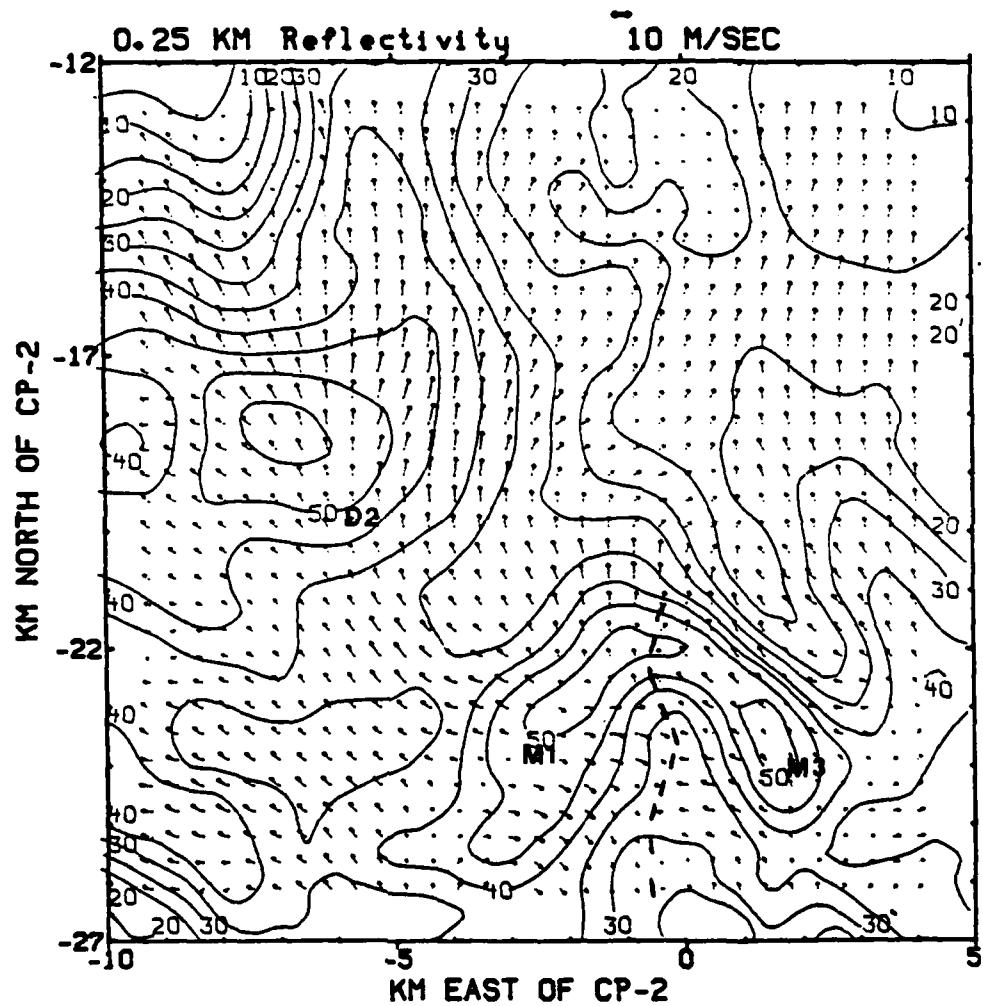


Fig 4.12 Plan view of the horizontal wind field and reflectivity field for 1847 MDT at 0.25 km.

gust front in the vicinity of (0, -24) is very apparent from the wind flow pattern based on the convergence of the winds that essentially defines the front.

Figure 4.13 shows the vertical velocity at 0.25 km for the 1847 MDT period. M1 is shown to be an area of strong downward vertical motion. It is, however, hard to distinguish the newer microburst, M3, based on the vertical motion field since M3's vertical velocity at 0.25 km is weaker than M1's. There is evidence from the divergent wind flow pattern in Figure 4.12. at (2, -24.5) that the area has become a microburst. From 1845 to 1847, the area grew rapidly, and it should now be considered a microburst based on the evidence of the divergent wind flow at 0.25 km. The downdraft, D2, shows rather strong vertical motion at this level, but the low-level wind field at 0.25 km for 1847 remains unaffected by the downdraft. At 1847, D2 can not yet be considered a microburst, but it seems to be growing and its flow may possibly break through to the surface by the next radar scan at 1850 MDT.

The perturbation pressure pattern for the 1847 case is shown in Figure 4.14. The convergence at the surface causes a bubble-high where M1's downdraft reaches the surface. There is a strong meso-high for the downdraft, D2, at the 0.25 km level. D2 shows an increase in perturbation pressure at the surface. This increase in perturbation

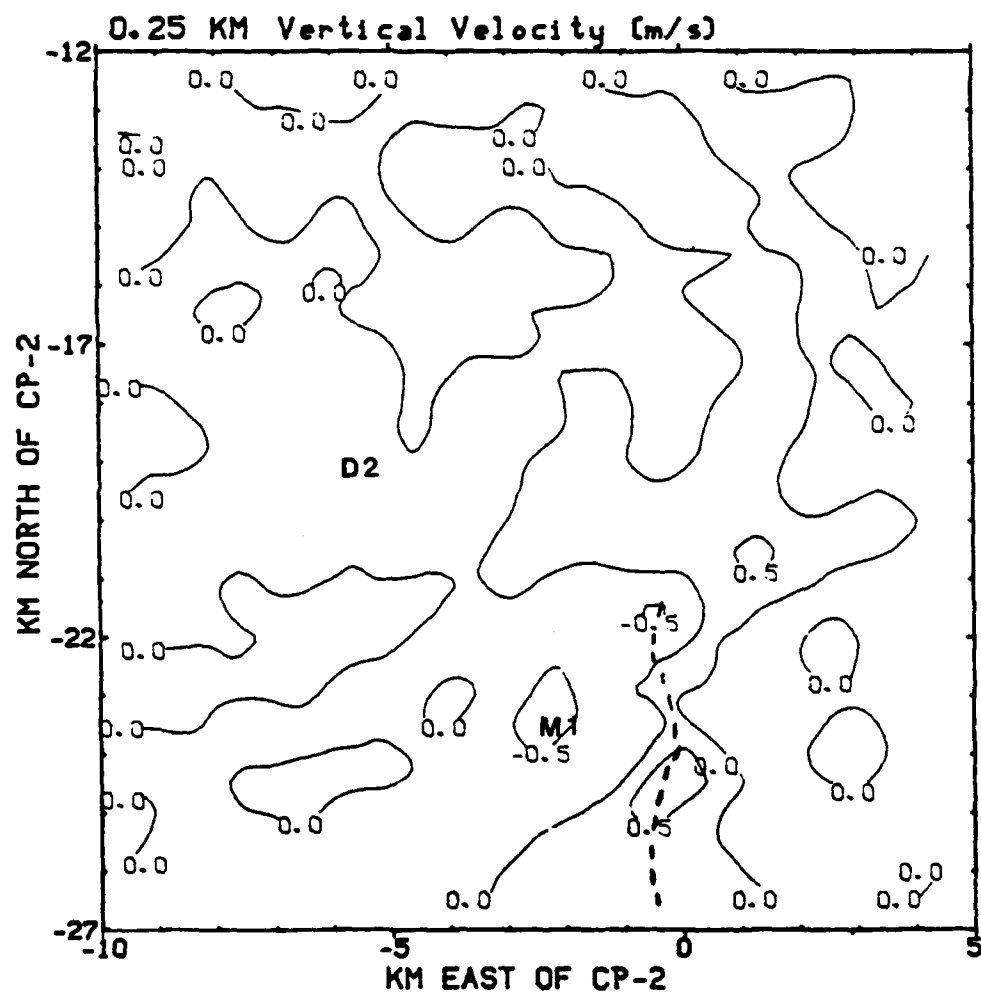


Fig 4.13 Same as Fig 4.12, except for vertical velocity.

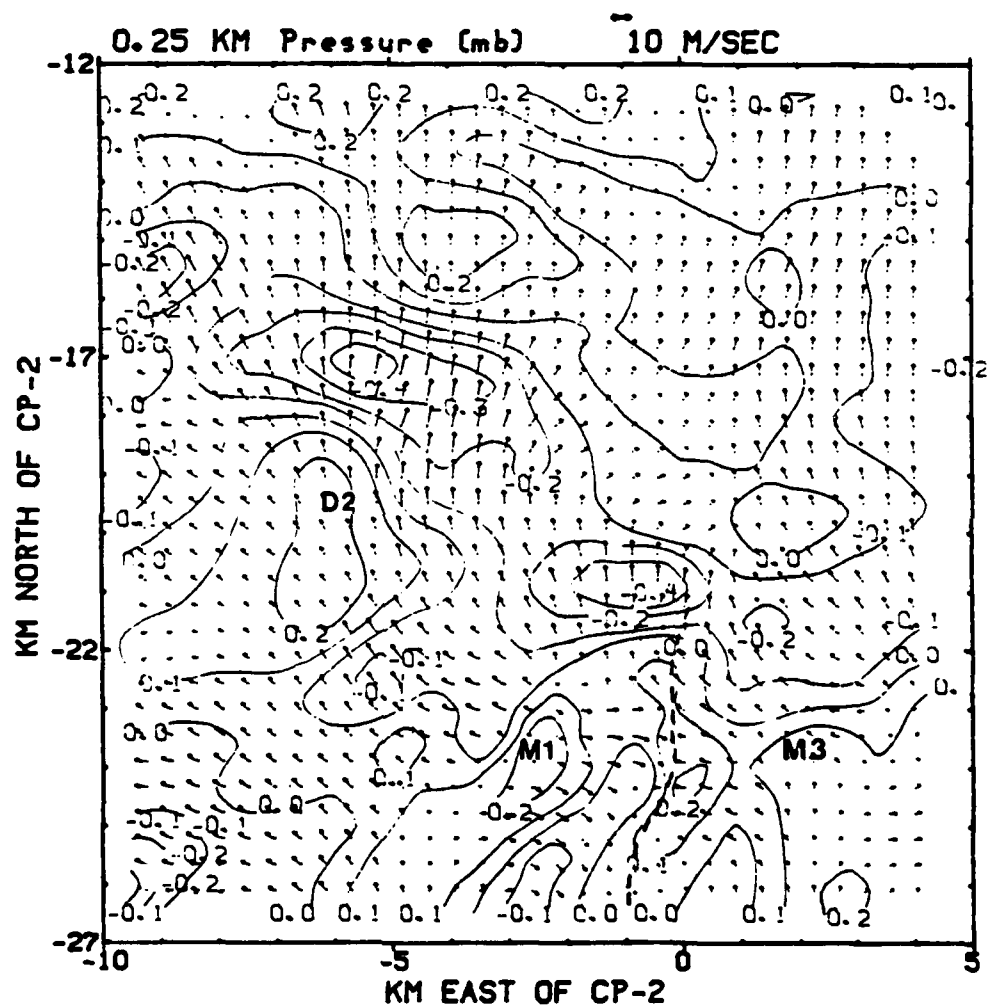


Fig 4.14 Same as Fig 4.13, except for pressure  $P'_{vd}$ .



tion pressure at the surface is due to D2's downdraft as it approaches the surface. The perturbation pressure felt at the surface directly under the path of the downdraft above would certainly increase due to the weight of the converging air mass above. Thus, the perturbation pressure field can serve as an indicator of changing flow above. The perturbation pressure field for this same time period with tendency included would show more detail in the pressure field, and will be discussed at a later time.

The temperature pattern for the 1847 case at 0.25 km is shown in Figure 4.15. Note that the core of M1 shows a cold temperature anomaly at the surface as the cooled air from the downdraft converges at the surface. The gust front is well defined based on the cold anomaly where the converging outflow from the microburst is contrasted with the environmental air in the region between M1 and M3. Outflow from a microburst is generally cold in comparison to the surrounding air due to evaporative cooling within the downdraft as moist air is mixed with drier environmental air above 1 km.

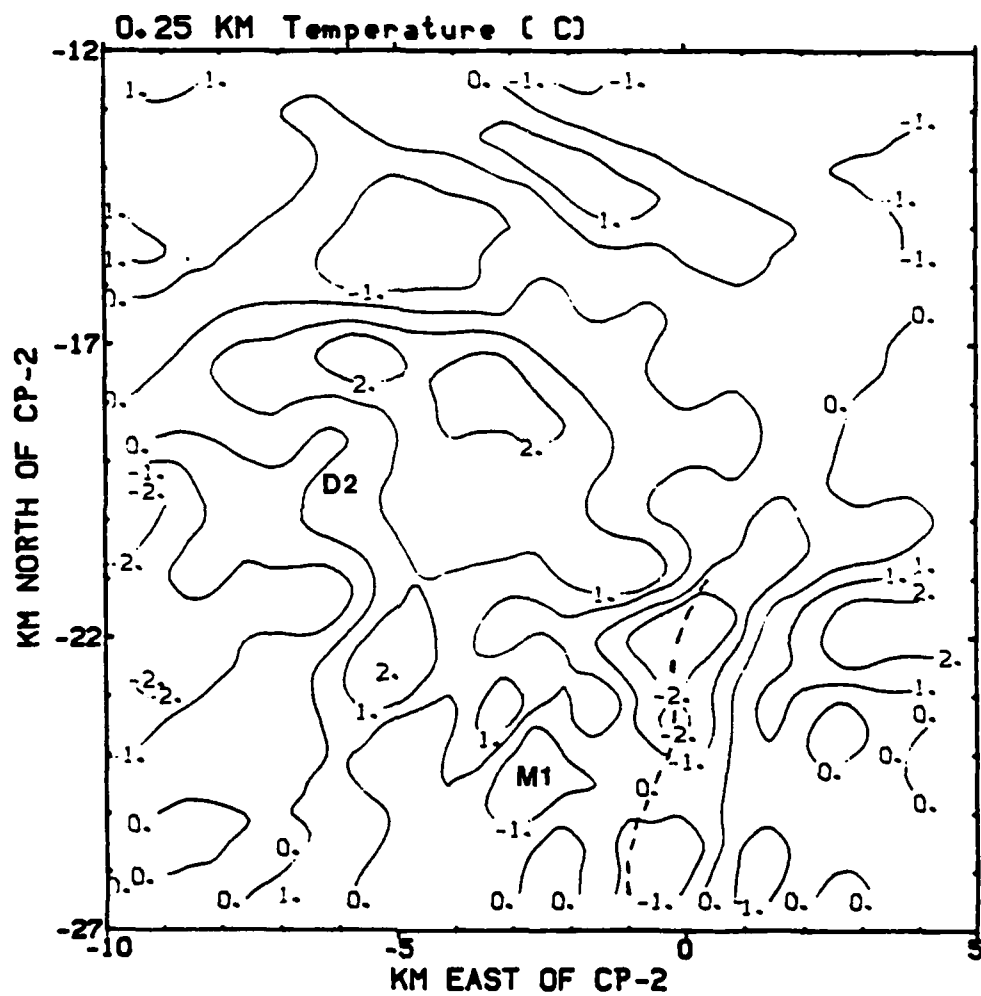


Fig 4.15 Same as Fig 4.12, except for temperature  $T'_{vd}$ .

The reflectivity pattern for 0.5 km is shown in Figure 4.16. M1 and M3 have developed a strong reflectivity region of 50 dBz that presents a bow-echo effect. At 1845, this feature was not discernable, and the 50 dBz contour that identified M3 was barely distinguishable. The cyclonic circulation at the south end of the gust front is also apparent, and its radius of rotation has grown from the 0.25 km level.

The 0.5 km vertical velocity field is shown in Figure 4.17. Strong vertical velocity is displayed for M1, while M3 and D2 are showing signs of increased vertical motion that was not apparent at the 0.25 km level.

Looking at the reflectivity and wind flow field for 0.75 km, as shown in Figure 4.18, there is little interaction between the environmental flow and the shafts of downward vertical motion associated with M1, M3 and D2. The predominant flow is from the southeast, and there is no evidence of entrainment of the environmental flow into the downdrafts, as evidenced by the uniformity of the environmental flow as it seems to ignore the downdraft core.

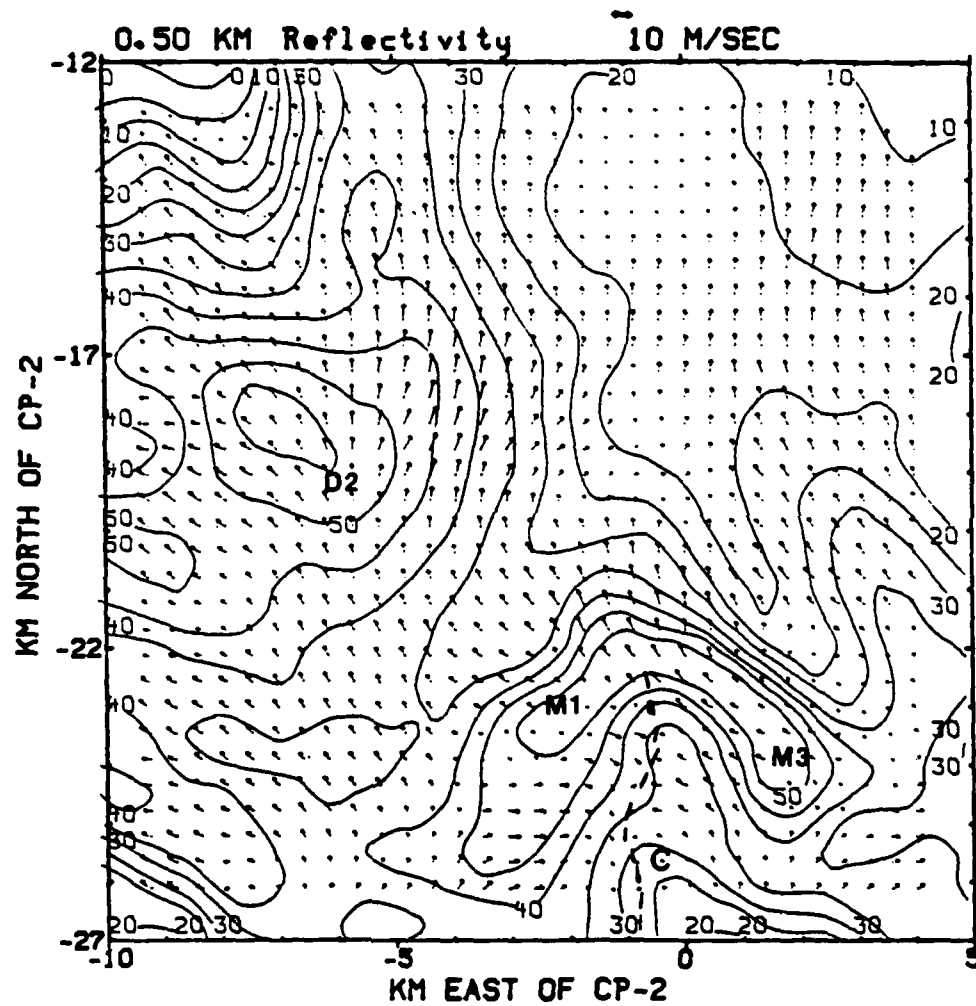


Fig 4.16 Plan view of the horizontal wind field and reflectivity field for 1847 MDT at 0.5 km.

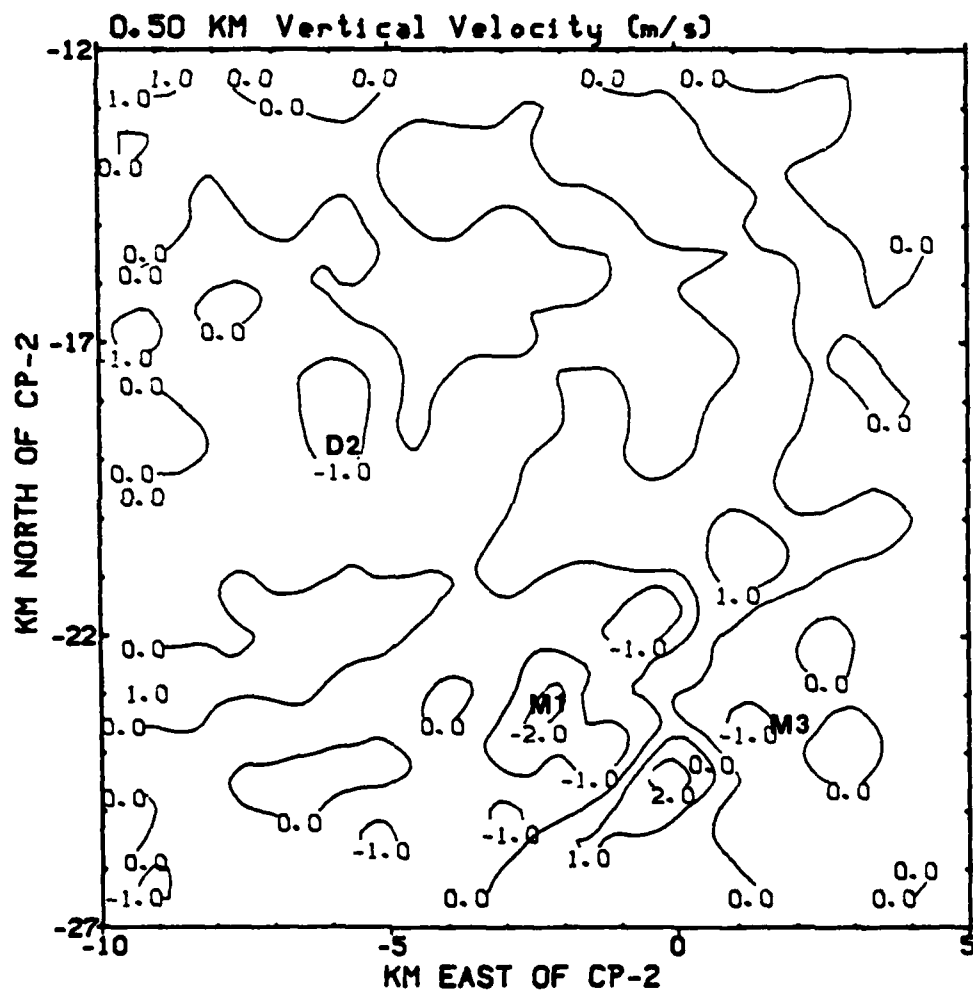


Fig 4.17 Same as Fig 4.16, except for vertical velocity.

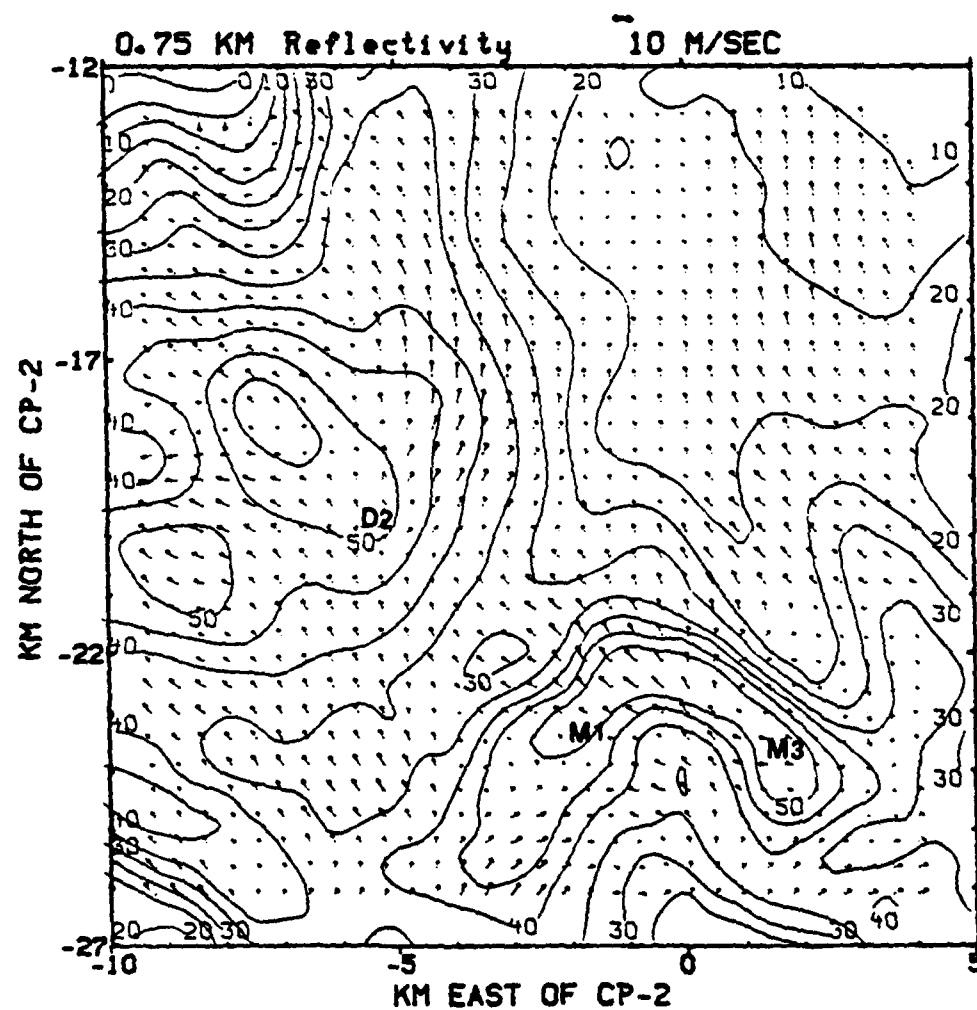


Fig 4.18 Plan view of the horizontal wind field and reflectivity field for 1847 MDT at 0.75 km.

The vertical velocity field for the 0.75 km level is shown in Figure 4.19. Strong vertical velocities for both M1 and D2 ( $-2.0$  m/sec) are shown, with M3 showing a somewhat weaker value ( $-1.0$  m/sec). The second microburst has grown since 1845, but it is not nearly as strong as D2 at this level. Note the area of strong upward vertical velocity in the area between M1 and M3 (0, -24). This upward vertical motion results from the outflows of M1 and M3 and their interaction with the mean flow at the gust front. This upward vertical flow can supply both M1 and M3 with warm, moist air, which helps sustain the microbursts. One of the mechanisms that sustains the downdraft is evaporative cooling of the downflow. M3 has displayed substantial growth since the first time period of 1845, and during the next period under consideration it should continue to grow.

The 1 km reflectivity with wind flow field superimposed is shown in Figure 4.20. As was the case at 1845, environmental air from the south is beginning to be funneled to the downwardly-moving shaft of M1, as evidenced by the wind flow pattern. This is not the case with neither D2 nor M3. Since M1's downdraft is stronger, it seems the attraction of a downdraft to the dry environmental air is related to the strength of the downflow within the microburst. The intensity of the downdraft is attributable to the amount of dry environmental air entrained in

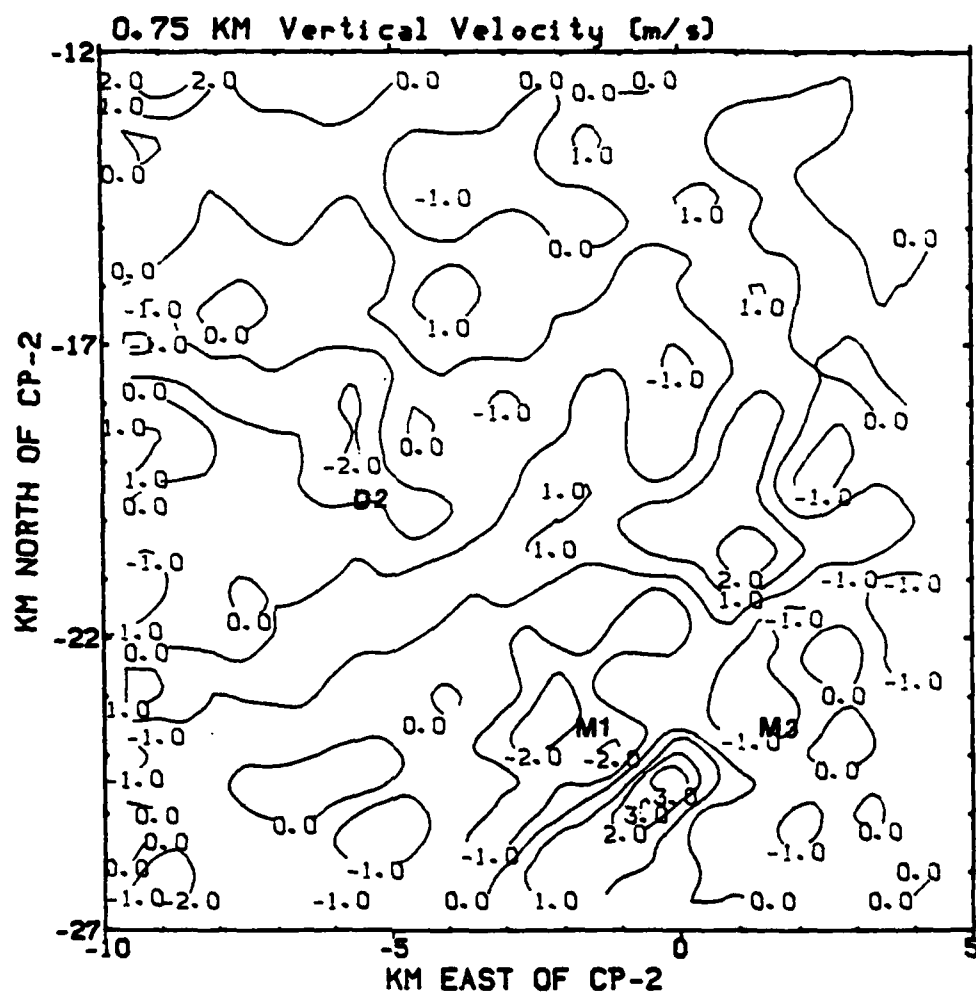


Fig 4.19 Same as Fig 4.18, except for vertical velocity.



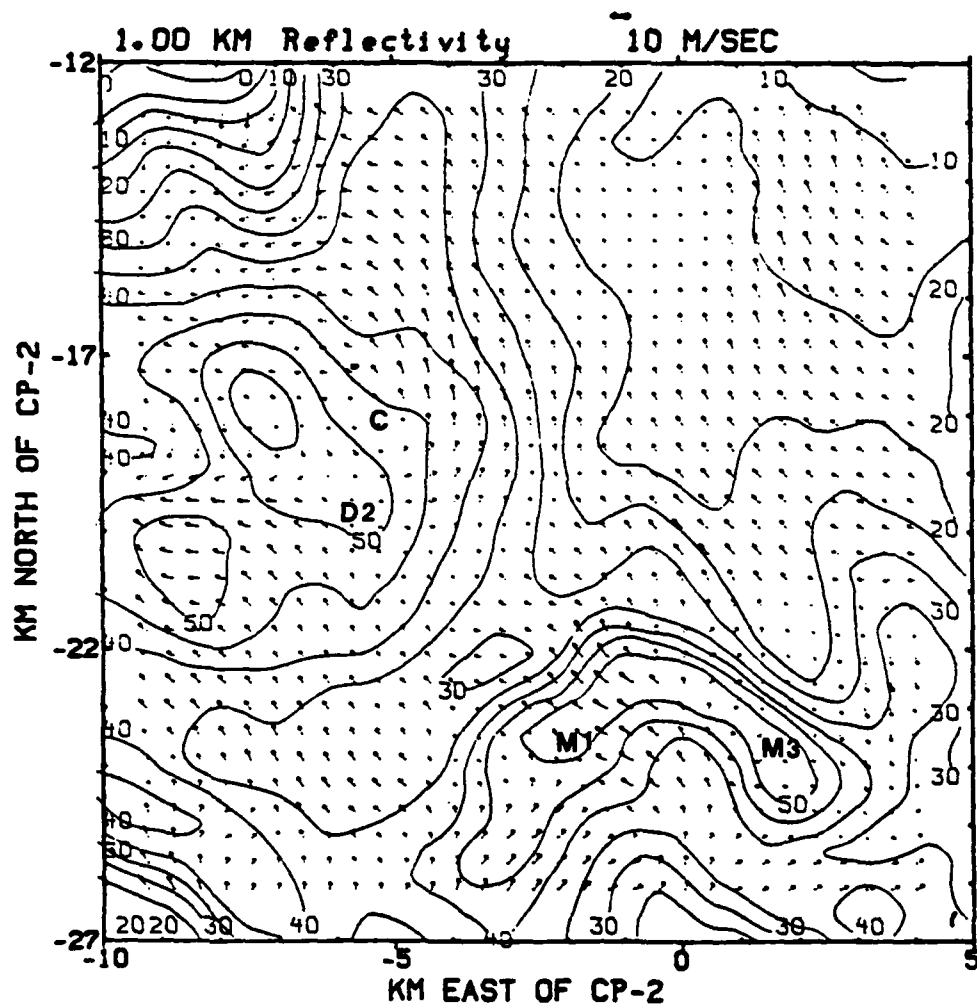


Fig 4.20 Plan view of the horizontal wind field and reflectivity field for 1847 MDT at 1 km.

the upper levels. Note that at (-5, -20), a cyclonic circulation pattern is plainly visible north of D2, but this circulation is not helping to funnel the warm environmental flow into the downdraft core. If this were the case, perhaps the downflow of D2 would extend to the surface and D2 would then be a microburst.

#### 4.1.3 1850 Plan View Plots

The 1850 time period reflectivity pattern is shown in Figure 4.21. By this time, a vigorous stream of downward-moving air from the second microburst, M3, has reached the surface. M3 is now definitely considered a microburst, since the diverging outflow of M3 near the surface is clearly visible. The microburst, as expected, is coincident with the 50 dBz contour. The gust front continues to be very well defined in the area between M1 and M3, as would be expected in an area between the two converging outflow winds of the microbursts. The outflow from M3 has coincided with the appearance of a second gust front to the north of M3.

D2 continues to be in a strong reflectivity area of 55 dBz; however, D2 still does not evidence a strong divergent outflow at the surface. Note the strong flow of air toward lower dBz values as precipitation cooled air from the outflow under-runs the warmer environmental air at the surface. Because of this cool air underflow, positive vertical motion along the gust front is expected, thereby increasing the intensity of both M1 and M3 by providing moist low-level air. The cool diverging outflow air thus enhances further inflow of warm air to both microbursts.

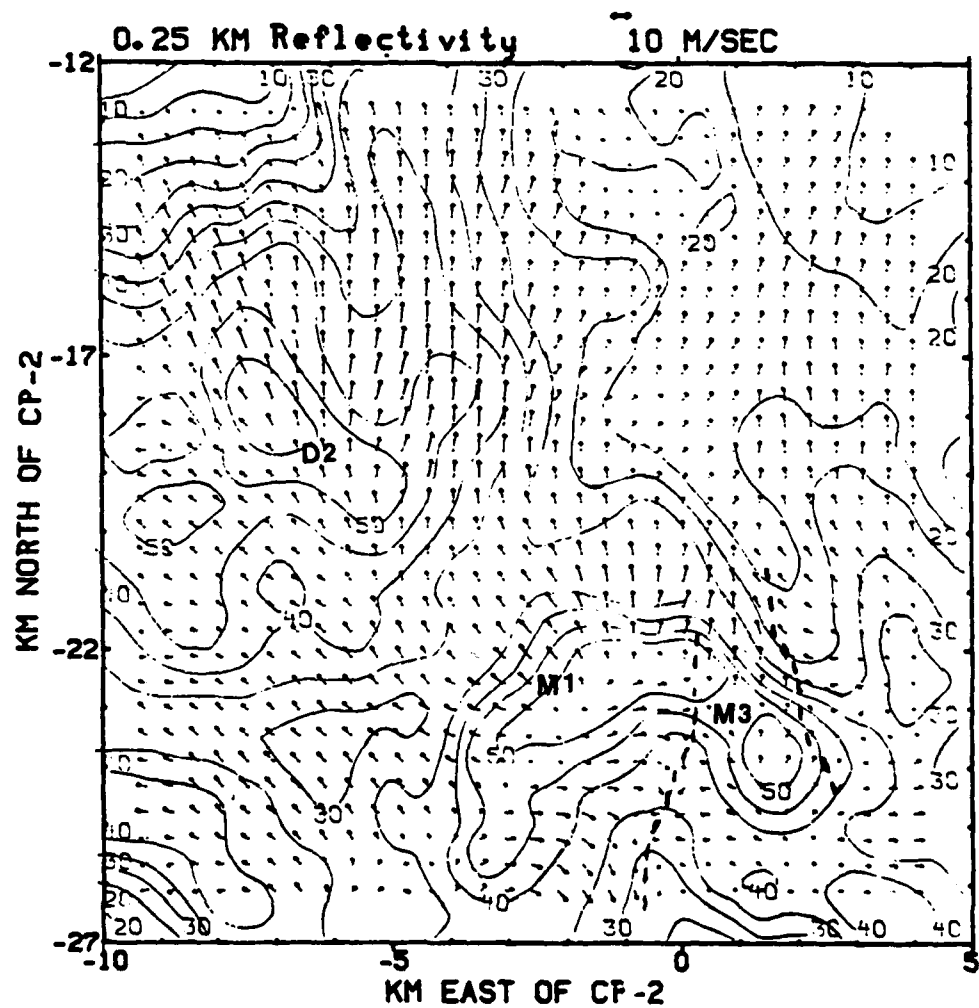
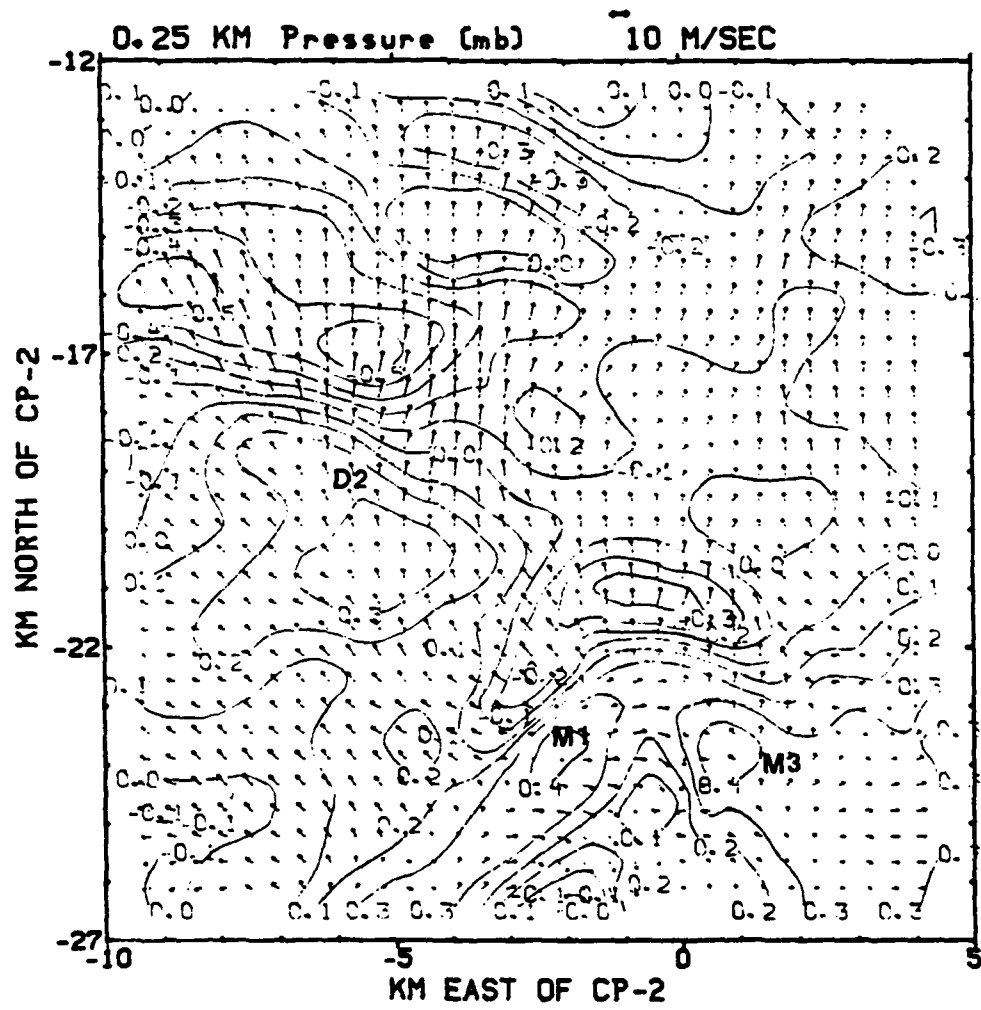


Fig 4.21 Plan view of the horizontal wind field and reflectivity field for 1850 MDT at 0.25 km.

The 1850 perturbation pressure plot at 0.25 km is shown in Figure 4.22. The highest values of perturbation pressure are located to the upwind side of the microbursts where the downward-moving air diverges horizontally at the surface, and the environmental air and outflow from the microbursts meet. It is interesting to notice the perturbation pressure gradient, since as the gust front spreads out, the highest values of pressure deficit are directly ahead of the gust front. There is a strong increase in pressure from 1847-1850 MDT along the first gust front between M1 and M3 as M3 increases in outflow intensity, and the outflow from M3 has increased the pressure rise along the front. This is to be expected along the front since pressure rises as more air converges at the frontal boundary.



4.22 Same as Fig 4.21, except for pressure  $P'_d$

The vertical velocity field for 0.5 km is shown in Figure 4.23. Note the strong updraft velocity in the area between M1 and M3 along the gust front (2 m/s). The surface outflows of both microbursts increased the upward motion at the front to enhance the amount of warm environmental air being uplifted to feed the microbursts via precipitation loading. The interaction of M1 and M3 will thus cause the intensification of both microbursts. Looking at the vertical velocity field at 0.5 km, M1 is still much stronger than M3 or D2.

The perturbation pressure pattern for 0.5 km is shown in Figure 4.24. The pressure pattern reveals that the highest values of perturbation pressure are located on the upwind side (to the southeast) of the microburst, and the most negative pressure perturbation is located to the north of the microbursts just ahead of the outflow. Note the strong negative pressure perturbation (-0.3 mb at -5, -20) as D2 continues to grow. D2 has increased in intensity throughout the period, but it is still not considered a microburst based on the wind field at the lowest level.

The temperature pattern for 0.5 km is shown in Figure 4.25. M1 and M3 are clearly shown to be cold anomalies due to evaporative cooling in the downdraft as the upper level environmental air descends. The warm anomaly in the vicinity of the gust front is due to upward motion and adia-

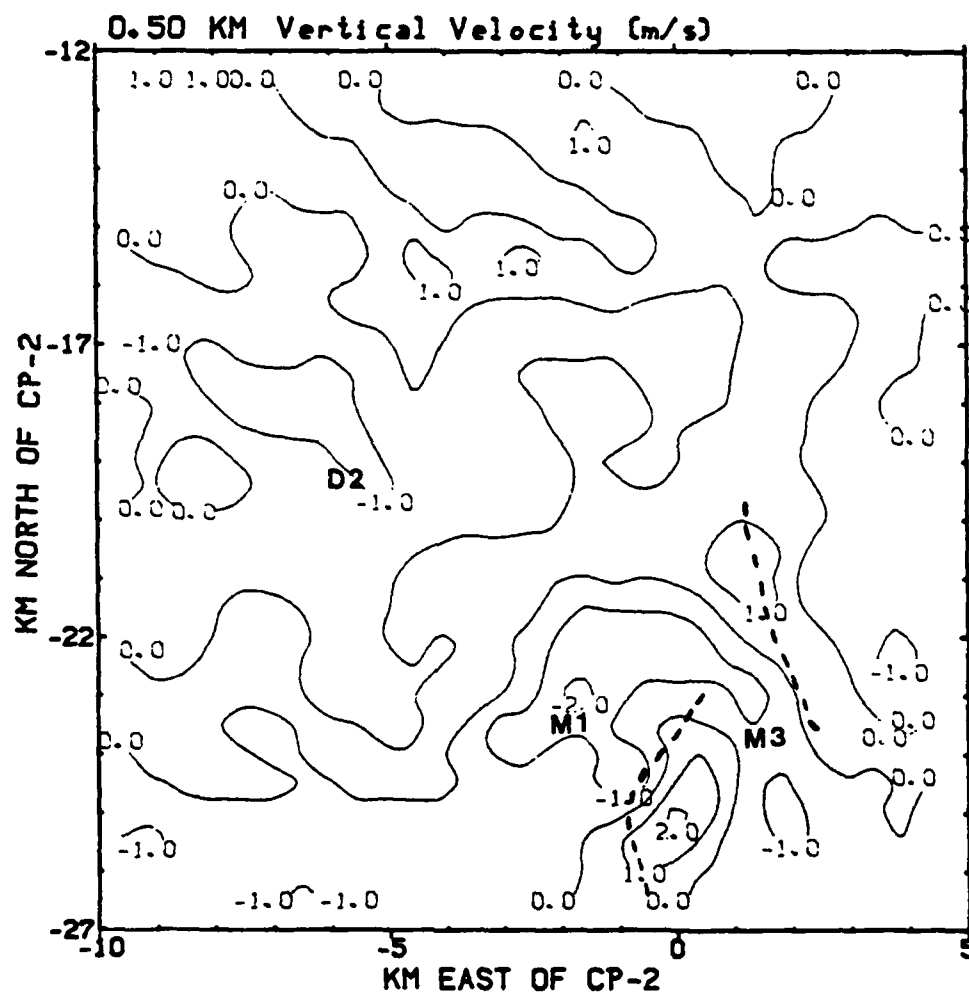


Fig 4.23 Plan view of the vertical velocity field for 1850 MDT at 0.5 km.





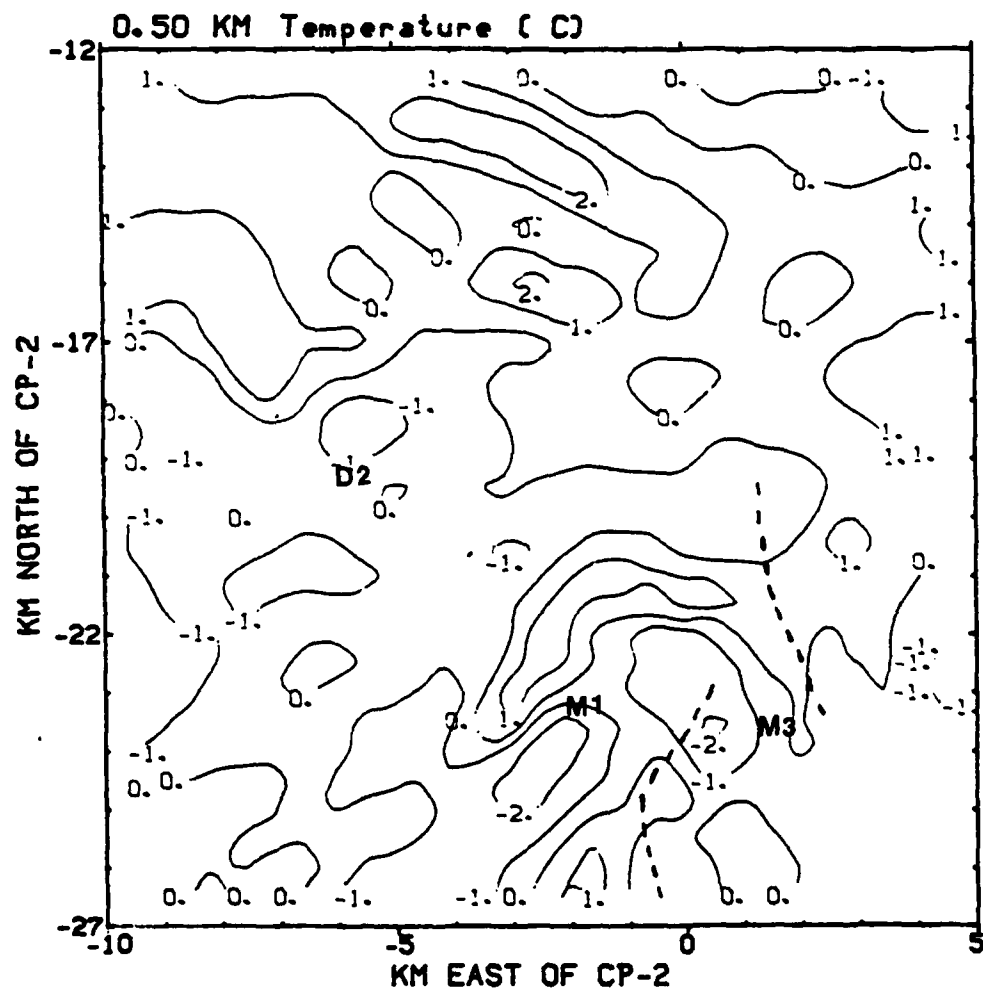


Fig 4.25 Same as Fig 4.23, except for temperature  $T'_{vd}$ .

batic expansion found in the updrafts, and warm environmental air being driven upward by convergence at the front. The same time period will be shown later with tendency considered, which should provide much more insight to the pressure and temperature fields, not only at this time period, but at all three.

The 0.75 km field of reflectivity is shown in Figure 4.26. Note the appearance of the gust front at 0.75 km, just to the south of M1. At the two previous time periods, the gust front was not manifested at the 0.75 km level. The intensification of M3 and the increased convergence along the gust front has increased the definition of the front. A misocyclone has appeared at (-3, -24.5), suggesting an intensification of the two microbursts has occurred.

The reflectivity field at 1.0 km is shown in Figure 4.27. The misocyclone near M1 (-3.5, -23.5) is well defined. A cyclonic circulation has appeared just to the north of D2 (-6, -18.5). The second microburst, M3, has not yet displayed a misocyclone. Coover (1988) believes that a misocyclone is not essential to the generation of the microburst. A misocyclone has a role in maintaining the storm by entraining environmental air into the downdraft; however, the misocyclone does not play a key role in the *generation* of the microburst. Note that M3 does not

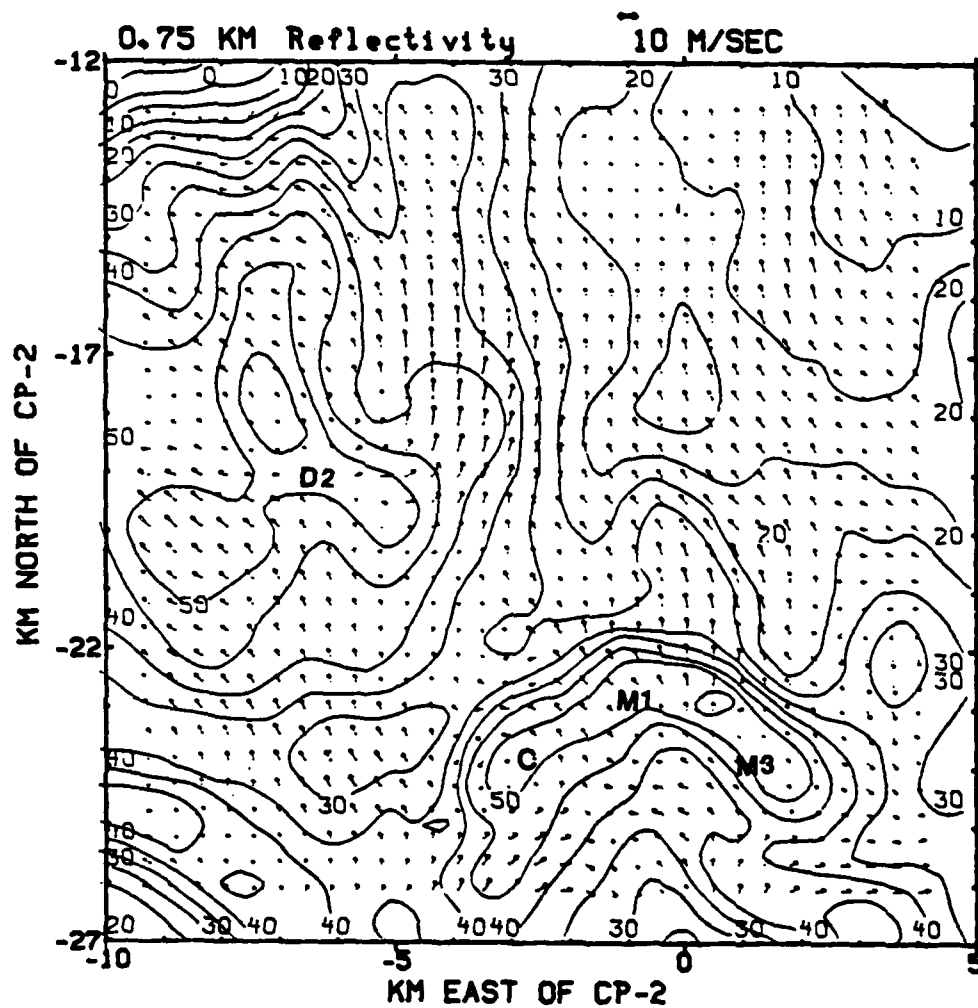


Fig 4.26 Plan view of the horizontal wind field and reflectivity field for 1850 MDT at 0.75 km.

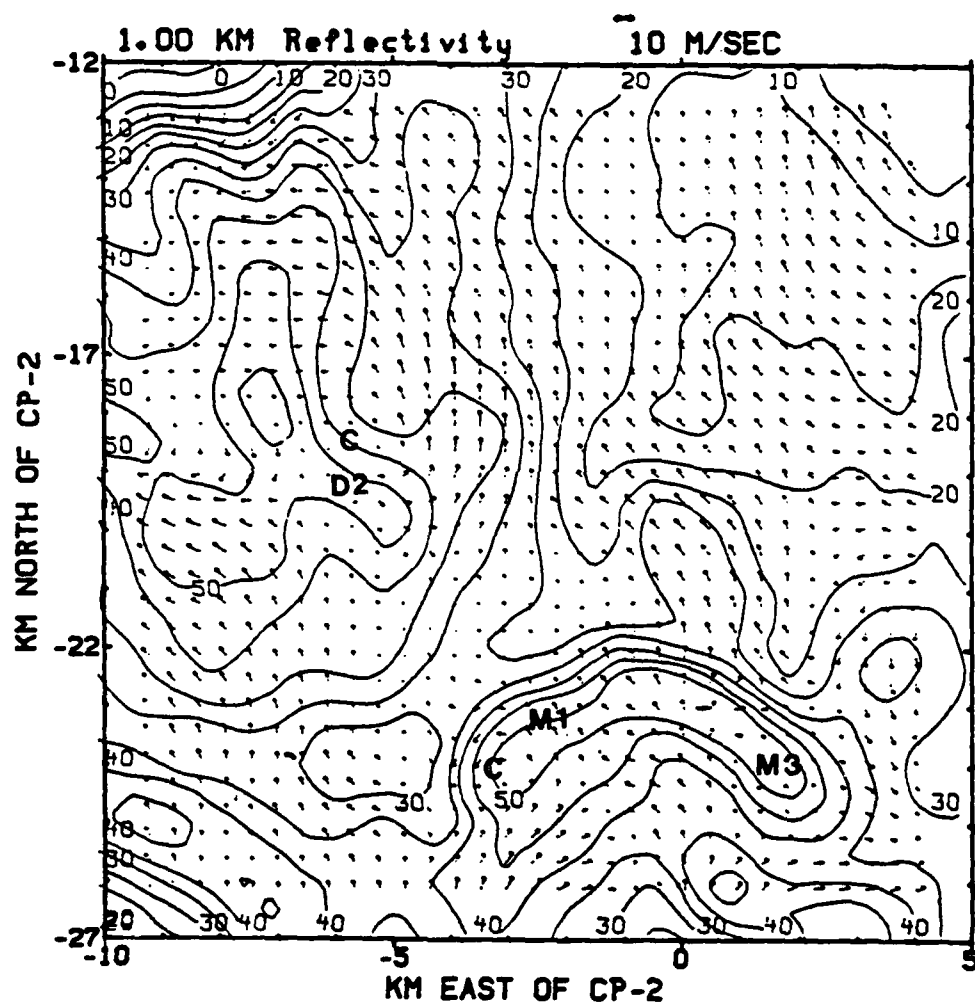


Fig 4.27 Plan view of the horizontal wind field and reflectivity field for 1850 MDT at 1 km.

manifest a misocyclone, while M1 and D2 do. The misocyclone is simply a factor in the maintenance of the storm by providing a mechanism for funneling dry, high-momentum air into the downdraft.

The reflectivity at 1.25 km is displayed in Figure 4.28. Note the well-defined misocyclone at (-3.5, -24). and the misocyclone near D2 (-5, -19). There is still no manifestation of an upper-level cyclonic flow near M3. Over a span of several minutes, M3 certainly would develop such a circulation as M1 and D2 have.

The pressure perturbation pattern is shown in Figure 4.29. A very large drop in perturbation pressure and an extensive low-pressure region is located near D2. This suggests that D2 is developing rapidly and will be a microburst in a matter of minutes, especially with the flow able to funnel dry air into the downdraft.

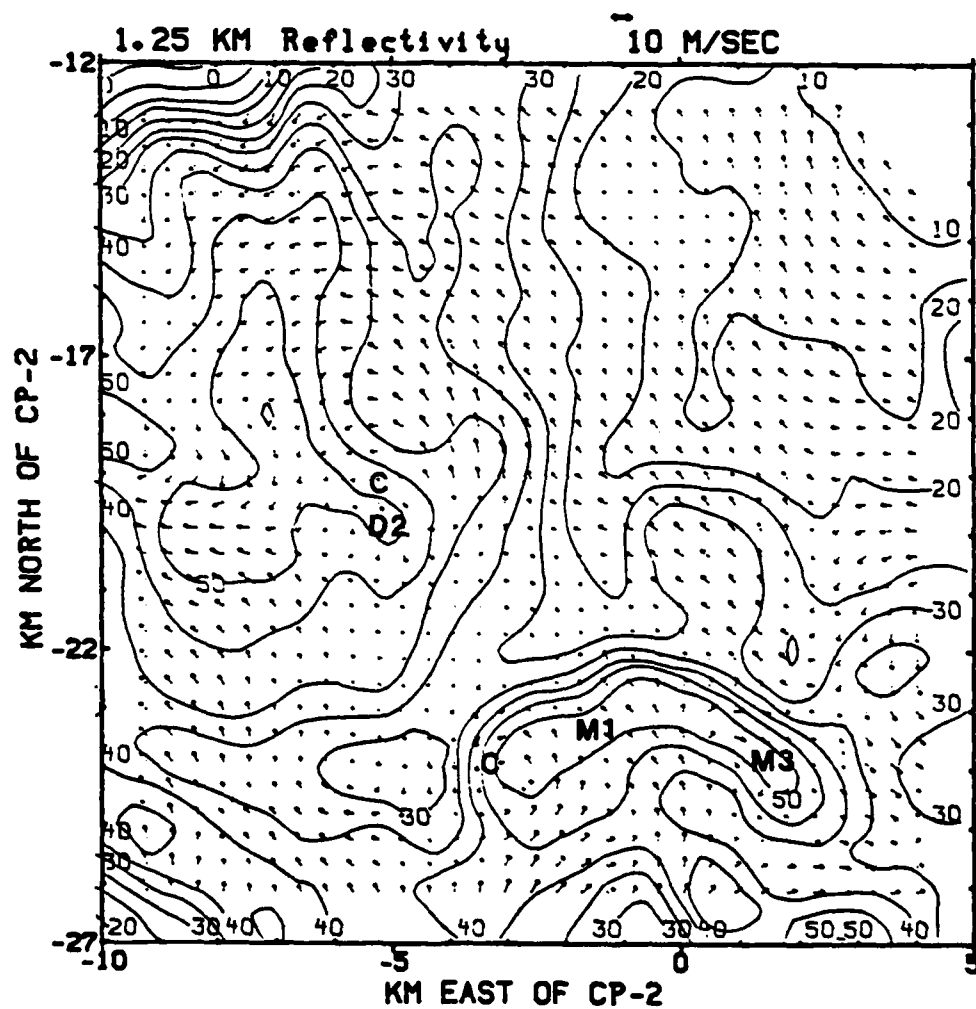


Fig 4.28 Plan view of the horizontal wind field and reflectivity field for 1850 MDT at 1.25 km.

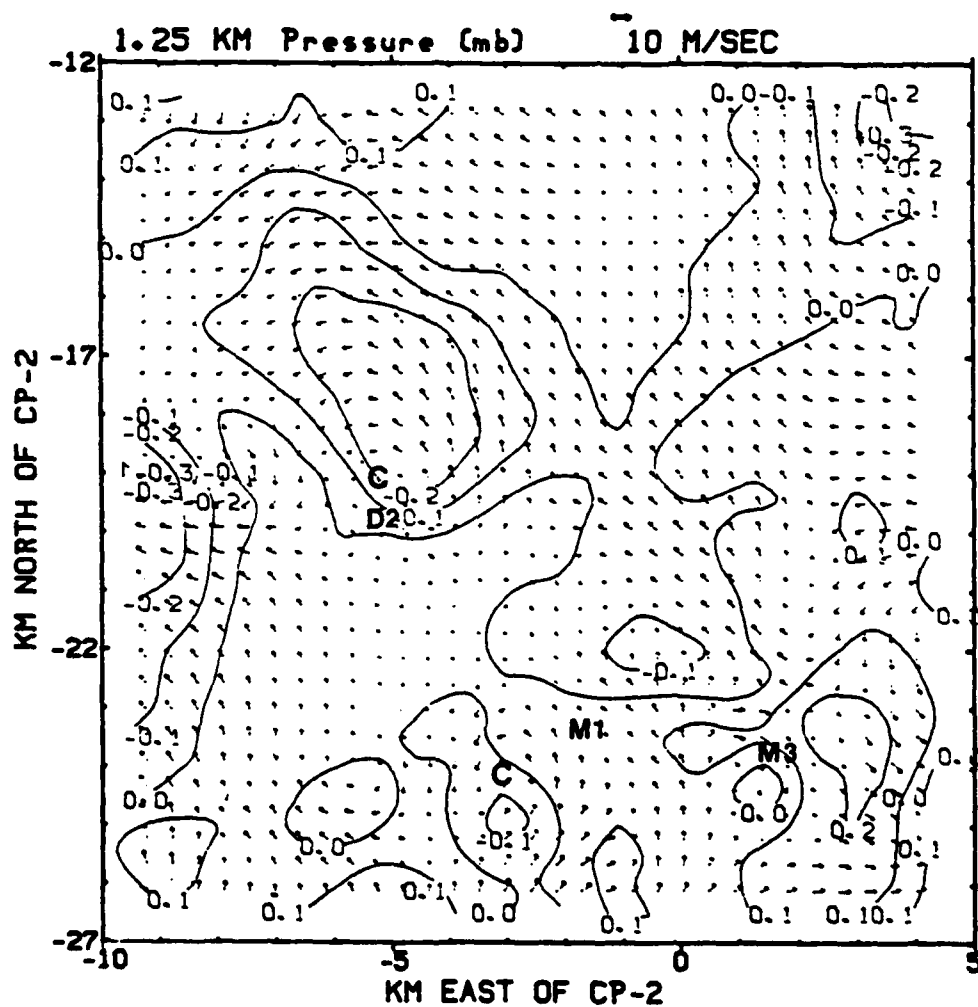


Fig 4.29 Same as Fig 4.28, except for pressure  $P'_d$ .



#### 4.2 Cross-Section Plots (tendency not considered)

Two cross-sections of the domain will be used, as shown in Figure 4.30. The first cross-section slice is oriented from northwest to southeast (NW-SE), as shown by line A-B. The second slice is from west to east (E-W), as shown by line C-D. Both cross-sections extend from the surface through a height of 1.25 km, so the five levels plotted in plan view will be represented in cross-section. For the plots in this section, the local time tendency terms are omitted from the momentum equations used to derive the perturbation pressure and temperature fields.

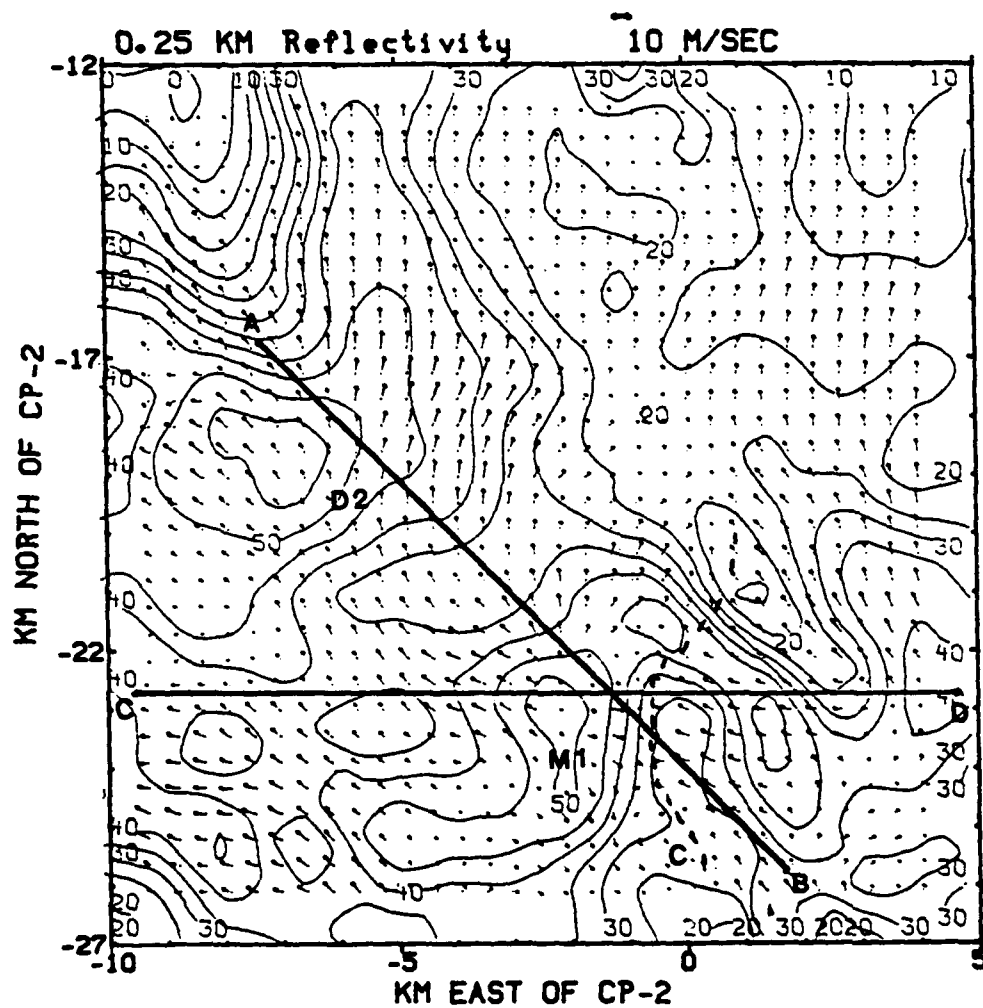


Fig 4.30 Plan view of the horizontal wind field and reflectivity field for 1845 MDT at 0.25 km. The axes of the NW-SE and E-W cross-sections are shown by lines A-B and C-D.

#### 4.2.1 (NW-SE) Cross-Section Plots

The northwest to southeast oriented cross-sections at all three time periods will be discussed in this section. The east to west cross-sections will be addressed in Section 4.2.2.

##### 4.2.1.a (NW-SE) Cross-Section at 1845

The 1845 wind flow and reflectivity, shown in Figure 4.31, depicts the mean flow from the southeast to the northwest. Between  $x = -2$  to 0, a circulation develops just to the left of the gust front. This flow results from interaction of microburst outflow and environmental inflow. To the left of M1, air descends and the secondary circulation over the gust front accentuating downward flow near M1. Convergence along the gust front is also enhanced by return flow around this secondary circulation.

To the right of M1, the gust front is clearly defined by the convergence of microburst and the environmental flows. There is evidence of negative vertical velocity of D2 ( $x = -5.5$  to 7) in the upper levels. This downward vertical motion has not penetrated to the surface, as clearly shown by the wind profile.

The vertical velocity field for 1845 is shown in Figure 4.32. The positive vertical velocity between  $x = -1$  to

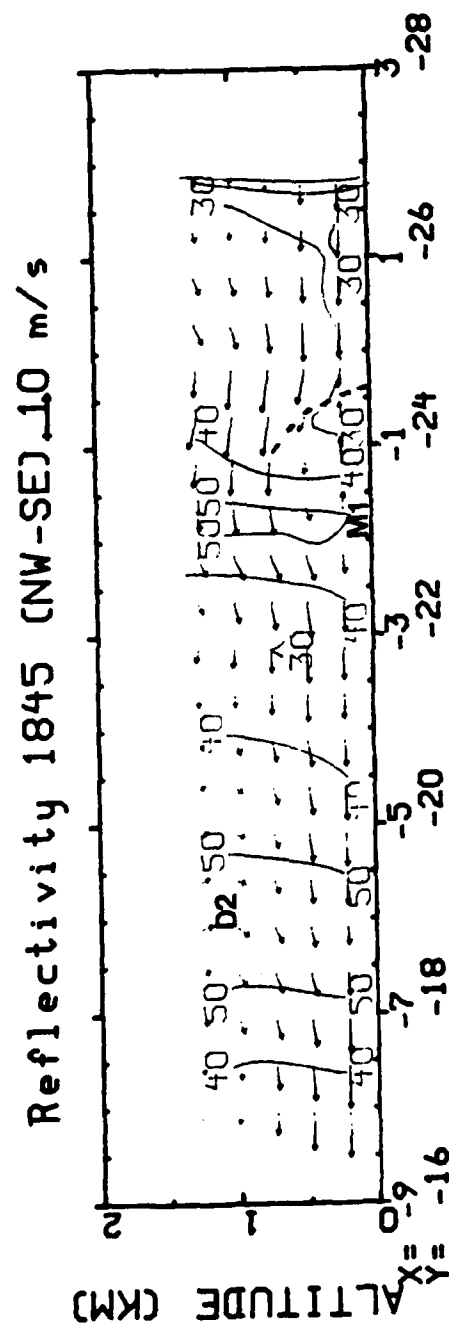


**Fig 4.31 NW-SE cross-section of the reflectivity field for 1845 MDT.**

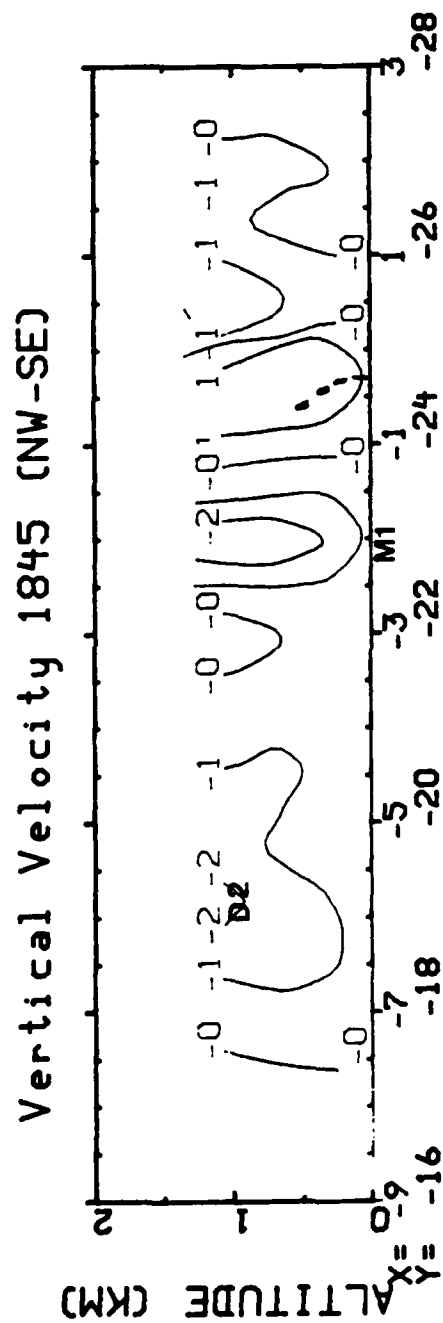


Fig 4.32 NW-SE cross-section of the vertical velocity field for 1845 MDT.

0 defines the location of the gust front. M1 is denoted by the maximum vertical velocity reaching to the surface ( $x = -2$ ). D2 is shown to have negative vertical velocity in the upper levels, but not extending to the surface ( $x = -6$ ). The negative vertical velocity at  $x = 0.5$  shows the beginning of M3 in the upper levels; however, the east-west cross-section is better suited to study the development of M3.

The 1845 pressure plot for the NW-SE cross-section is shown in Figure 4.33. The surface meso-high at  $x = -2$  shows where M1's descending air converges and surface outflow begins. Convergence at the gust front ( $x = 0$ ) shows the positive pressure perturbation as air converges and forms the frontal boundary. D2 is also showing a positive pressure perturbation near the surface ( $x = -6$ ) as the descending air at upper levels is beginning to be felt near the surface.

The 1845 NW-SE temperature plot is shown in Figure 4.34. Air from the microburst's outflow forms a cool pocket at the gust front boundary ( $x = 0$  to  $-1$ ) as the outflow's cool temperature is contrasted with the warm environmental flow. The temperature anomaly at  $x = -2$  shows the downwardly-moving cool air from the microburst as it reaches the surface.

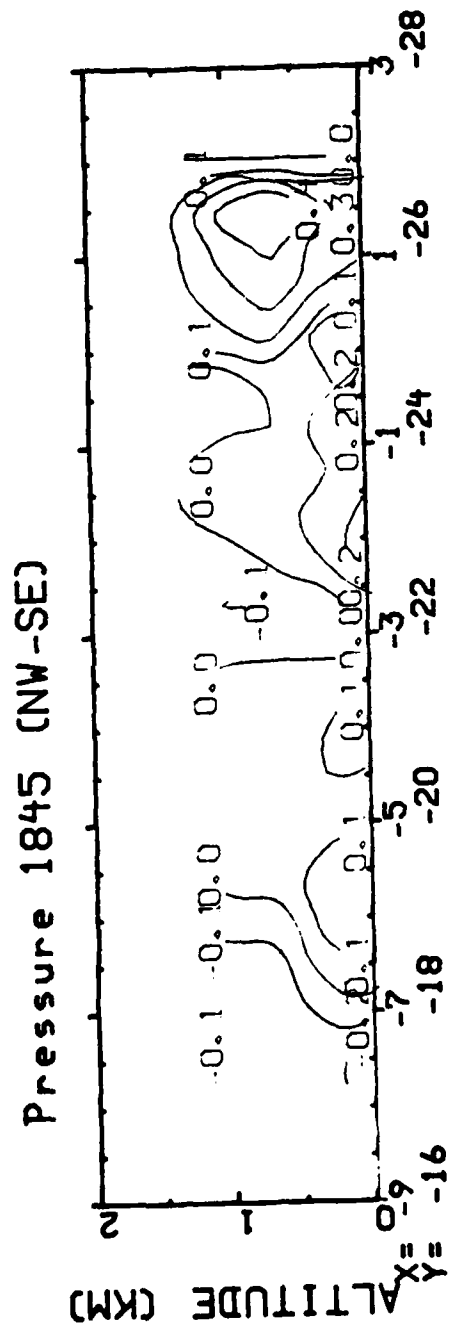


Fig 4.33 Same as Fig 4.32, except for pressure  $P'_d$ .

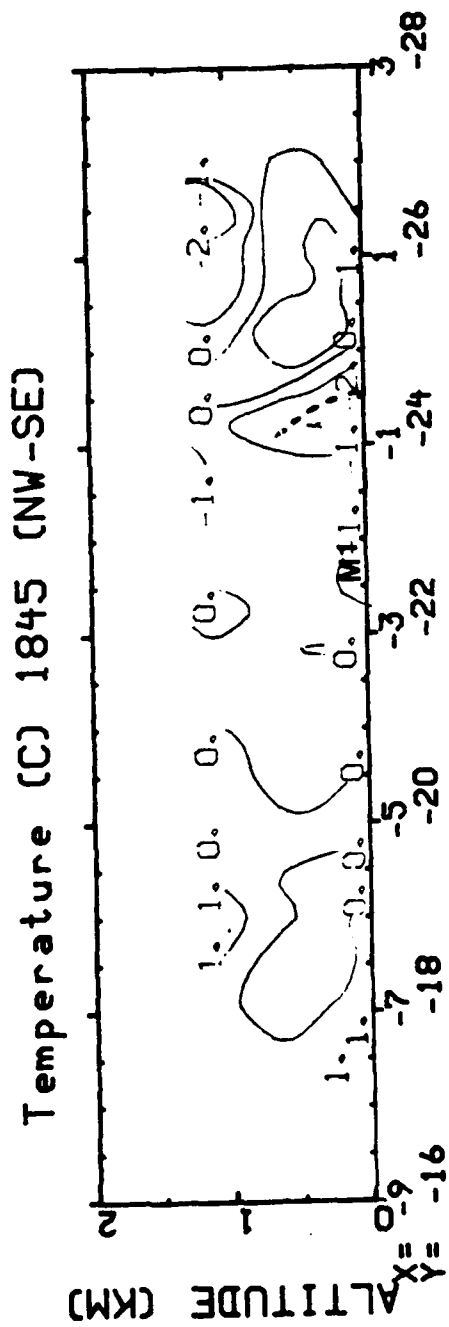


Fig 4.34 Same as Fig 4.32, except for temperature  $T'_{vd}$ .



#### 4.2.1.b (NW-SE) Cross-Section at 1847

The reflectivity cross-section plot for 1847 is shown in Figure 4.35. The gust front near  $x = 0$  has intensified and the converging microburst and environmental flows are thrust into higher levels as upward vertical motion at the front is detailed by the wind flow profile. The reverse circulation to the left of the gust front is also stronger, resulting in increased convergence at the lowest level of the frontal boundary. D2 continues to grow as the wind field shows a descending downflow at the top three levels. D2 shows no effect on low-level flow as the environmental wind flow at the lowest level remains unaffected by the descending air from D2 above.

The vertical velocity field for 1847 is shown in Figure 4.36. Note the increased vertical velocity at the gust front in the vicinity of  $x = 0$ . The return circulation around the gust front has indeed enhanced convergence and resulted in an increase in upward vertical motion along the gust front. The maximum vertical velocity for M1 has decreased slightly since 1845. This suggests that M1 may be weakening as it competes with the developing M3 for moist air. D2 has intensified, but its effects still do not extend to the surface, as mean flow at the surface remains undisturbed by D2.

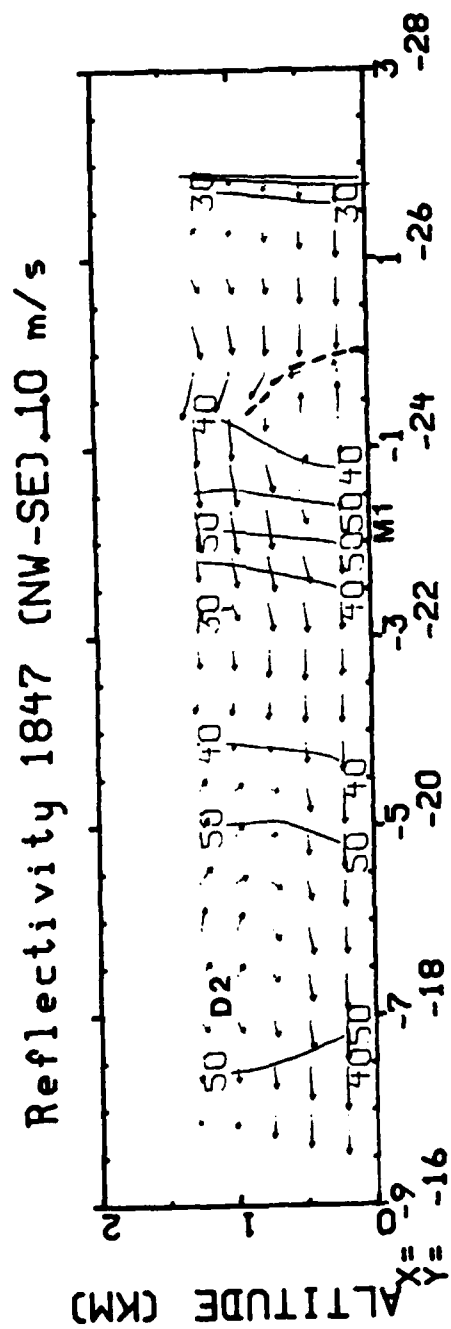


Fig 4.35 NW-SE cross-section of the reflectivity field for 1847 MDT.

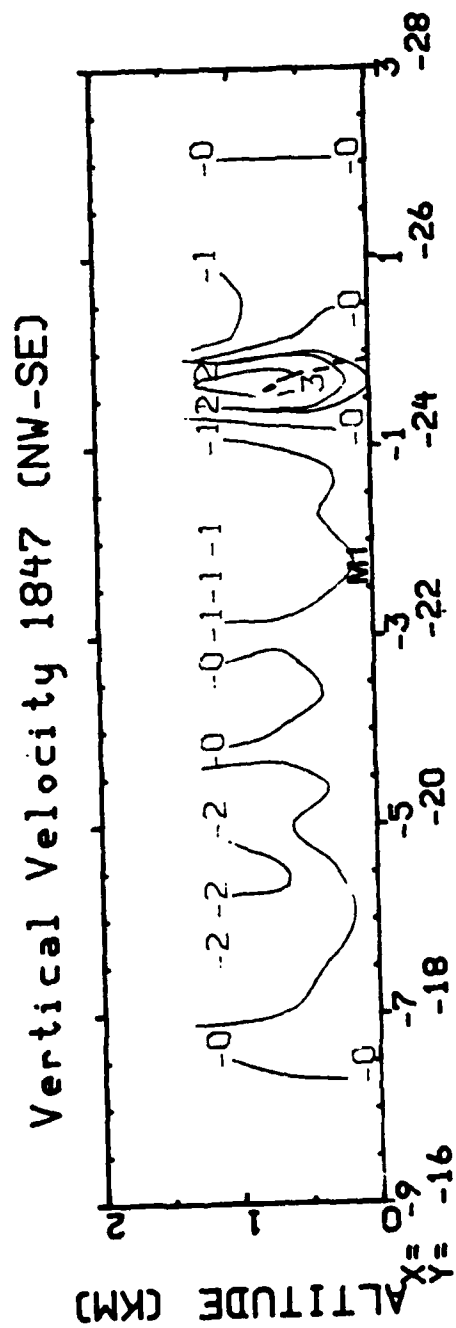


Fig 4.36 Same as Fig 4.35, except for vertical velocity.

4.2.1.c (NW-SE) Cross-Section at 1850

The NW-SE reflectivity pattern for 1850 is shown in Figure 4.37. The circulation pattern at the gust front remains robust, and convergence at the gust front is apparent from the wind flow field. The divergent outflow from M1 is also shown, but it is not as strong as it was during earlier stages of the study due to interaction with the outflow of M3 and environmental low-level winds. D2 has grown ( $x = -2$ ), but it still does not extend to the lowest level, and does not have the divergent outflow at the surface that defines a microburst. Based on this wind plot, D2 is not manifested at the surface, and throughout the period of this study from 1845 to 1850, it remains an enhanced downdraft and can not be considered a microburst.

The vertical velocity is shown in Figure 4.38. Again, strong vertical motion characterizes M1 extending from 1.25 km all the way to the surface. The positive vertical velocity at the gust front continues in the vicinity of  $x = 0$ . The downward vertical velocity to the left side of the gust front identifies the circulation on the left side of the front ( $x = -1$ ).

The perturbation pressure plot for 1850 is shown in Figure 4.39. The surface meso-high associated with M1 is shown at  $x = -1.7$ . High pressure associated with M1

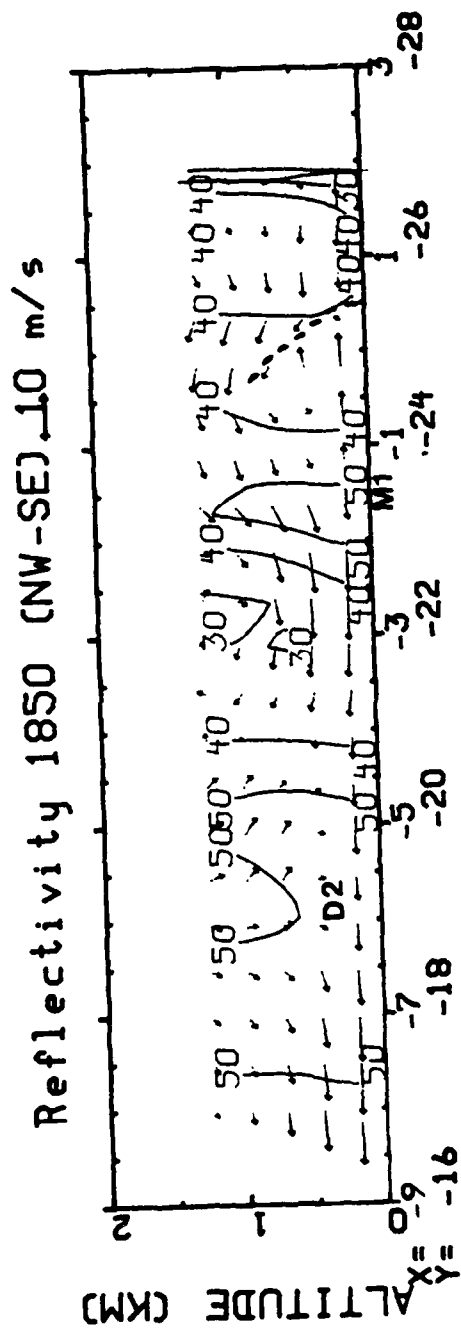


Fig 4.37 NW-SE cross-section of the reflectivity field for 1850 MDT.

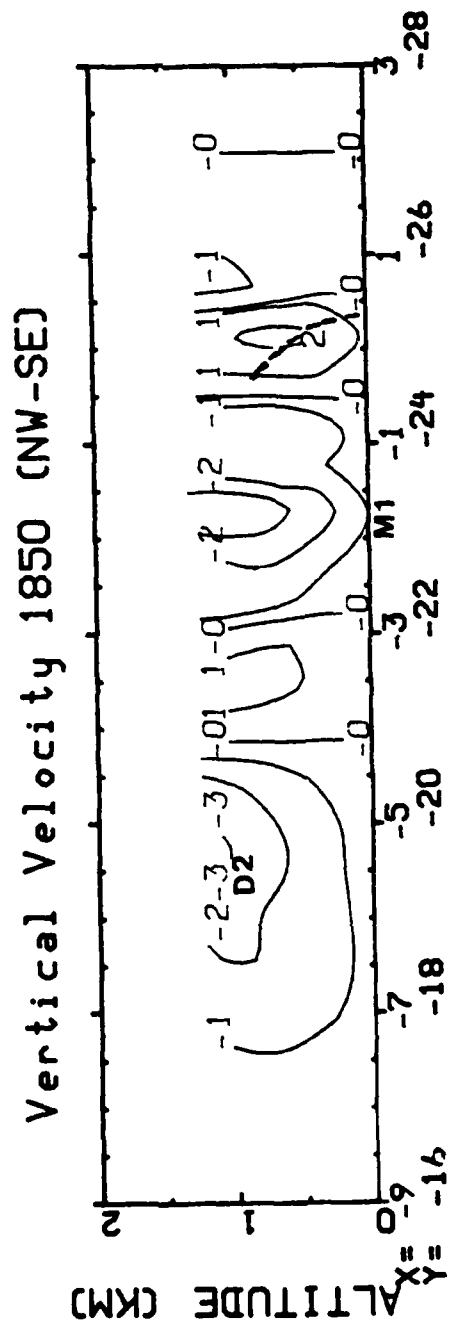


Fig 4.38 Same as Fig 4.37, except for vertical velocity.



extends only into the lower levels. In the vicinity of the gust front ( $x = 0$ ), there is a positive pressure perturbation as the winds converge at the front.

The temperature field for the NW-SE cross section at 1850 is shown in Figure 4.40. It is interesting to note the warm anomaly at  $x = 0$  where the return flow over the gust front converges at the lower levels of the front. The environmental flow is warmer than the microburst's outflow, so the warm anomaly is encountered when the air circulated around the gust front reaches the surface near  $x = -2$ . Normally, one would expect a cold anomaly due to the cool outflow from the downdraft of the microburst, but due to a strong return flow at the gust front, the warm anomaly is encountered instead.



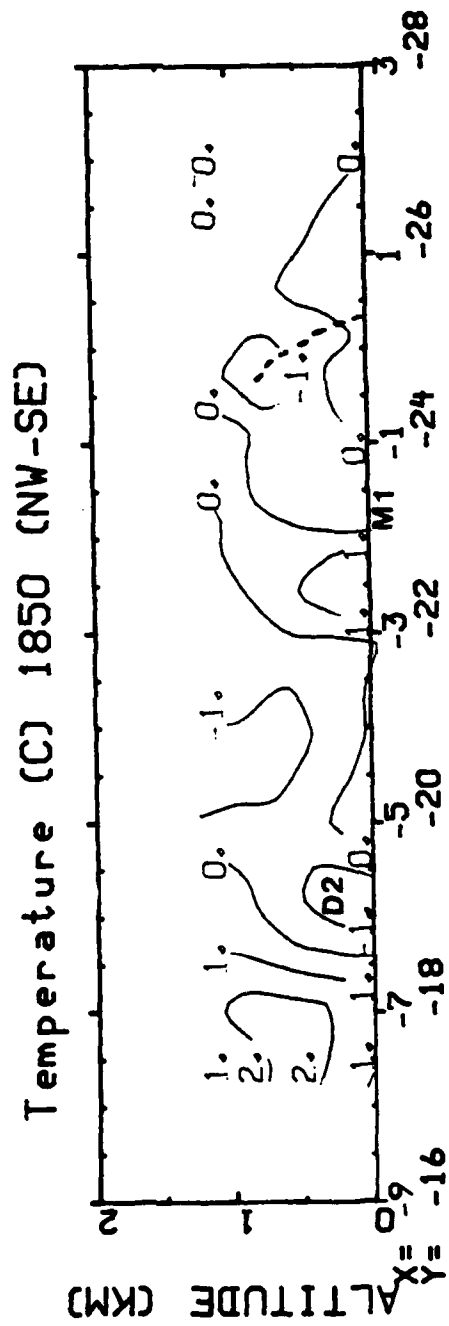


Fig 4.40 Same as Fig 4.37, except for temperature  $T'_{vd}$ .

#### 4.2.2 (E-W) Cross-Section Plots

Cross-sections for the east-west oriented slice of the area under study will be examined for all three time periods. Plots in this section do not include the local tendency terms in the momentum equations.

##### 4.2.2.a (E-W) Cross-Section at 1845

The east-west cross-section for the 1845 time period reflectivity field is shown in Figure 4.41. The strong downward vertical motion near  $x = -2$  identifies M1 as a microburst. Note the strong divergent winds as the downdraft from the microburst reaches the surface and spreads. The convergence at the gust front is apparent in the vicinity of  $x = 0$  to  $-1$ . It is interesting to note that gust front convergence extends only to the lowest level, and the directional shear at the frontal boundary between the first and second levels is obvious. The outflow from the microburst at the lowest levels is westerly oriented, while at the next level, environmental flow and has an easterly component; thus, there is a pronounced directional shear of the winds from the 0.25 km level to the 0.50 km level in the vicinity of the gust front.

As the environmental air above 0.75 km nears the downdraft of M1 in the vicinity of  $x = -1$ , it mixes with

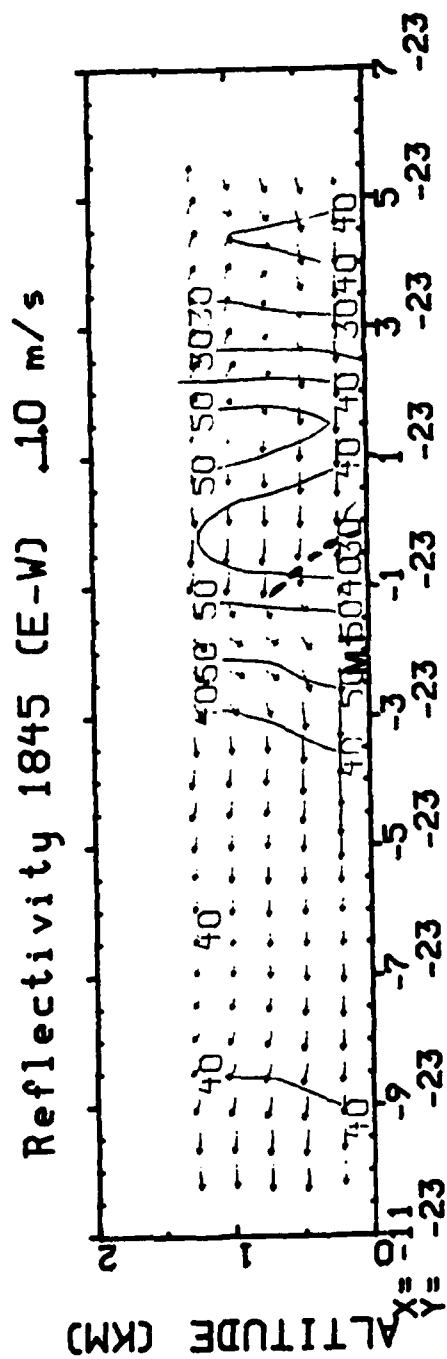


Fig 4.41 E-W cross-section of the reflectivity field for 1845 MDT.

the downdraft, just to the right of M1. The cool and dry environmental air comes into contact with the precipitation loaded air of the downdraft. Since the velocity of the downdraft is still relatively slow, the environmental air undergoes precipitation cooling due to interaction of the dry upper-level flow with the moist downdraft. If the speed of the downdraft were faster, the air could not allow such entrainment because the environmental air would not be joined into the downdraft. At  $x = 1.5$ , there is evidence of downflow, especially in the upper layers. Within the strong reflectivity region of 50 dBz, the downward motion of the upper layers is apparent. This is the region where M3 will develop, so the following two time periods should be interesting to study microburst development in this region.

The vertical velocity field for 1845 is shown in Figure 4.42. The downward vertical motion at  $x = -2$  pinpoints the location of M1. Note the vertical velocity extending from the upper layers to the surface. In the area of  $x = 2$ , the second microburst, M3, will eventually develop in the coming minutes. At 1845, it is an area of negative vertical velocity that does not yet extend to the surface.

The perturbation pressure field is displayed in Figure 4.43. The strong pressure gradient and large value of

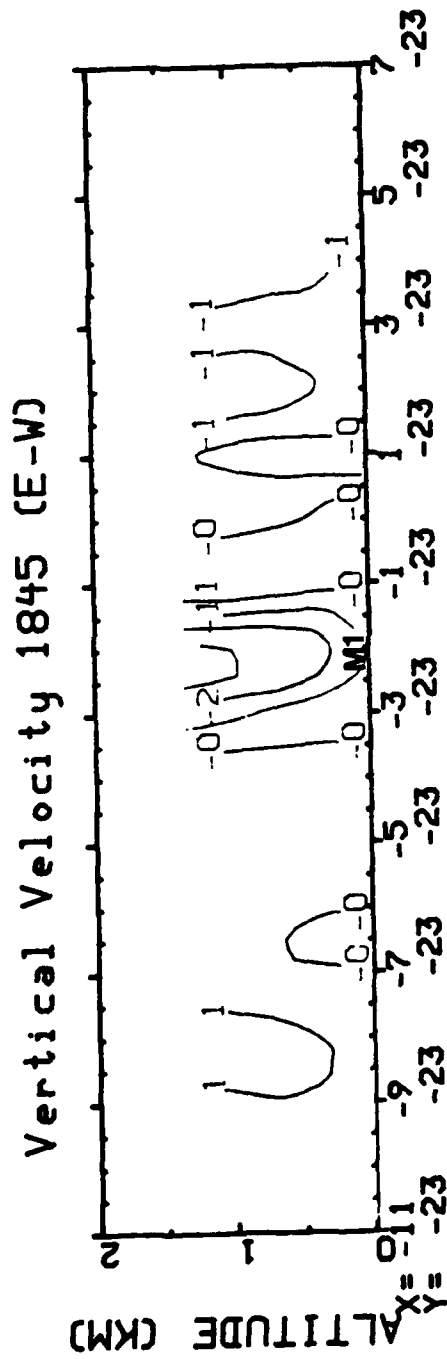


Fig 4.42 Same as Fig 4.41, except for vertical velocity.



pressure perturbation associated with M1 is shown in the vicinity of  $x = -2$ . There is a positive pressure perturbation associated with the gust front in the area of  $x = 0$  due to the low-level converging air mass at the front.

#### 4.2.2.b (E-W) Cross-Section at 1847

The reflectivity pattern for the 1847 E-W cross-section is shown in Figure 4.44. The most striking feature is the rapid development of M3 in the vicinity of  $x = 1.5$ . This rapid downflow has now extended throughout the upper three layers, while two minutes earlier, it was confined to the upper two only. The flow from the downdraft is just beginning to break through to the surface, so I now consider this downdraft to be a microburst. The full effect of M3's downdraft at the surface is not complete, and will be much more pronounced at 1850.

The vertical velocity field shown in Figure 4.45. The downward vertical velocity of M1 reveals the microburst is intensifying as evidenced by the appearance of a  $-3$  m/sec vertical velocity at the 1 km level. In addition, the downdraft at  $x = 1.5$  has intensified as it nears the surface.

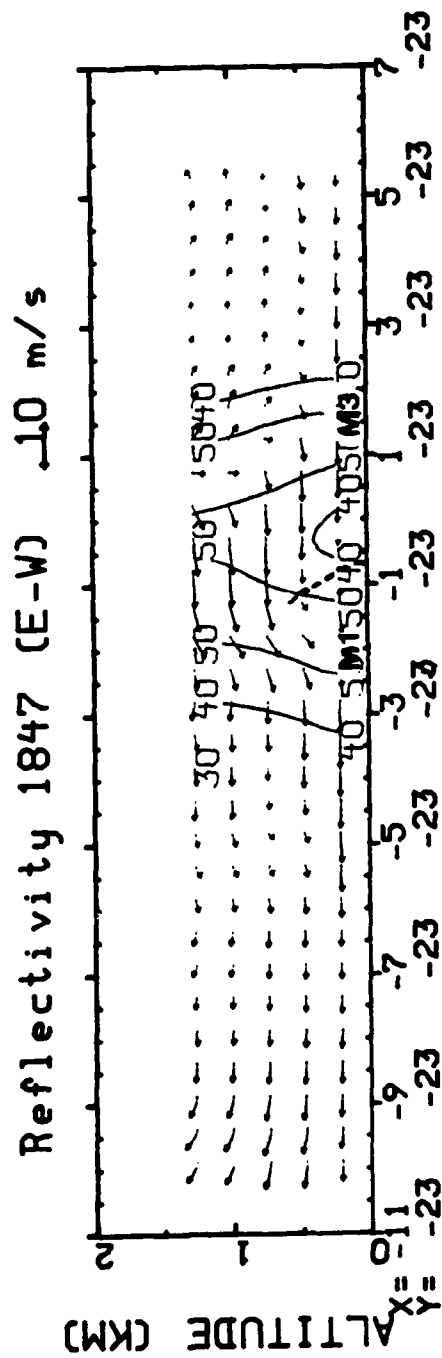


Fig 4.44 E-W cross-section of the reflectivity field for 1847 MDT.



# Vertical Velocity 1847 (E-W)

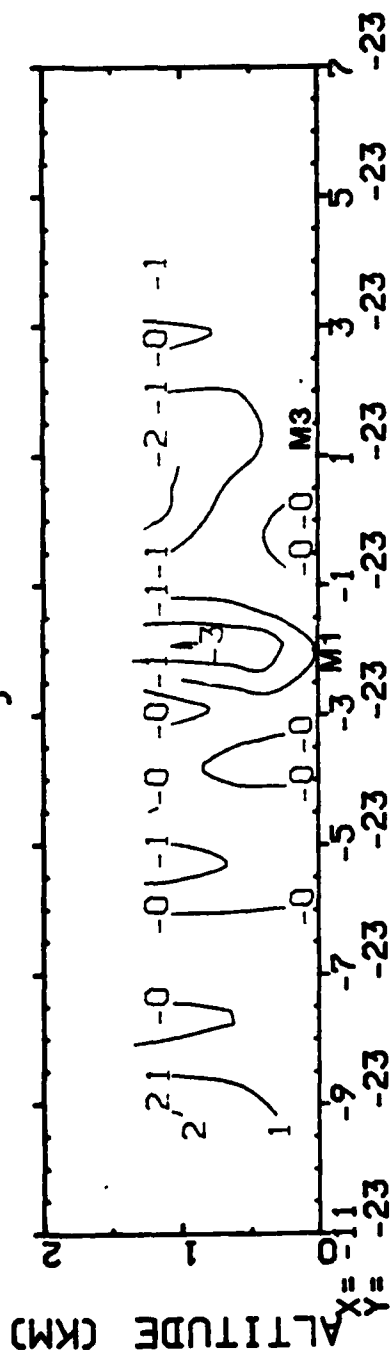


Fig 4.45 Same as Fig 4.44, except for vertical velocity.

#### 4.2.2.c (E-W) Cross-Section at 1850

The (E-W) reflectivity and wind flow field cross-section for the 1850 time period is shown in Figure 4.46. The wind flow is characterized by an increase in turbulent motion, and the intensification of M3. By this time period, M3 is definitely a microburst and has developed considerably between 1847 and 1850. In the span of only three minutes, the flow of the downdraft has reached the ground and the divergent flow pattern that characterizes a microburst is evident. Note the outflow at the surface near  $x = 1.5$  where M3 has reached the ground and diverges horizontally. The area between M1 and M3 is interesting because of the opposition of the outflows of each microburst, although the outflow of M1 continues to be stronger than that from M3. Note that the outflow of M1 opposes that of M3 and so has diminished substantially in velocity due to this opposition by the outflow of M3. The gust front between M1 and M3 is visible just to the left of M3, but is diminished in intensity because M3's outflow has effectively blocked the environmental flow. On the downwind side of M3, the environmental wind does not interact with the outflow of M1 as it did before M3's downdraft reached the ground.

The vertical velocity field is shown in Figure 4.47. The two microbursts are plainly seen as the areas of nega-



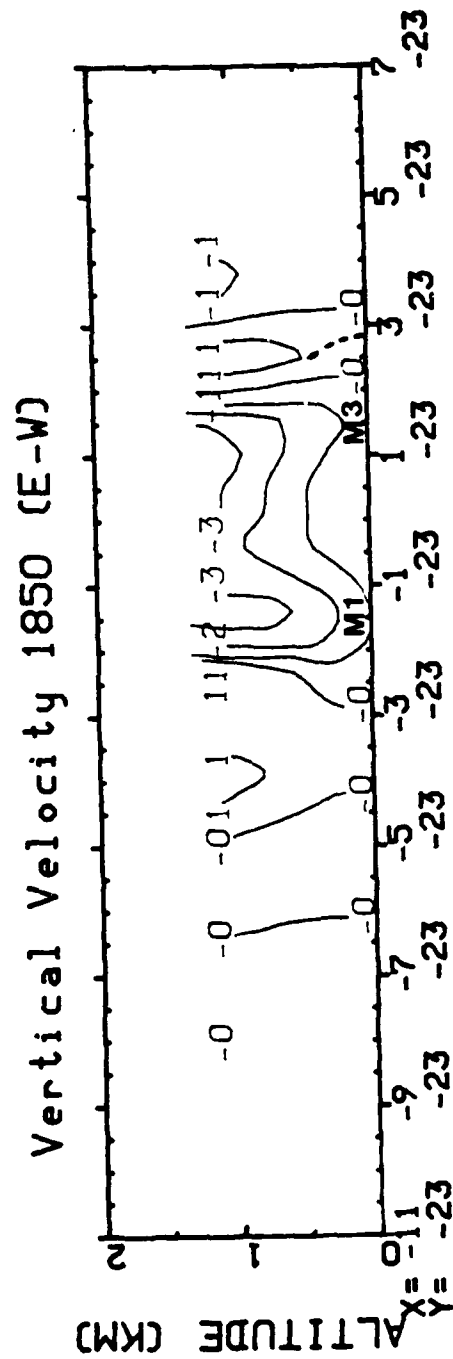


Fig 4.47 Same as Fig 4.46, except for vertical velocity.

tive vertical velocity that extend from the upper layers to the surface. It would appear that M3 is not as strong as M1 based on the vertical velocity pattern. The gust front to the right of M3 shows up as an area of weak positive vertical motion. As M3 swells, the gust front should also intensify as the velocity of descending air within the microburst grows.

The pressure pattern at 1850 is shown in Figure 4.48. Note the strong positive pressure perturbations where the microbursts strike the surface. The pressure pattern with local time tendency is considered should show more detail in the perturbation pressure field and also the temperature field.

The temperature field for the 1850 time period is shown in Figure 4.49. Note the negative temperature perturbation in the vicinity of  $x = -1$  to  $1$  caused by the apparent merger of the precipitation-cooled outflows from the two microbursts.



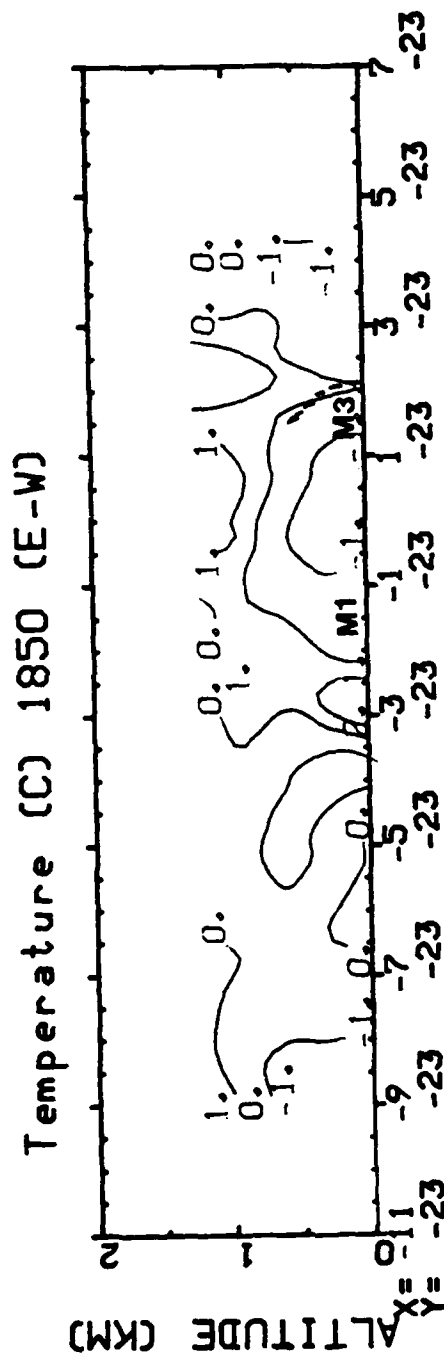


Fig 4.49 Same as Fig 4.46, except for temperature  $T'_{vd}$ .

#### 4.3 Plan View Plots (tendency included)

Inclusion of the local tendency terms in the momentum equations used to derive the perturbation pressure field should enhance the definition and overall accuracy of the plotted perturbation pressure and temperature fields. The thermodynamic retrieval process of Gal-Chen (1978) uses the momentum equations to derive perturbation pressure from the wind field. The increased accuracy and detail of these thermodynamic fields will better define development and structure of the microbursts during the 1845-1850 time period.

Horizontal plots of perturbation temperature and pressure are used for 5 levels, beginning with 0.25 km, up to 1.25 km, just as in the non-tendency case. These plots use the same grid spacing as the non-tendency plots of temperature and pressure.



#### 4.3.1 1845 Plan View Plots

The perturbation pressure field for 1845 (with tendency included) is shown in Figure 4.50. As expected, there is a positive pressure perturbation where the downflow from M1 reaches the ground. Directly to the east of M1, there is a large positive pressure perturbation as the environmental winds and the outflow from M1 combine at the gust front. Note the well-defined pressure gradient to the north of the microburst as the diverging outflow from the microburst spreads. The wind flow field shows little effects of D2 at the surface; however, the pressure gradient caused by the upper-level downward vertical motion of D2 is plainly visible just to the north of the downdraft, and much better defined than in the non-tendency plot for 0.25 km at 1845 ( Fig 4.3).

The temperature field for the first level is shown in Figure 4.51. Note the cold anomalies in the vicinity of M1. As expected, the outflow is colder than the environmental winds at the surface since the downdraft has been cooled. The cool outflow is to the southeast of M1 and is well detailed in this temperature plot.

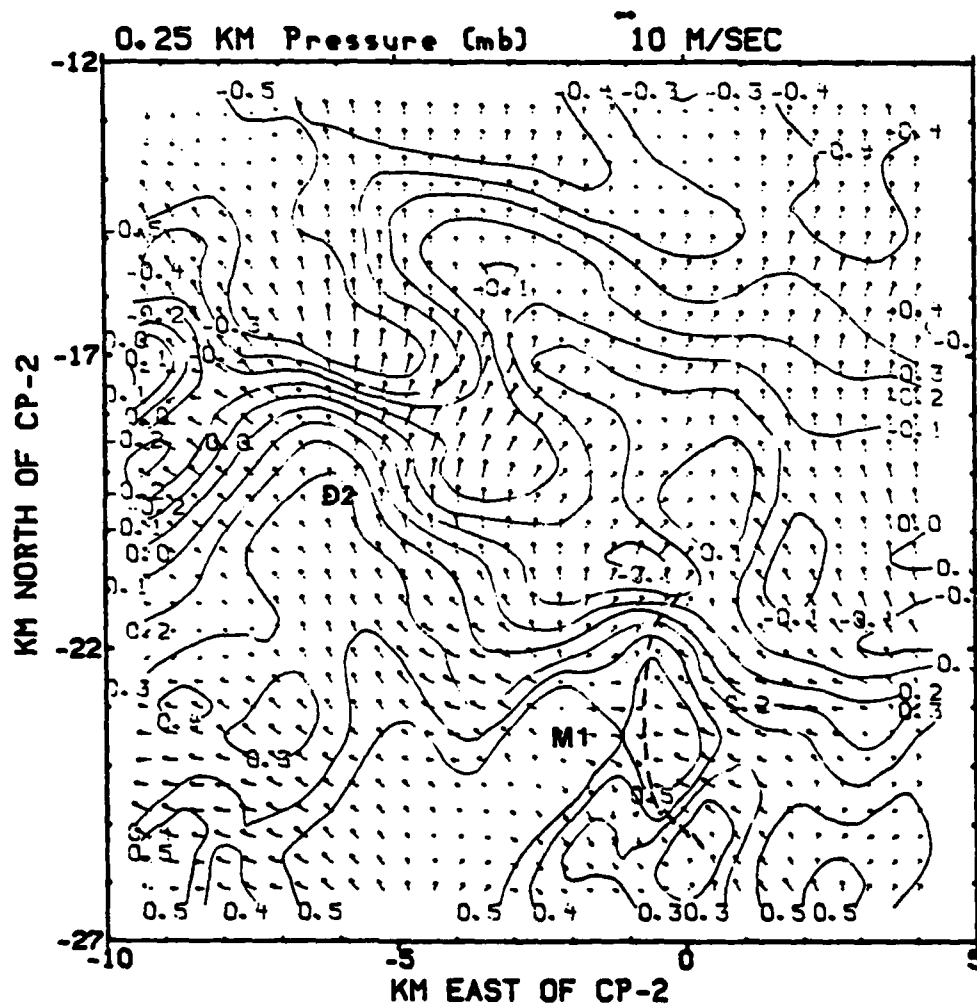


Fig 4.50 Plan view of the horizontal wind field and pressure field (tendency included) for 1845 MDT at 0.25 km.

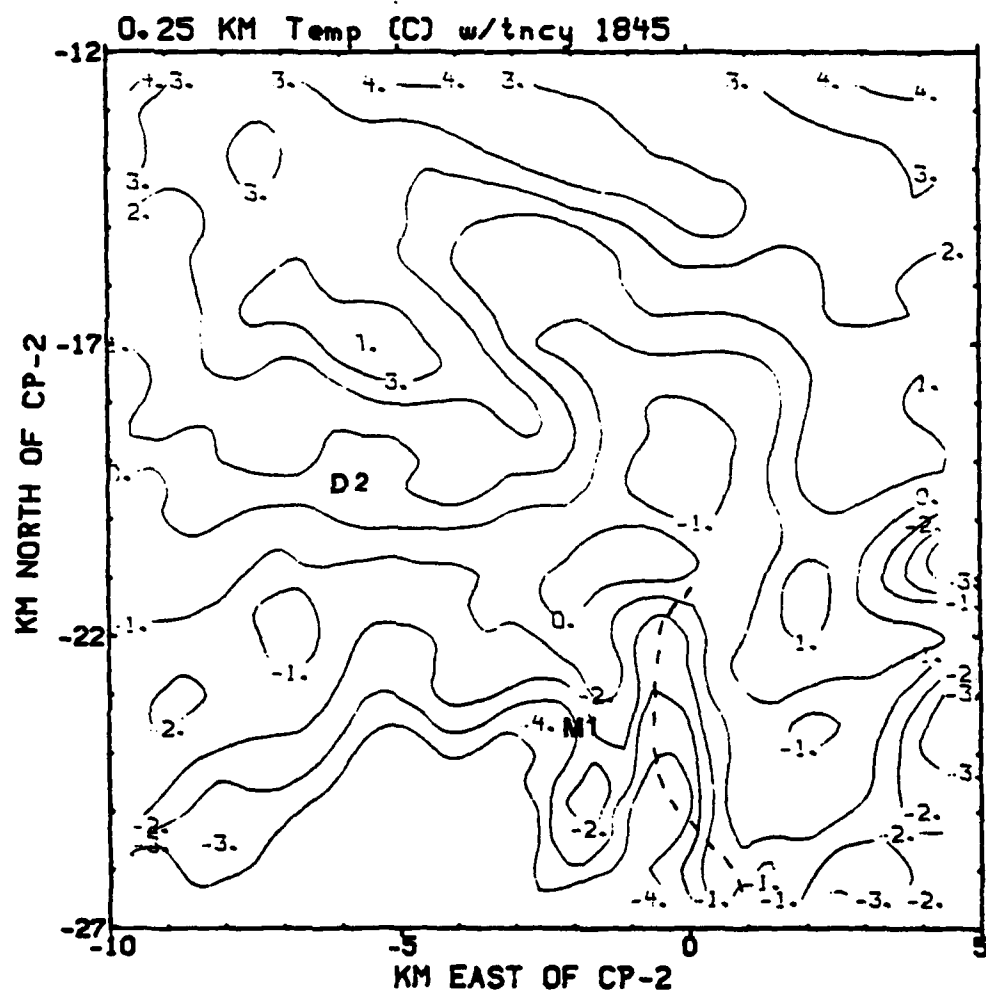


Fig 4.51 Same as Fig 4.50, except for temperature  $T'_{vd}$ .

The 1845 pressure pattern for 0.5 km is shown in Figure 4.52. The most interesting feature here is the large value of positive perturbations associated with M1 and D2. The descending air causes a positive pressure perturbation due to compression. Of course, the area of positive pressure perturbation is much greater for microburst than for the downdraft, since the microburst extends to the surface.

The temperature field for 0.5 km is shown in Figure 4.53. The cool air from the outflow of M1 is lifted at the gust front, as depicted by a strong negative temperature perturbation of  $-3^{\circ}$  C in the frontal boundary area. The cool downdraft associated with D2 does not appear at this level.

The 0.75 km perturbation pressure field (Figure 4.54) shows the strong pressure gradient at the microburst. D2 still shows a weak pressure field at this level. There is a well-defined horizontal pressure gradient in the vicinity of the gust front as convergence at the levels below is felt at 0.75 km. The temperature field at 0.75 km is inconclusive and shows little improvement in definition over the non-tendency field already discussed.

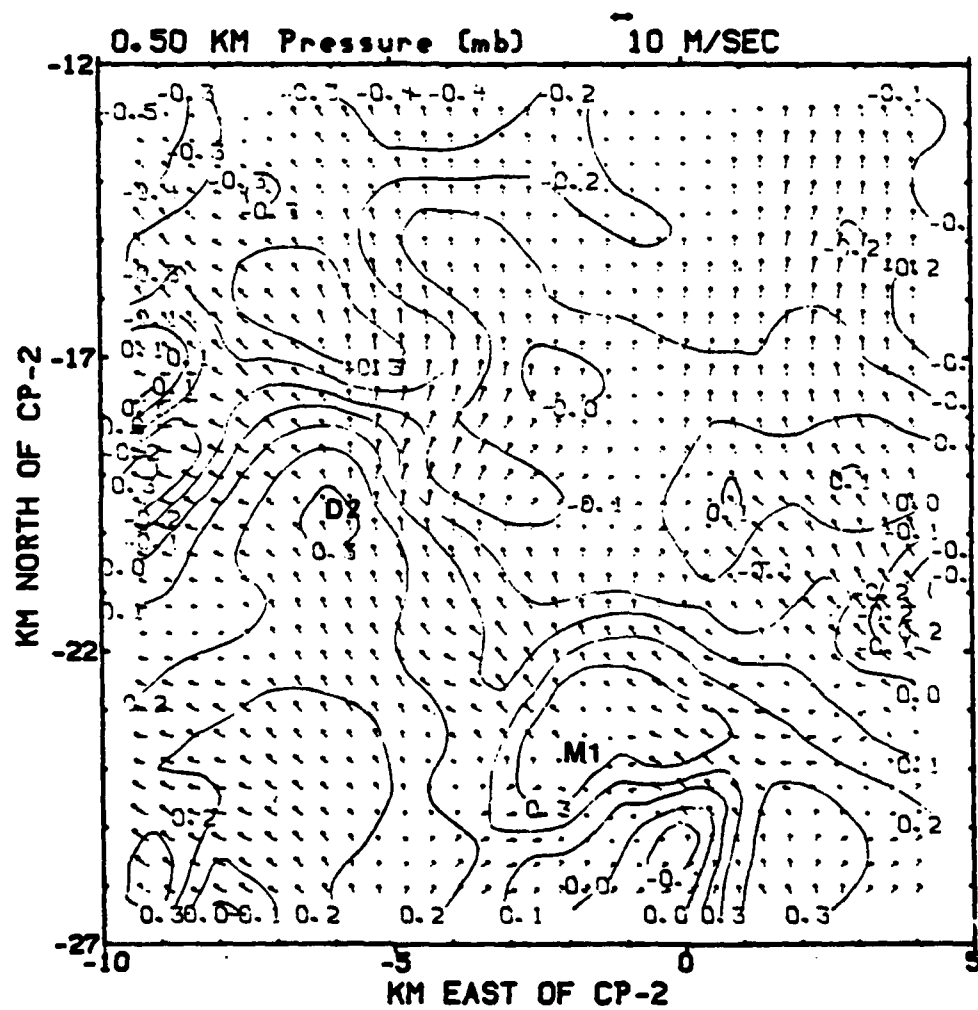


Fig 4.52 Same as Fig 4.50, except for 0.5 km.

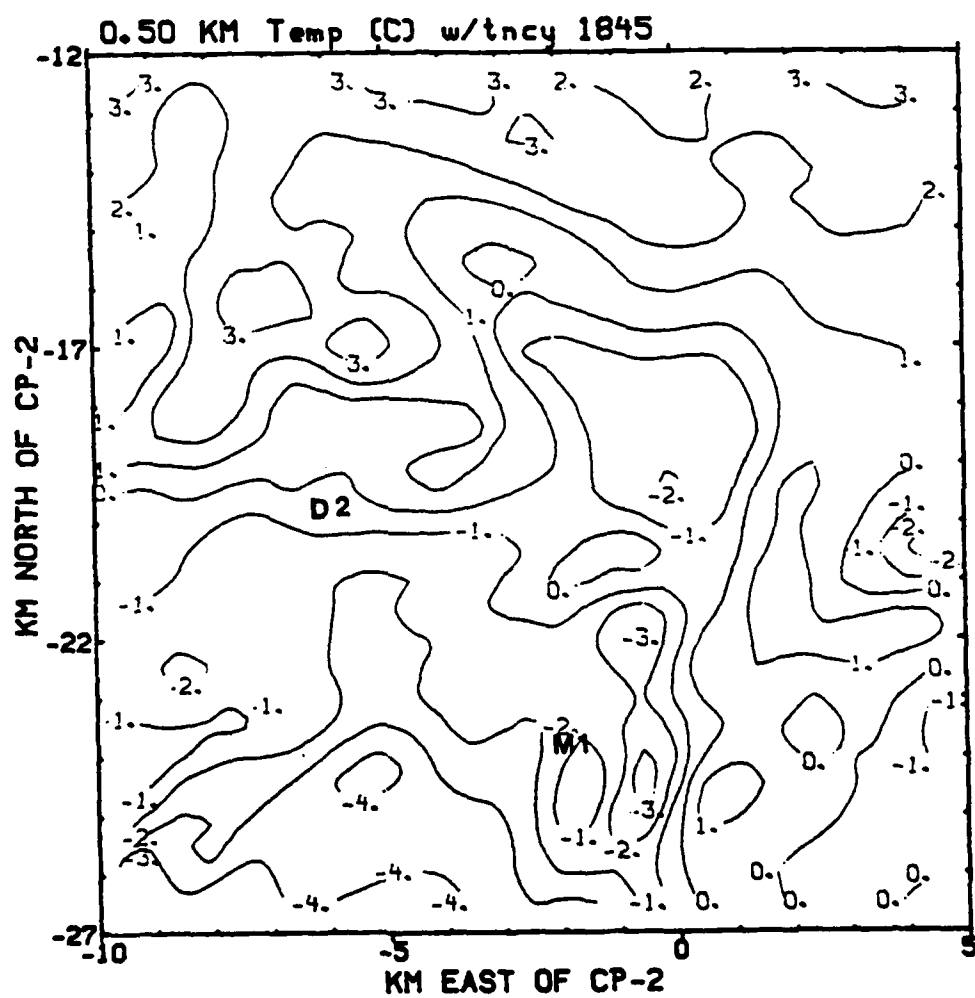


Fig 4.53 Same as Fig 4.51, except for 0.5 km.

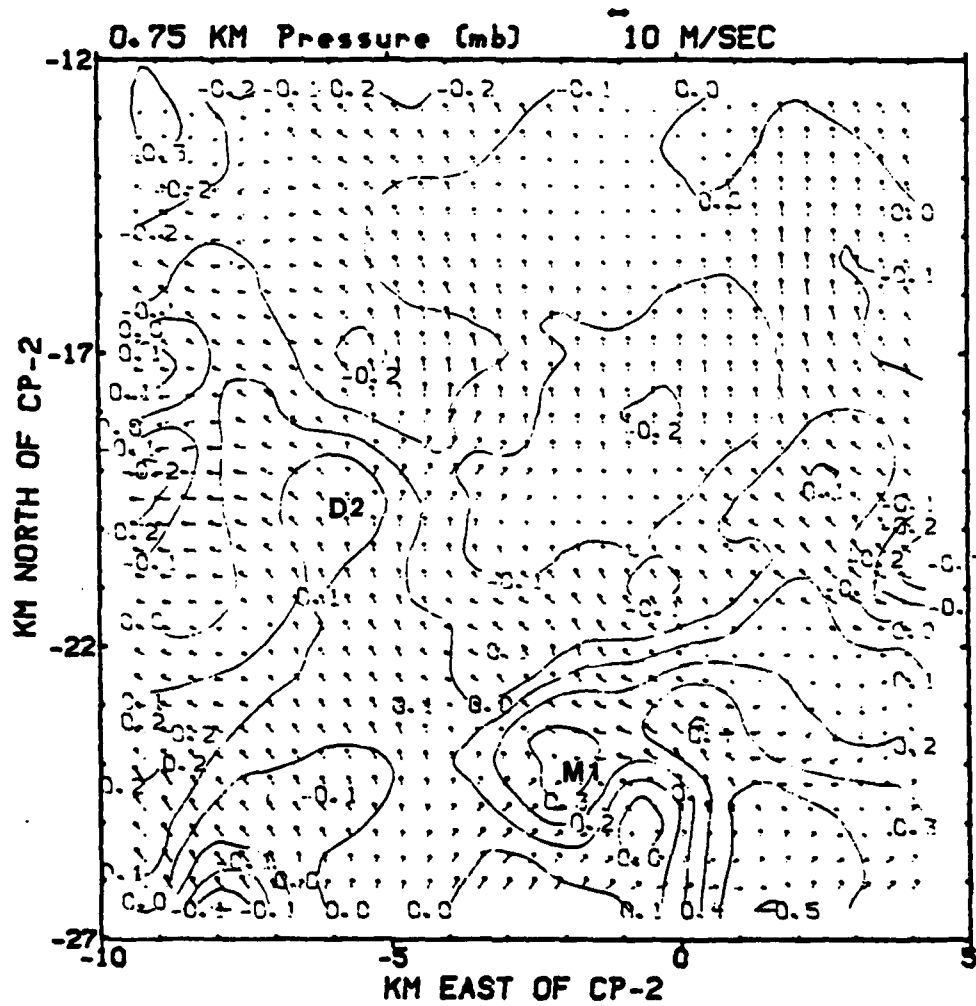


Fig 4.54 Same as Fig 4.50, except for 0.75 km.

The 1 km pressure field is shown in Figure 4.55. Note the area of negative pressure perturbation just to the north of M1, just beyond the northern most extent of the gust front where winds tend to diverge. The negative pressure perturbations that accompany a divergent wind pattern are being felt even at 1 km above the surface.

The temperature field for 1 km is displayed in Figure 4.56. Recall from the wind field pattern that environmental air begins to be drawn into the downdraft at this level. Note the negative temperature perturbations as this cooler environmental air is being funnelled into the downdraft.

The temperature pattern for 1.25 km, shown in Figure 4.57, shows a well defined temperature gradient near M1 as cool, dry environmental air is entrained into the microburst's downdraft. There is, as yet, no evidence of such entrainment into the downdraft that eventually develops into M3, nor is there any into D2. The entrainment of upper-level cool air is a key factor in microburst maintenance. Entrainment of dry air is directly related to the strength of the microburst, and this temperature field plot provides clues to the increasing strength of the microburst by detailing the entrainment of the cooler air. The inclusion of the local tendency terms into the momentum equations allows this well-defined temperature plot.



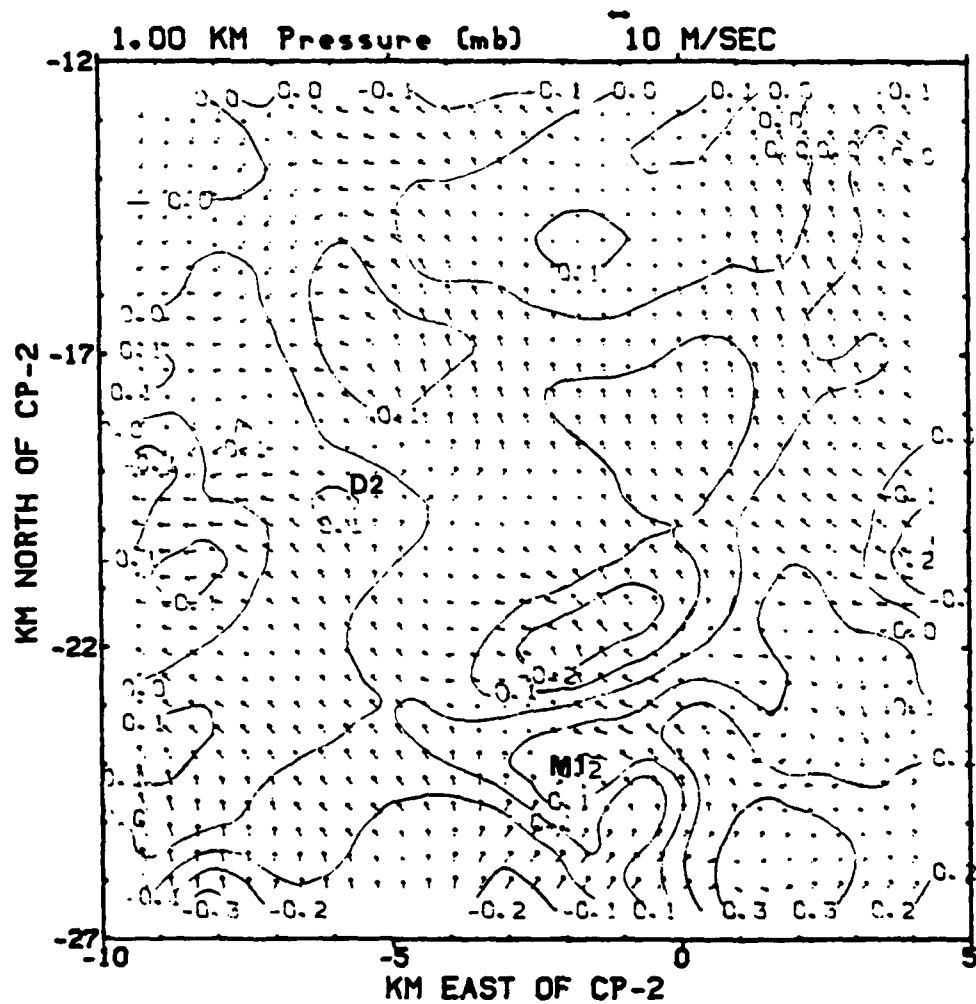


Fig 4.55 Same as Figure 4.50, except for 1 km.

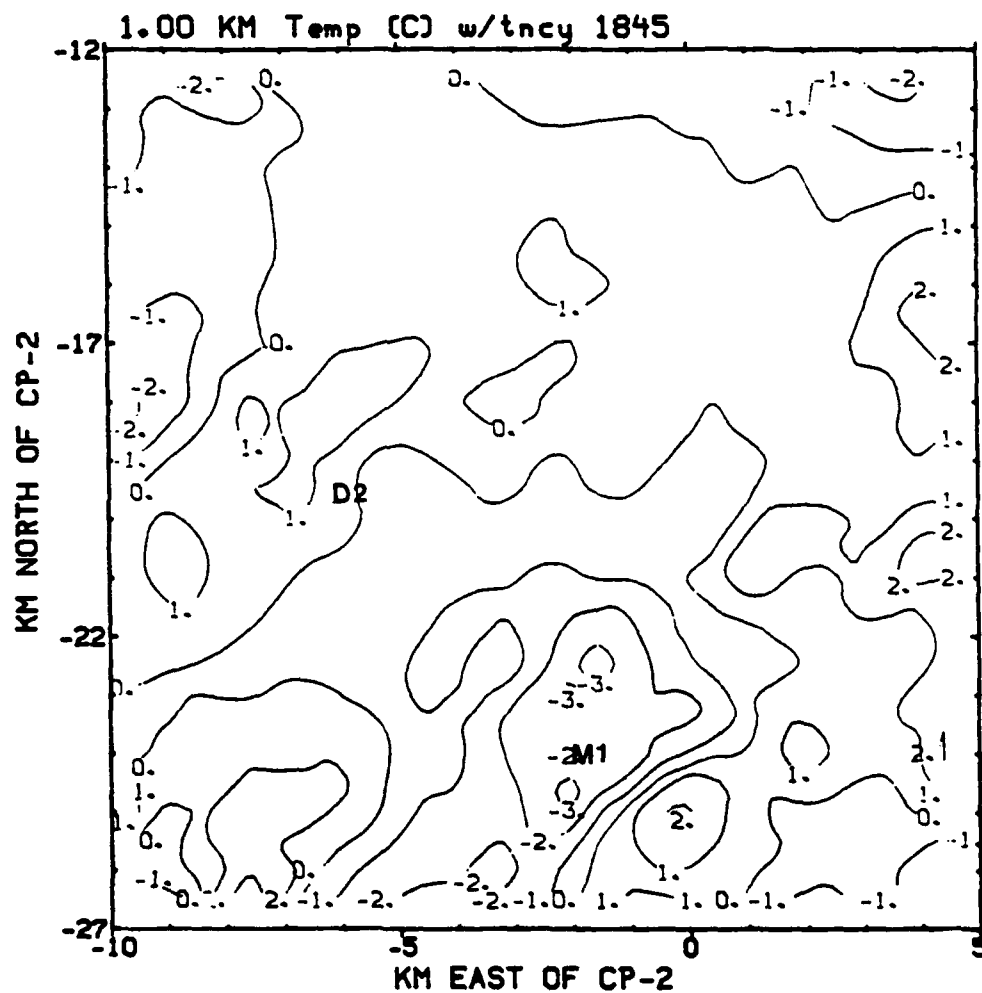


Fig 4.56 Same as Figure 4.51, except for 1 km.

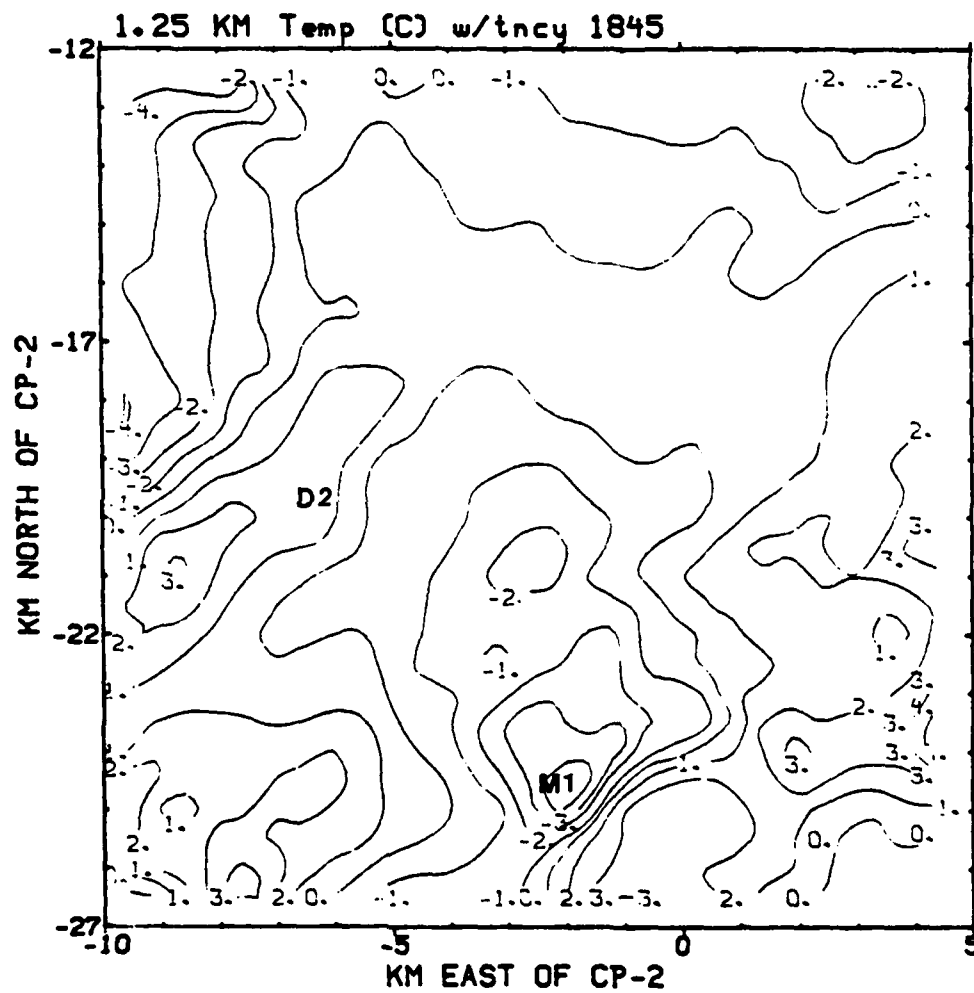


Fig 4.57 Same as Figure 4.51, except for 1.25 km.

#### 4.3.2 1847 Plan View Plots

The 1847 time period uses a three minute forward tendency (1850-1847) in the momentum equations to enhance the retrieved pressure field. The perturbation pressure field for 0.25 km is shown in Figure 4.58. Note the strength of the perturbation pressure gradient to the north and northwest of M1. This gradient is a result of the microburst's horizontally diverging outflow. At the gust front boundary, (0, -23), there is a large area of strong positive pressure perturbation due to convergence. The downdraft, D2, shows a larger pressure gradient than it did only two minutes ago at 1845, indicating a growth in strength of the downdraft. The wind flow indicates the downdraft itself has not reached the surface; however, the effects of the descending air of the downdraft is manifested by positive pressure perturbations at 0.25 km.

The temperature perturbation field for the 0.25 km level is shown in Figure 4.59. The enhanced temperature field shows the cooled air as it strikes the surface and spreads easterly to form the gust front boundary. The advantage of including the local time tendency term in the momentum equations is clearly displayed in this temperature plot. The resolution of this retrieved temperature field over the plot for the without tendency case is clearly evident (i.e., Fig 4.15, which is the 1847 non-

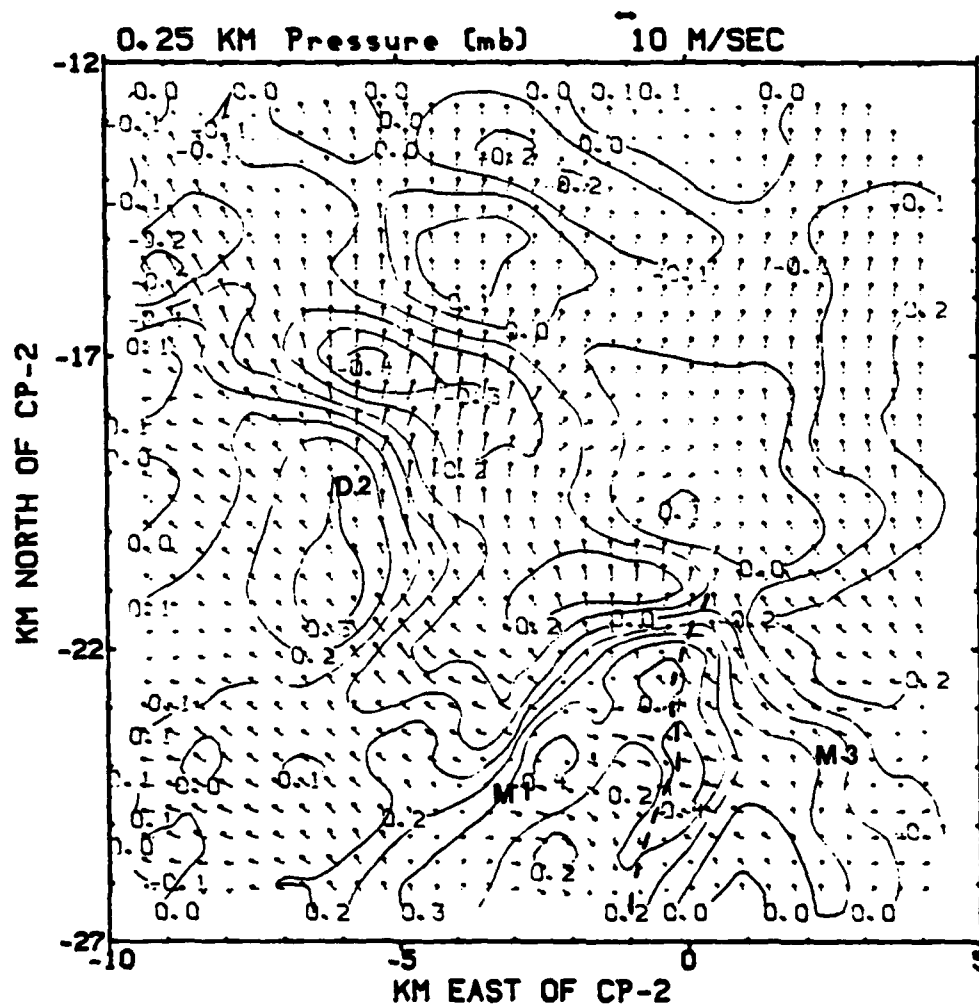


Fig 4.58 Plan view of the horizontal wind field and pressure field (tendency included) for 1847 MDT at 0.25 km.

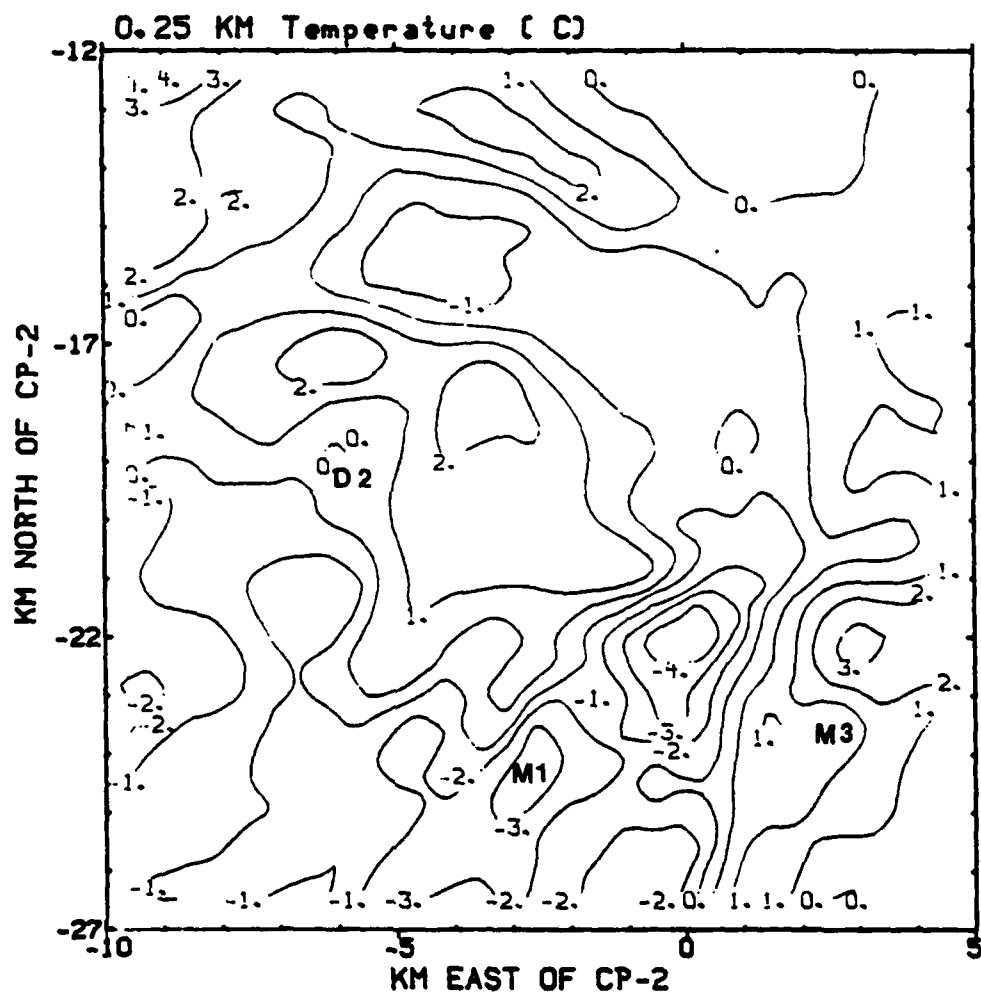


Fig 4.59 Plan view of the temperature field  
(tendency included) for 1847 MDT at 0.25 km.

tendency considered temperature plot for 0.25 km.)

The pressure plot for 0.5 km is shown in Figure 4.60. In the gust front area between M1 and M3, the positive pressure perturbation has grown since 1845. The surface outflow of M3, although rather weak at 1847, has contributed to the increased perturbation pressure at the gust front.

The temperature plot for 0.5 km is shown in Figure 4.61. Again, note the strong negative temperature perturbation at the gust front boundary, extending from south to the northeast of M1, denoting the area of rising air.

The 0.75 km pressure perturbation plot is shown in Figure 4.62. The negative temperature perturbation that coincides with the northern edge of the gust front extends to this level. The negative pressure perturbation at (0,-22) coincides with the diverging wind field near the northern most area of the gust front. The positive pressure perturbation associated with D2 has grown considerably since 1845 (0.1 to 0.3 mb) as the downdraft continues to grow.

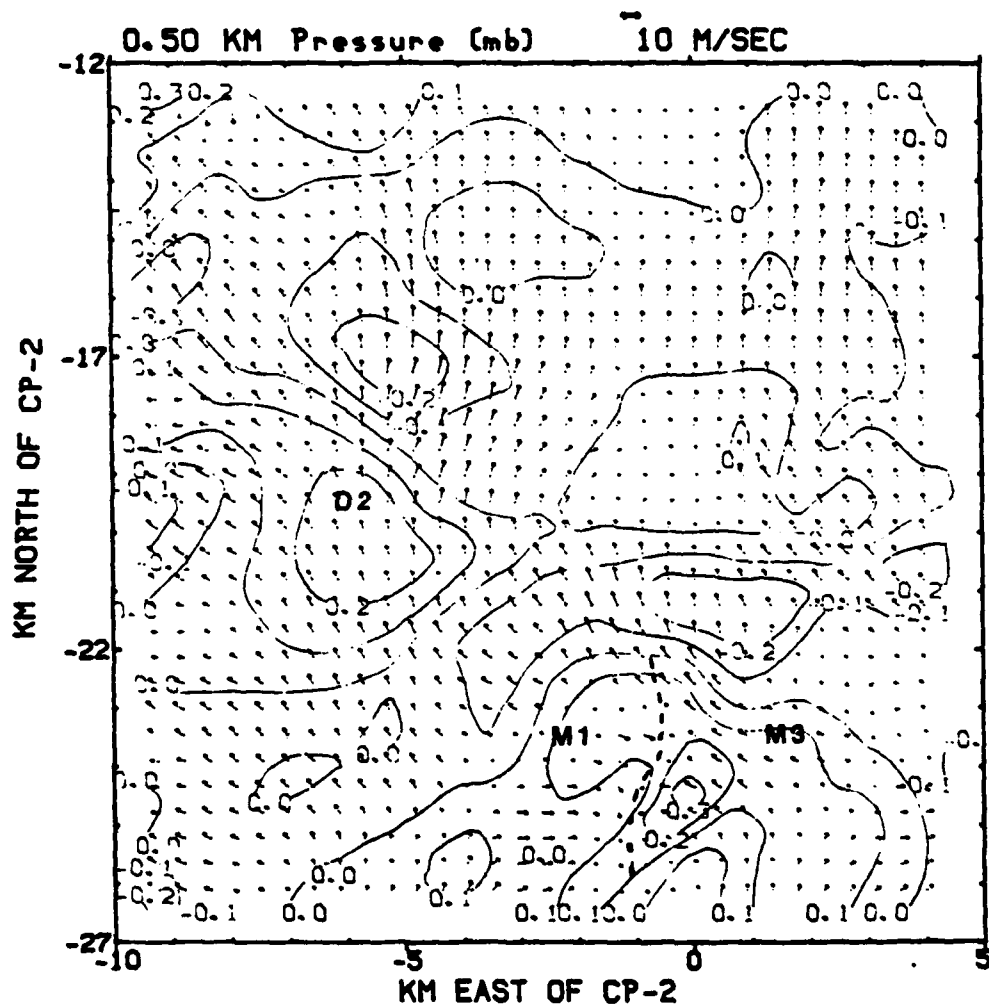


**Fig 4.60** Same as Fig 4.58, except for 0.5 km.



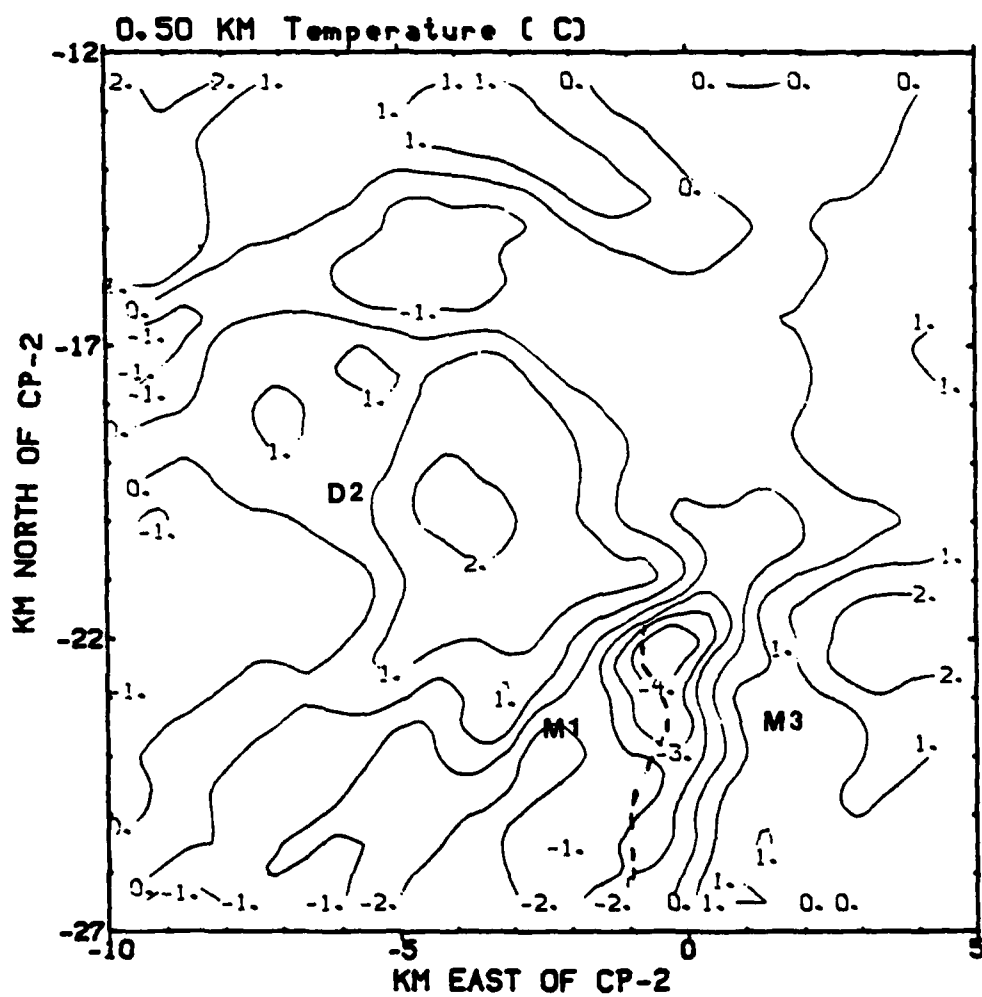


Fig 4.61 Same as Fig 4.59, except for 0.5 km.

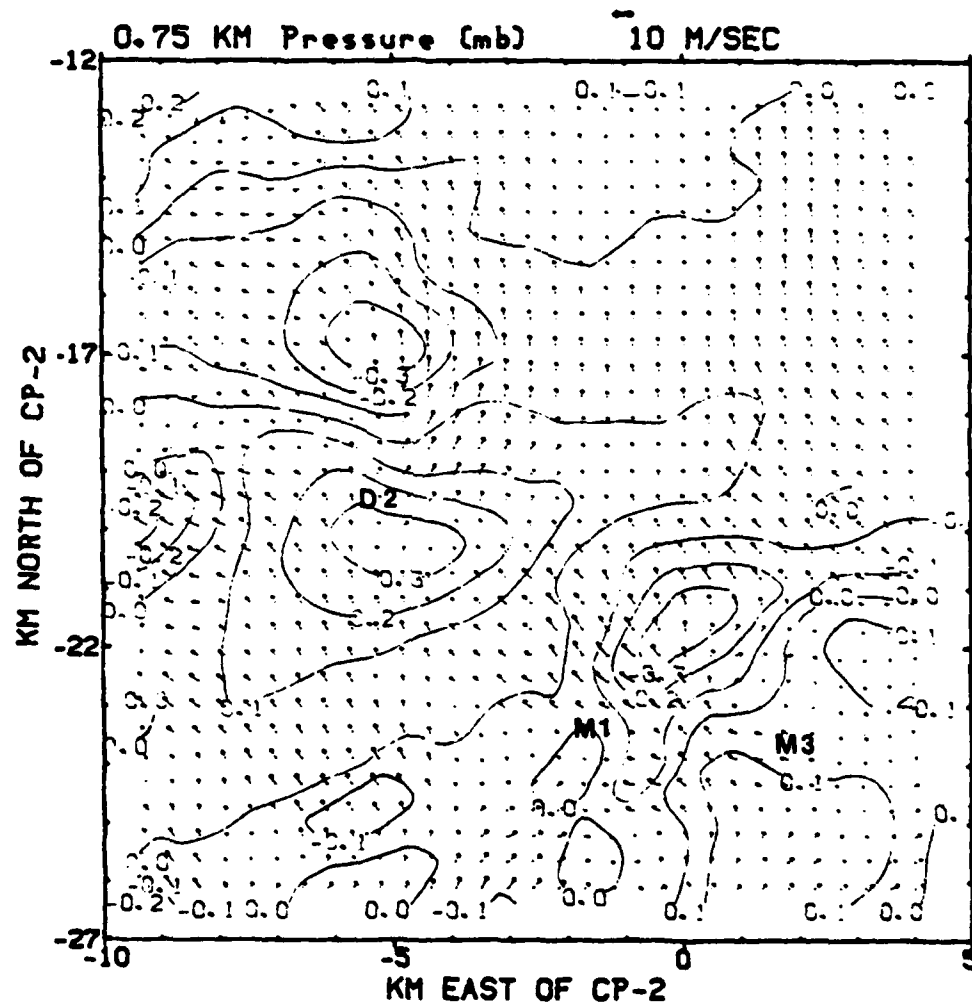


Fig 4.62 Same as Fig 4.60, except for 0.75 km.

The pressure field for the 1 km level is shown in Figure 4.63. Note the strong negative pressure perturbation immediately to the north of D2, which identifies an updraft that helps supply the downdraft with moist air. The pressure field change from 1845 to 1850 indicates a growth in intensity of D2, and a key reason must be this area of upward vertical motion. Air rising at the gust front just to the east of M1 is also depicted. This rising air can also be used as a source of warm, moist air, not only for M1, but for the developing M3. The detail in this pressure field helps identify these regions of upward vertical motion that can be used to channel warm, moist air to both microbursts and D2.

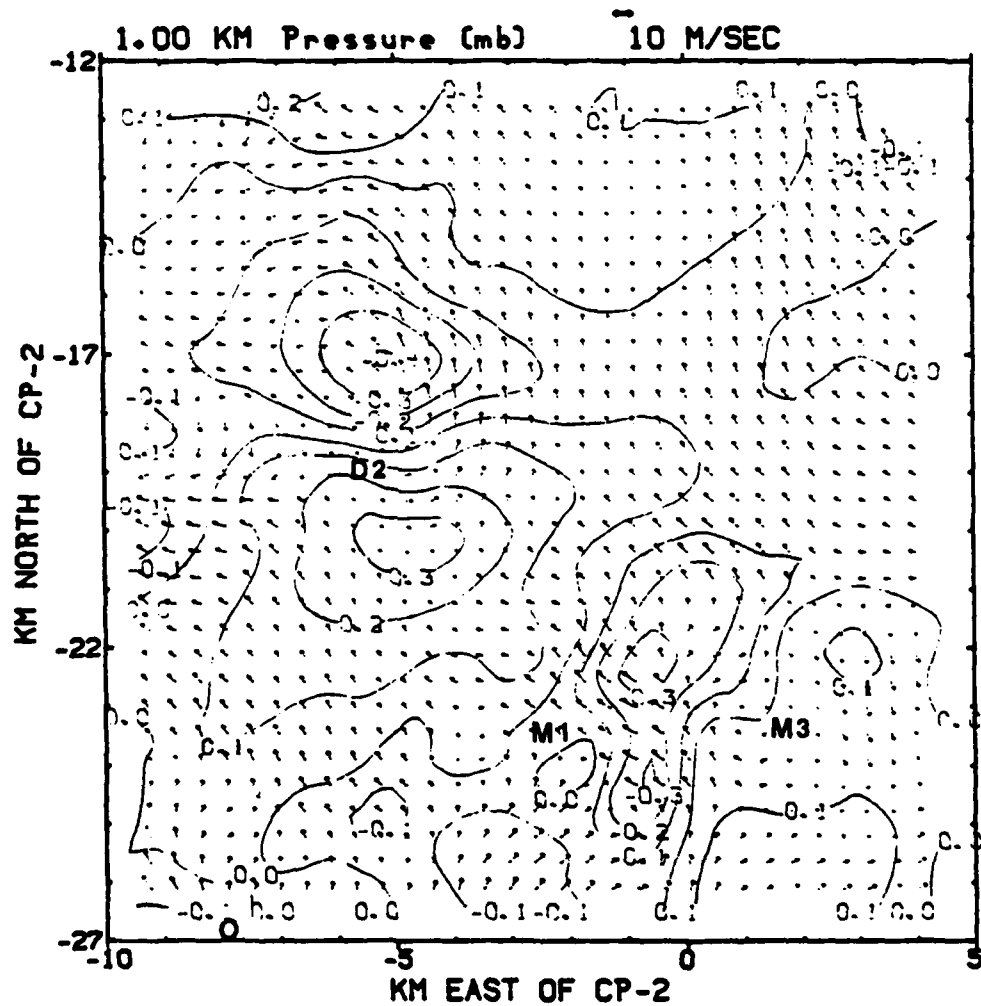


Fig 4.63 Same as Fig 4.62, except for 1 km.

#### 4.3.3 1850 Plan View Plots

The 1850 plan view plots (with tendency) will now be discussed, beginning with perturbation pressure at 0.25 km (Figure 4.64). Note the well-defined perturbation pressure gradient as a result of the combined outflows of the two microbursts. As M1 and M3 grow, the low-level perturbation pressure gradient increases with time, due to the combined outflow of both M1 and M3 and the observed bow-echo effect just to the north of M1.

The temperature plot for 1850 at 0.25 km is shown in Figure 4.65. Strong negative temperature perturbations are apparent in the gust front area as the cool outflows of both M1 and M3 merge. Note that the downdraft, D2, is beginning to cause an increase in perturbation pressure being felt at the surface, as evidenced by the  $-1^{\circ}$  temperature perturbation for the downdraft as D2's downward flow moves ever-closer to the surface.

The 0.5 km pressure perturbation plot is shown in Figure 4.66. Again, the strong pressure perturbations near M1 and M3 are apparent. The area of positive pressure perturbation near D2 has increased in size, indicating continuing growth of the downdraft. It seems D2 is ready to extend to the surface, and be upgraded to a microburst.



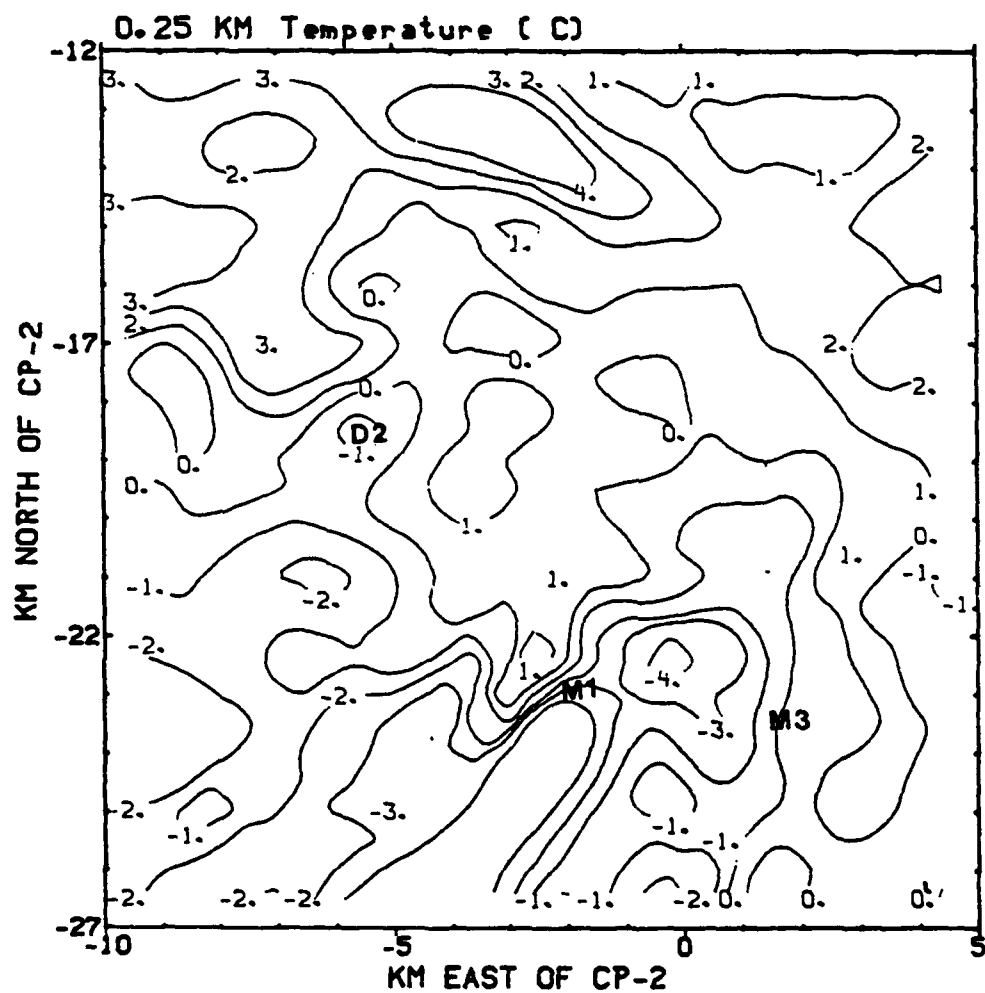


Fig 4.65 Plan view of the temperature field  
(tendency included) for 1850 MDT at 0.25 km.





The perturbation pressure plot for the 0.75 km level is seen in Figure 4.67. Just to the north of the microbursts, note the strong negative pressure gradient. This is the rising air, forced by the gust front, that serves as a "feeding" mechanism of warm, moist air for the microbursts. The gust front is thus a feed-back device that helps to sustain a microburst by providing moist low-level air to the storm. Such a supply system is now apparent immediately to the north of D2. This increase in low level air is another reason to speculate D2 is ready to extend to the surface. D2's downdraft has taken so long to develop sufficiently to reach the surface because of interference by M1 of low-level inflow. As a result, D2 grows slowly to the surface and can not diverge its outflow to form a gust front boundary to be used as a mechanism to further its supply of warm moist air. It would appear, based on this plot, that D2 is now getting a supply of moist low-level air, and its downflow should soon extend to the surface.

The 1.25 km pressure and wind flow plot is shown in Figure 4.68. The flow of environmental air toward both M1 and M3 is evidenced by the windflow profile and the turning of the winds toward the microburst cores. It appears that D2 is also beginning to attract high momentum upper-level air, especially just to the north of its downdraft. A cyclonic-like flow is visible just to the north of D2 to



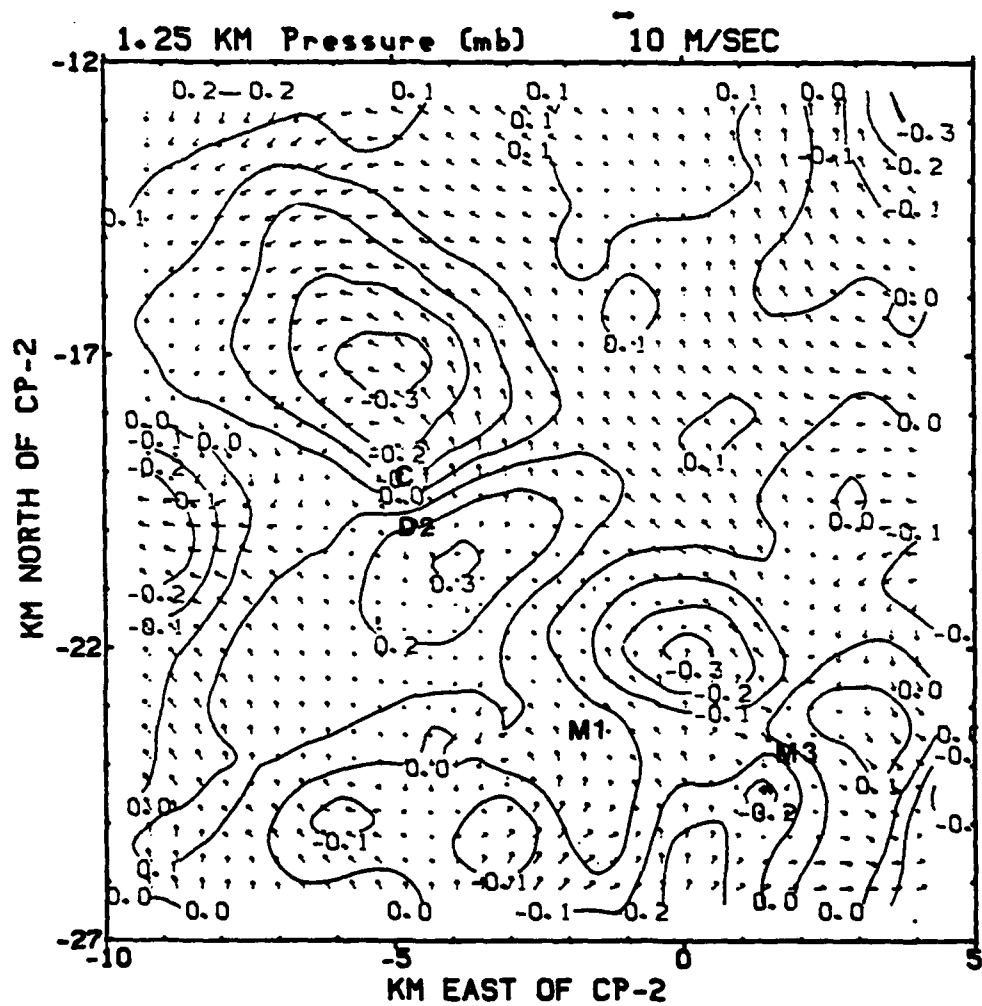


Fig 4.68 Same as Fig 4.64, except for 1.25 km.

steer air to the downdraft. Moist low-level air channeled in the the updraft just north of D2 (-5, -17) is available to supply the downdraft with low-level moist air. D2 will gain strength because of upper-level entrainment and evaporative cooling of moist air within the downdraft. Based on this perturbation pressure plot, D2's updraft is nearly equal to that supplying both of the microbursts. Clearly, D2 is gaining strength.

#### 4.4 Cross-Section Plots (tendency included)

The same two cross-section orientations that were examined in the non-tendency cases will be used in the tendency-included discussion of cross-sections. The difference in the plots is the inclusion of the local tendency terms excluded from the momentum equations used to derive the perturbation pressure field. For the tendency-included cases, the addition of these terms in the momentum equations enhances the definition of the recovered perturbation pressure and temperature fields, just as in the plan-view plots.

Two cross-section configurations are used for these cross-section plots. One has a northwest-southeast (NW-SE) orientation, while the other is east-west (E-W).

##### 4.4.1 (NW-SE) Cross-Section at 1845

The 1845 cross-section of the pressure field (NW-SE) (with tendency considered) is shown in Figure 4.69. The surface meso-high where the air from the microburst's downdraft converges at the surface is clearly shown at  $x = -2$ . To the right of M1, the strong positive pressure perturbation at the gust front shows the converging air and the associated increase in perturbation pressure, as evidenced by the 0.6 mb perturbation pressure increase at  $x =$

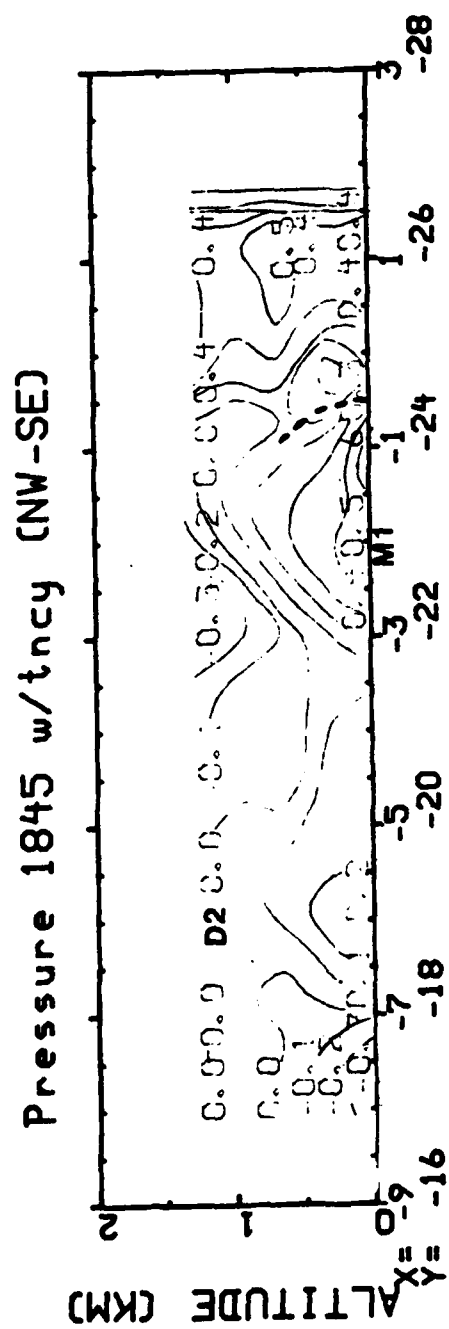


**Fig 4.69 NW-SE cross-section of the pressure field  
(tendency included) for 1845 MDT.**

-1. This strong pressure gradient at the gust front and the clarity with which it is displayed underlines the advantage of including local tendency terms in the momentum equations used in pressure retrieval (i.e., Figure 4.33, which was the same cross-section with tendency not considered). The increase in definition of the perturbation pressure isobars over the non-tendency case makes a strong point for the inclusion of the local tendency term in the momentum equations. Overall accuracy of the recovered perturbation pressure field helps to better define the physical processes in progress during the evolution of the microburst.

The temperature field of the (NW-SE) 1845 cross-section is shown in Figure 4.70. As with the pressure field discussed in the previous paragraph, the temperature field shows a marked improvement over the non-tendency plot for the same orientation and time period. Note the temperature gradient where the precipitation-cooled air from the microburst outflow collides with the warm environmental air at the gust front ( $x = -1$  to  $0$ ). The descending cool air in the upper levels is shown at  $x = -2$  as environmental air from the upper levels descends into warmer air. As with the pressure plot, the temperature plot is better defined when tendency is included in the retrieval process.

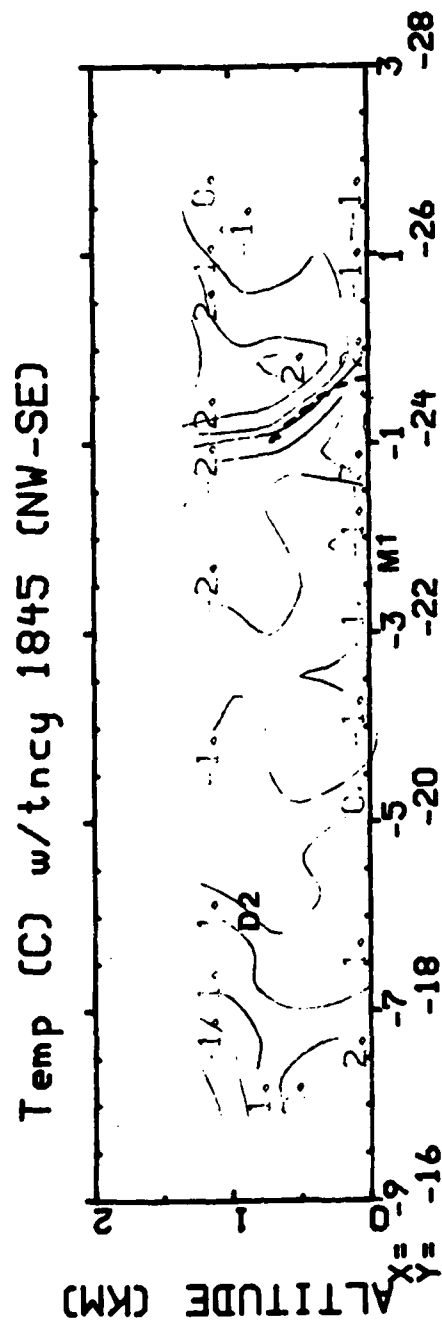


Fig 4.70 NW-SE cross-section of the temperature field  
(tendency included) for 1845 MDT.



#### 4.4.2 (NW-SE) Cross-Section at 1847

The 1847 (NW-SE) cross-section plot (with tendency considered) is shown in Figure 4.71. In the two minutes since 1845, the positive pressure perturbation at the gust front has increased as the outflow from M1 continues to converge in the vicinity of  $x = -1$ . The strong meso-high at  $x = -2$  clearly defines the point where M1's downdraft reaches the surface. The descending downdraft of D2 and the associated surface pressure gradient increase is shown at  $x = 6$ .

The temperature plot for 1847 is shown in Figure 4.72. Again, the temperature gradient at the gust front shows the differential in environmental flow and the outflow of M1, as the cooled outflow from the microburst is lifted on the left side of the gust front.

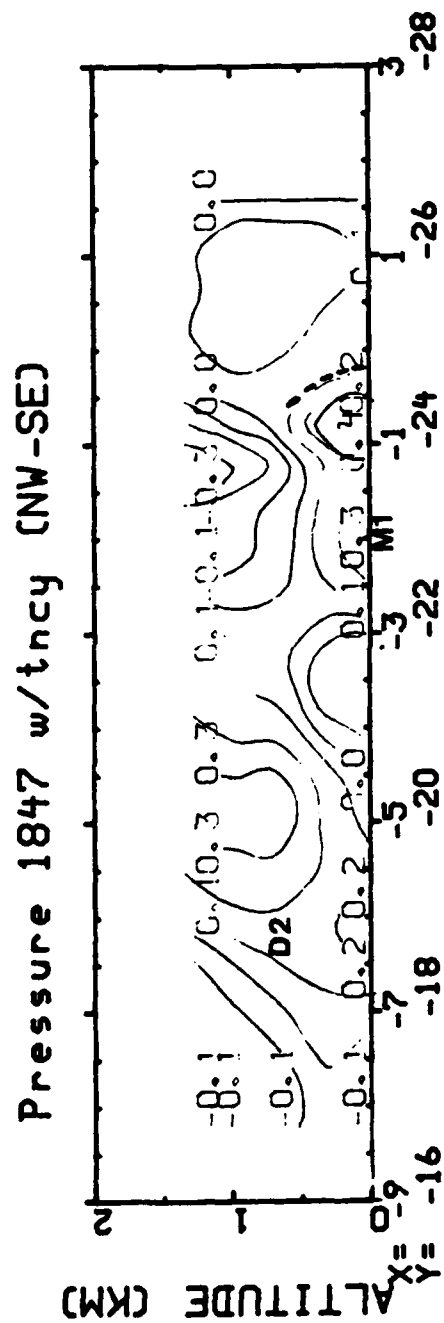


Fig 4.71 NW-SE cross-section of the pressure field  
(tendency included) for 1847 MDT.

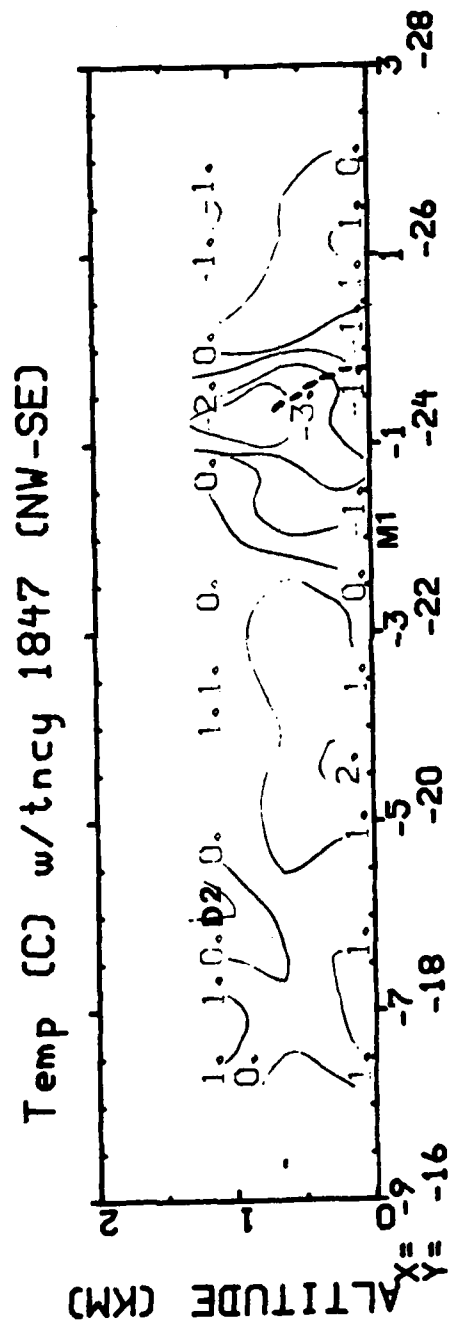


Fig 4.72 NW-SE cross-section of the temperature field  
(tendency included) for 1847 MDT.

#### 4.4.3 (NW-SE) Cross-Section at 1850

The 1850 perturbation pressure plot is shown in Figure 4.73. The meso-high at  $x = -1.5$  where M1's downdraft reaches the surface has grown since 1847; however, the gust front gradient has weakened because M3's outflow is now interrupting the environmental flow that was colliding with the outflow of M1 in the two previous time periods.

The temperature plot for 1850 is shown in Figure 4.74. The surface anomaly due to the outflow of cool air from M1 is evident in the area of  $x = -2$  to  $-1$ . The temperature gradient at the gust front may be less well defined than at 1847 since M3 blocks a great deal of the low-level environmental flow. The area of the gust front is apparent because of the diverging cool air of M1's outflow being lifted after the collision with environmental flow at the frontal boundary.

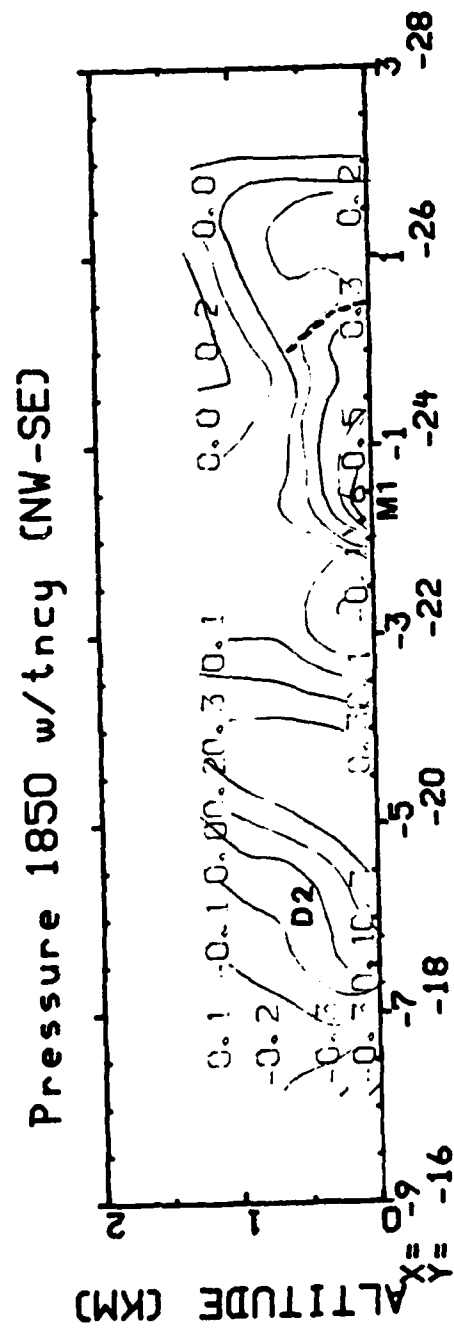


Fig 4.73 NW-SE cross-section of the pressure-field  
(tendency included) for 1850 MDT.

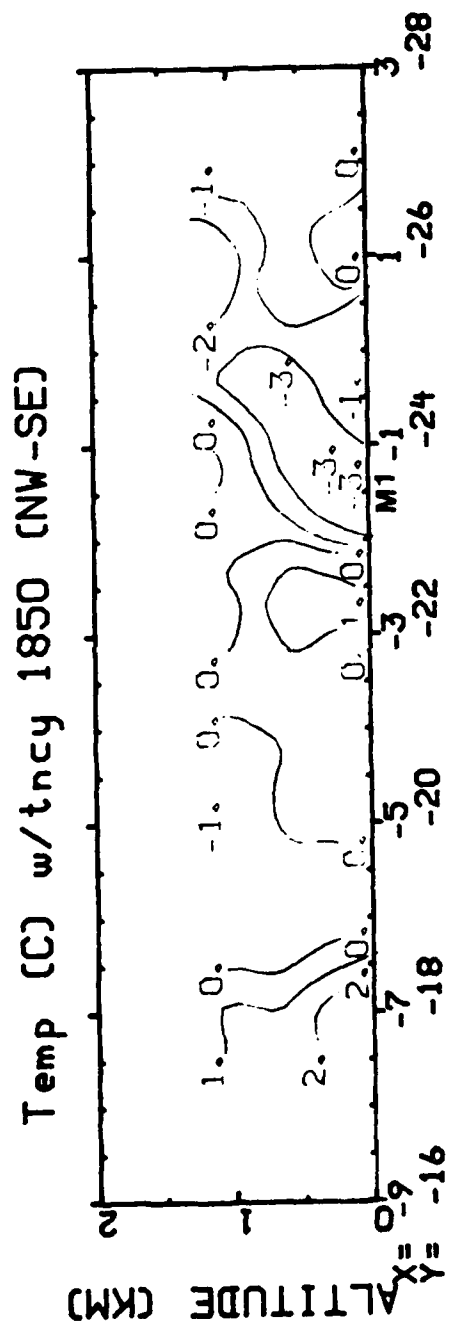


Fig 4.74 NW-SE cross-section of the temperature field  
(tendency included) for 1850 MDT.

#### 4.4.4 (E-W) Cross-Section at 1845

The 1845 (E-W) cross-section pressure field is shown in Figure 4.75. As was the case with the (NW-SE) plot, the surface meso-high at the point of the converging downflow of M1 is clearly shown at  $x = -2$ . This plot is a definite improvement over the same non-tendency field (i.e., Figure 4.43) since the definition of the isobars is much clearer. At the gust front in the vicinity of  $x = 0$ , there is a stagnant meso-high marking the point of converging outflow from the microburst. Note the trough at the mid-level of the plot at about  $x = -0.5$  where air rises over the gust front and splits to circulate around the gust front and enhance low-level convergence at the boundary.

The temperature plot for the 1845 (E-W) case is shown in Figure 4.76. There is a cold surface anomaly at  $x = -2$  as M1's descending air reaches the surface. In the upper layers, cool air descending causes a temperature anomaly from  $x = -3$  to 0. This clearly shows the descending precipitation-cooled downdraft as dry environmental air is being drawn into the downdraft and ventilates the downdraft as it descends.





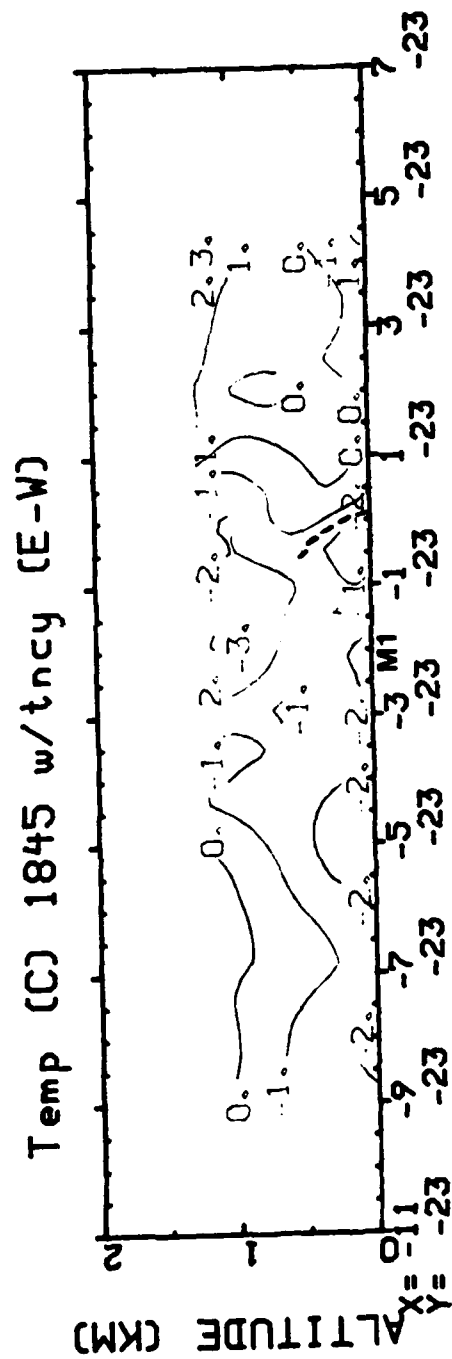


Fig 4.76 E-W Cross-section of the temperature field  
(tendency included) at 1845 MDT.

#### 4.4.5 (E-W) Cross-Section at 1847

The perturbation pressure plot for the (E-W) cross-section at 1847 is shown in Figure 4.77. Again the stagnation high at M1 is clearly shown at  $x=-2$ , and the tightened pressure gradient at the gust front is shown in the vicinity of  $x = 0$ .

The temperature plot for 1847 (Figure 4.78) shows the rising cool air from the outflow of M1 as it reaches the gust front in the vicinity of  $x = 0$ . The temperature differential at the frontal boundary is detailed in this plot by the convergence of two air masses with different temperature characteristics. This warm inflow/cold outflow collision is illustrated by the temperature gradient at the gust front boundary.



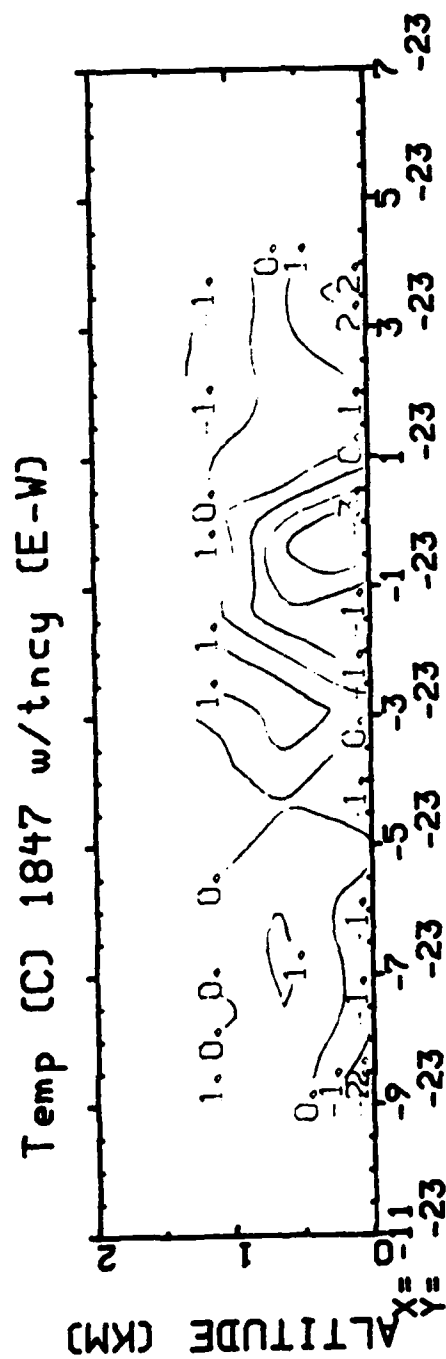
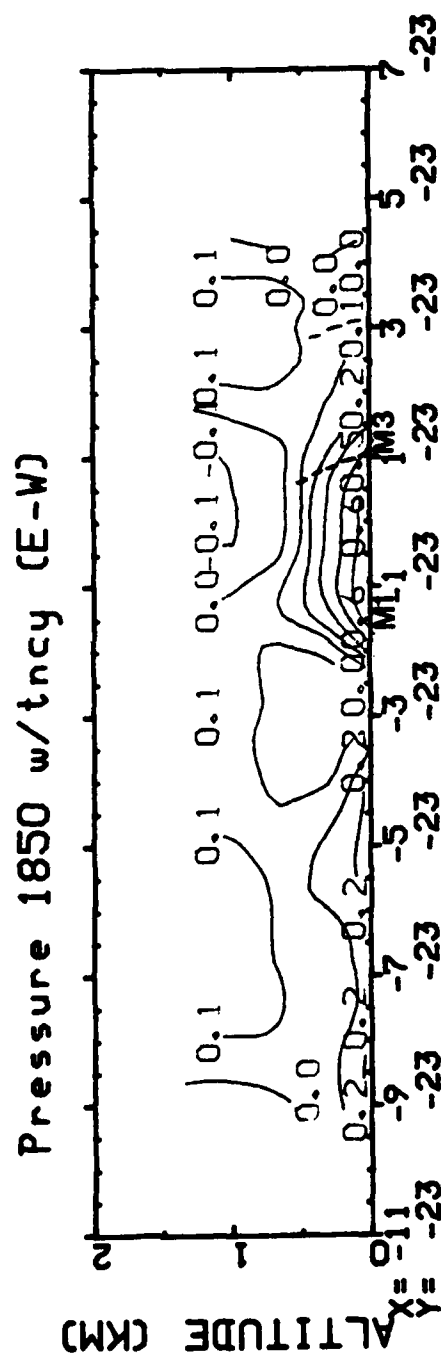


Fig 4.78 E-W cross-section of the temperature field  
(tendency included) for 1847 MDT.

#### 4.4.6 (E-W) Cross-Section at 1850

The 1850 (E-W) cross-section perturbation pressure field is shown in Figure 4.79. Note the strong pressure gradient between  $x = -1.5$  to  $1.5$ , as the result of converging downdrafts at the surface and the subsequent outflows of both M1 and M3. Now that M3 has reached the surface, the environmental flow that contributed to such a strong gust front in the area between M1 and M3 has been cut off by M3; hence, the gust front has weakened and is less well defined as a result of the interference of environmental flow by the new microburst, M3.

The temperature pattern for the 1850 (E-W) case is shown in Figure 4.80. The converging outflows of both M1 and M3 cause the rather large cold surface anomaly between  $x = -1.5$  and  $1.5$ . The cool outflows from both microbursts creates a dome of cool air in the area between them.



**Fig 4.79 E-W cross-section of the pressure field (tendency included) at 1850 MDT.**

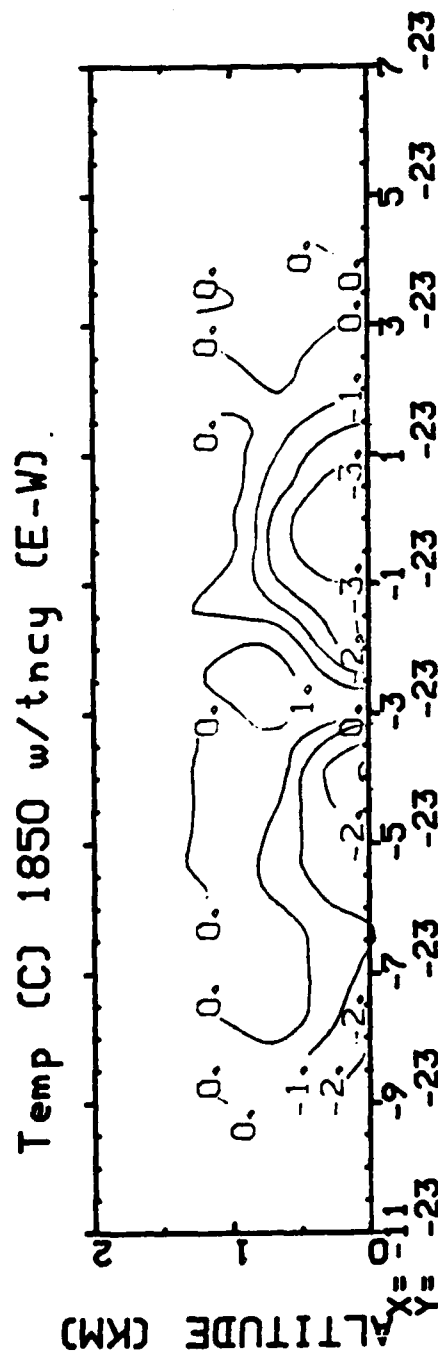


Fig 4.80 E-W cross-section of the temperature field  
(tendency included) at 1850 MDT.

## 5. Summary and Conclusions

This study was done to increase understanding of the 5 August 1982 case and, in particular, to study the circumstances surrounding microburst development in Colorado at 1845, 1847 and 1850 MDT on 5 August 1982. The JAWS dual-Doppler data collected in the atmospheric boundary layer were judiciously processed to produce a three-dimensional wind field at each analysis level. Subsequently, a thermodynamic retrieval method was employed to produce the fields of perturbation pressure and temperature from the Doppler derived wind field.

Inclusion of local tendency terms in the momentum equations produced more detailed perturbation pressure and temperature fields than were obtained excluding the tendency terms. Stagnation meso-highs at the surface where descending air of the microbursts reach the ground are clearly evident, as are perturbation pressure increases at the confluence of the gust front. The microbursts studied are cold-cored, so their rate of descent is slow enough ( $<5$  m/s) to allow evaporative cooling of the moist air within the downdraft. The temperature cross-sections show negative temperature perturbations as the descending cool air reaches the ground and diverges.



Microbursts can interact with each other's outflows, as well as with the environmental winds, to produce intense gust fronts and areas of significant vertical and horizontal shearing. A portion of the diverging cool air at the surface can be dynamically lifted at the front, along with most of the over-running warm environmental flow.

At levels above 1 km, drier air is entrained into the downdraft column where it mixes with moist air in the downdraft. The upper-level air maintains its momentum as it heads toward the surface, and serves as a mechanism to sustain the microburst's downflow. As the microburst extends to the surface, the downdraft column becomes stretched. As observed in the wind flow fields at 1 and 1.25 km, environmental air turns toward the downdraft at these upper levels as the column expands vertically. As the downdraft approaches the surface, increased entrainment of upper-level environmental air is observed. Circulation of the environmental winds in the vicinity of a downdraft at upper levels is a key to the resultant strength of the microburst and, ultimately, the intensity of its surface outflow.

As the rapidly moving downdraft contacts the surface, it diverges horizontally. This low-level compression is evidenced by the surface meso-high and a spin-down of the

downdraft; thus, near the outer edge of the microburst and the gust front boundary, a roll-type low-level turbulent circulation is observed. In this dynamic environment, vertical shear of the horizontal winds from the microburst's outflow and the environmental wind creates this rolling circulation; thus, air lifted at the gust front can spin as it rises. As this rotating air ascends, it facilitates entrainment of dry air into the downdraft above 1 km and thus serves as a feedback mechanism to maintain growth of the microburst. For example, the updraft caused by the gust front just east of M1 served not only as a feedback mechanism for M1, but also as a feeder for the second microburst, M3. M1 and M3 are thus inter dependent, and the formation of the additional microburst in the vicinity of M1 was not unusual based on the strength of the updraft at the gust front of M1.

The lifted rotating circulation helps channel dry environmental air into the downdraft of the microburst. It is important to note this circulation results from vertical shear at the microburst's horizontal low-level outflow. At the gust front, this rotating air is dynamically lifted; therefore, a downdraft that does not extend to the surface to create a strong gust front will be slow to develop a "feeder" circulation to perpetuate the downdraft with the entrainment of drier high-momentum environmental air.

By 1850 MDT, as the downdraft D2 is stretching closer to the surface, it finally begins to develop a circulation near the downdraft core at 1.25 km to channel dry air into the downdraft. This is the key reason M3 develops faster than D2 and becomes a *bona-fide* microburst sooner, although at 1845 MDT, D2 was stronger than D3 (the downdraft that eventually becomes M3). Prior to 1850, any upward vertical velocity near D2 was polluted with the cool outflow of M1; thus, the outflow of M1 helped to retard development of D2, while at the same time, enhance development of M3, the second microburst. As microbursts interact with their environment they can thus affect the timely development of phenomena in their vicinity.

## REFERENCES

- Armijo, L., 1969: A Theory for the Determination of Wind and Precipitation Velocities with Doppler Radars. *J. Atmos. Sci.*, 26, 566-569.
- Battan, L. J., 1973: *Radar Observations of the Atmosphere*. University of Chicago Press, Chicago, IL., 324pp.
- Brandes, E.A., 1977: Gust Front Evolution and Tornadoogenesis as Revealed by Doppler Radar. *J. Appl. Meteor.*, 16, 333-38.
- Condray, P.M., 1987: Momentum Flux in the Subcloud Layer of a Microburst-Producing Thunderstorm. M.S. Thesis, Saint Louis University, 97pp.
- Coover, J. A. Jr., 1988: Kinematic and Dynamic Studies of Microbursts in the Subcloud Layer Derived From JAWS Dual-Doppler Radar for a Colorado Thunderstorm. Ph.D. Dissertation, St. Louis University, 225pp.
- Elmore, K. L., J. McCarthy, W. Frost, and H. P. Chaug, 1986: A High Spatial and Temporal Multiple Doppler Analysis of a Microburst and Its Application to Aircraft Flight Simulation. *J. Appl. Meteor.*, 25, 1398-1425.
- Fujita, T. T., 1985: *The Downburst. Satellite and Mesometeorology (SMR<sup>o</sup>)*, University of Chicago, 51pp.
- Gal-Chen, T., 1978: A Method for the Initialization of the Anelastic Equations: Implications For Matching Models with Observations. *Mon. Wea. Rev.*, 106, 587-606.
- Hjelmfelt, M. R., 1987: The Microburst of 22 June 1982 in JAWS. *J. Atmos. Sci.*, 44, 1646-1664.
- Klingele, D. L., D. R. Smith, and M. M. Wolfson, 1987: Gust Front Characteristics as Detected by Doppler Radar. *Monthly Wea. Rev.*, 115, 905-918.
- Lin, Y. J., and J. A. Coover, 1988: A Kinetic Energy Analysis of a Microburst-Producing Thunderstorm Based on JAWS Dual-Dopple Data. *J. Atmos. Sci.*, 45, 2764-2771.
- \_\_\_\_\_, and P. M. Condray, 1988: Momentum Flux in the Subcloud Layer of a Microburst-Producing Thunderstorm Determined From JAWS Dual-Doppler Data.

*Boundary Layer Meteorology*, 43, 125-141.

\_\_\_\_\_, and R. G. Hughes, 1987: Structural Features of a Microburst-Producing Storm in Colorado Revealed by JAWS Dual-Doppler Radars. *J. Atmos. Sci.*, 24, 3640-3655.

\_\_\_\_\_, T. C. Wang, and J. H. Lin, 1986: Pressure and Temperature Perturbations Within a Squall-Line Thunderstorm Derived from SESAME Dual-Doppler Data. *J. Atmos. Sci.*, 43, 2302-2327.

Wilson, J. W., R. D. Roberts, C. Kessinger, and J. McCarthy, 1984: Microburst Wind Structure and Evaluation of Doppler Radar for Airport Windshear Detection. *J. Climate Appl. Meteor.*, 22, 1227-1241.

## BIOGRAPHY OF AUTHOR

William Edward McNamee was born [REDACTED]

[REDACTED], in the heart of the Big Sky Country.

He graduated from Anaconda Central Catholic High School, and then briefly attended Montana State University. This

was followed by two tours of duty with the U. S. Army, which included assignments in Korea and Okinawa. His

interest in earth science led to a B.S. degree in Petroleum Engineering from Montana Tech in 1982, and a

B.S. in Meteorology from the University of Utah in 1984.

He was commissioned an Air Force officer through the Officer Training School on July 1, 1983. After serving as an

atmospheric and space environment forecaster at the Cheyenne Mountain Complex in Colorado Springs, he was offered

an assignment through the Air Force Institute of Technology (AFIT) to pursue a Master of Science degree at St

Louis University, which he gratefully accepted.